

THE RADIAL VELOCITY EXPERIMENT (RAVE): FOURTH DATA RELEASE

G. KORDOPATIS¹, G. GILMORE¹, M. STEINMETZ², C. BOECHE³, G.M. SEABROKE⁴, A. SIEBERT⁵, T. ZWITTER^{6,7}, J. BINNEY⁸, P. DE LAVERNY⁹, A. RECIO-BLANCO⁹, M.E.K. WILLIAMS², T. PIFFL², H. ENKE², S. ROESER³, A. BIJAOUTI⁹, R.F.G. WYSE¹⁰, K. FREEMAN¹¹, U. MUNARI¹², I. CARILLO², B. ANGUIANO^{13,14}, D. BURTON^{11,15}, R. CAMPBELL¹⁶, C.J.P. CASS¹⁵, K. FIEGERT¹⁵, M. HARTLEY¹⁵, Q.A. PARKER^{13,14,17}, W. REID^{14,17}, A. RITTER¹⁸, K.S. RUSSELL¹⁵, M. STUPART¹⁵, F.G. WATSON¹⁵, O. BIENAYMÉ⁵, J. BLAND-HAWTHORN¹⁹, O. GERHARD²⁰, B.K. GIBSON²¹, E. K. GREBEL³, A. HELMI²², J.F. NAVARRO²³, C. CONRAD², B. FAMAËY⁵, C. FAURE⁵, A. JUST³, J. KOS⁶, G. MATIJEVIĆ⁶, P.J. MCMILLAN⁸, I. MINCHEV², R. SCHOLZ², S. SHARMA¹⁹, A. SIVIERO², E. WYLIE DE BOER¹¹, M. ŽERJAL⁶

¹Institute of Astronomy, University of Cambridge, Madingley Road, Cambridge, CB3 0HA, UK

²Leibniz-Institut für Astrophysik Potsdam, An der Sternwarte 16, D-14482 Potsdam, Germany

³Astronomisches Rechen-Institut, Zentrum für Astronomie der Universität Heidelberg, Mönchhofstr. 12-14, D-69120 Heidelberg, Germany

⁴Mullard Space Science Laboratory, University College London, Holmbury St. Mary, Dorking, Surrey, RH5 6NT, UK

⁵Observatoire Astronomique de Strasbourg, Université de Strasbourg, CNRS, UMR 7550, 11 rue de l'Université, 67000 Strasbourg, France

⁶Faculty of Mathematics and Physics, University of Ljubljana, Jadranska 19, 1000 Ljubljana, Slovenia

⁷Center of Excellence SPACE-SI, Askerceva cesta 12, 1000 Ljubljana, Slovenia

⁸Rudolf Peierls Centre for Theoretical Physics, Keble Road, Oxford, OX1 3NP, UK

⁹Laboratoire Lagrange, UMR 7293, Université de Nice Sophia Antipolis, CNRS, Observatoire de la Côte d'Azur, BP4229, 06304, Nice, France

¹⁰Johns Hopkins University, 3400 N Charles Street, Baltimore, MD 21218, USA

¹¹Research School of Astronomy and Astrophysics, Australian National University, Cotter Rd., Weston, ACT 2611, Australia

¹²INAF National Institute of Astrophysics, Astronomical Institute of Padova, 36012 Asiago (VI), Italy

¹³Australian Astronomical Observatory, PO Box 915, North Ryde NSW 1670

¹⁴Department of Physics and Astronomy, Macquarie University, Sydney, NSW, 2109

¹⁵Anglo-Australian Observatory, PO Box 296, Epping, NSW 1710, Australia

¹⁶Western Kentucky University, Bowling Green, Kentucky, USA

¹⁷Macquarie Research Centre for Astronomy, Astrophysics and Astrophotonics, Sydney, NSW, 2109, Australia

¹⁸National Central University, 300 Zhongda Rd., Zhongli City, Taoyuan County, 325 Taiwan (R.O.C.)

¹⁹Sydney Institute for Astronomy, School of Physics A28, University of Sydney, NSW 2006, Australia

²⁰Max-Planck-Institut fuer Ex. Physik, Giessenbachstrasse, D-85748 Garching b. Muenchen, Germany

²¹Jeremiah Horrocks Institute, University of Central Lancashire, Preston, PR1 2HE, UK

²²Kapteyn Astronomical Institute, University of Groningen, PO Box 800, NL-9700 AV Groningen, the Netherlands

²³Department of Physics and Astronomy, University of Victoria, Victoria, BC, Canada

Draft version August 1, 2018

ABSTRACT

We present the stellar atmospheric parameters (effective temperature, surface gravity, overall metallicity), radial velocities, individual abundances and distances determined for 425 561 stars, which constitute the fourth public data release of the RAdial Velocity Experiment (RAVE). The stellar atmospheric parameters are computed using a new pipeline, based on the algorithms of MATISSE and DEGAS. The spectral degeneracies and the 2MASS photometric information are now better taken into consideration, improving the parameter determination compared to the previous RAVE data releases. The individual abundances for six elements (magnesium, aluminium, silicon, titanium, iron and nickel) are also given, based on a special-purpose pipeline which is also improved compared to that available for the RAVE DR3 and Chemical DR1 data releases. Together with photometric information and proper motions, these data can be retrieved from the RAVE collaboration website and the Vizier database.

Subject headings: catalogs — stars: fundamental parameters — stars: abundances — techniques: spectroscopic — surveys

1. INTRODUCTION

The assembly history of the Milky Way can be obtained by analysing the positions, the kinematics, the ages and the chemical compositions of large statistical samples of Galactic stars (Freeman & Bland-Hawthorn 2002). In addition to the identification and characterisation of hierarchical signatures (e.g. Helmi et al. 1999; Abadi et al. 2003; Sales et al. 2009), the precise measurement of the age-metallicity relation in the solar neighbourhood, for a very large sample of stars, allows us to establish, among much else, the strength and the importance of radial migration in the Galaxy, perhaps a key in-

gradient for Galactic evolution (Sellwood & Binney 2002; van der Kruit & Freeman 2011).

Ideally, one would need stellar spectra and precise distances to achieve such a goal. Nevertheless, even in the case where parallaxes are not available, it is still possible to estimate statistically valuable ages and distances of the stars by measuring from their spectra their atmospheric parameters (effective temperature, T_{eff} , surface gravity, $\log g$, overall metallicity, $[M/H]^1$) and projecting them afterwards on theoretical stellar isochrones (Bred-

¹ The stellar overall metallicity is defined as $[M/H] = \log \left(\frac{N(M)}{N(H)} \right)_{\star} - \log \left(\frac{N(M)}{N(H)} \right)_{\odot}$ where N represents the number density and M all the elements heavier than He.

dels et al. 2010; Zwitter et al. 2010; Burnett et al. 2011; Kordopatis et al. 2011b; Binney et al. 2013).

In the last decade, the advent of multi-fibre spectrographs, combined with large telescopes, has allowed the astronomical community to obtain such very large amounts of spectra in order to explore the evolution of our Galaxy. Until the release of the first substantial catalogue of Gaia (estimated to be available in early 2017), the already current main large spectroscopic surveys of the Milky Way are the *Sloan Extension for Galactic Understanding and Exploration* (SEGUE), the *RA*dial *Ve*locity *Ex*periment (RAVE), the *APO Galactic Evolution Ex*periment (APOGEE), the *LAMOST Ex*periment for *Galactic Ex*periment and *understanding* (LEGUE), the *Galactic Archaeology with HERMES* (GALAH) and the *Gaia-ESO Survey* (GES).

RAVE² began observations in 2003, and since then has released three data releases (noted DR hereafter): DR1 in 2006, DR2 in 2008 and DR3 in 2011 (Steinmetz et al. 2006; Zwitter et al. 2008; Siebert et al. 2011b). Furthermore, three catalogues with spectrophotometrically derived distances were published (Breddels et al. 2010; Zwitter et al. 2010; Burnett et al. 2011) and one catalogue with abundances for the individual elements Magnesium (Mg), Aluminium (Al), Silicon (Si), Calcium (Ca), Titanium (Ti), Iron (Fe), and Nickel (Ni) (Boeche et al. 2011). RAVE is a magnitude-limited survey of stars randomly selected in the southern celestial hemisphere. The original design was to only observe stars in the interval $9 < I < 12$ but the actual selection function includes stars both brighter and fainter (see Sect. 2). The spectra are obtained from the 6dF facility on the 1.2m Anglo-Australian Observatory's Schmidt telescope in Siding Spring, Australia, where three field plates with 150 robotically positioned fibres are used in turn. The effective resolution of RAVE is $R = \lambda/\Delta\lambda \sim 7500$ and the wavelength range coverage is around the infrared ionised Calcium triplet (IR Ca II, $\lambda\lambda 8410 - 8795\text{\AA}$), one of the widely used wavelength ranges for Galactic archaeology. Up to now, previous RAVE catalogues have released 83 072 radial velocities for 77 461 stars, and 41 672 sets of atmospheric parameters for 39 833 stars. These produced many valuable studies.

Seabroke et al. (2008) used the symmetry of the velocity distributions to rule out the presence of the Sagittarius stream or the Virgo overdensity in the solar neighbourhood. Recently, RAVE data allowed Williams et al. (2011) to discover the Aquarius stream and Antoja et al. (2012) to identify additional moving groups in the Galactic disc, consistent with dynamical models of the effects of the bar and the spiral arms. Pasetto et al. (2012a,b) used RAVE data in order to constrain the solar motion relative to the local standard of rest, the rotational lag of the thick disk component, and the components of the thin disk velocity ellipsoids in the solar neighbourhood. Additionally, Siebert et al. (2011a, 2012) measured the mean galactocentric radial velocity of stars in the extended solar neighbourhood and constrained the parameters of Milky Way spiral structure. Williams et al. (2013) identified differences in the velocity distribution between the north and the south of the Galactic plane with indica-

tions of a rarefaction-compression pattern, suggestive of wave-like behaviour. Furthermore, Ruchti et al. (2011); Wilson et al. (2011) and Fulbright et al. (2010) studied the chemo-dynamical information of the thick disc and metal-poor stars of the Galaxy, whereas Matijević et al. (2010, 2011) used RAVE to study single-lined and double-lined binary stars.

Here we present the new DR4 catalogue, which includes 482 430 spectra. In order to obtain the atmospheric parameters, an updated version of the Kordopatis et al. (2011a) pipeline is used, which combines the DE-GAS decision-tree method (*DE*cision *tree* *a*l*G*orithm for *A*strophysics, Bijaoui et al. 2012) as well as the MATISSE projection algorithm (*MA*Trix *I*nversion for *S*pectral *S*ynth*E*sis, Recio-Blanco et al. 2006) and which takes into account, for the first time, the *Two Micron All Sky Survey* (2MASS) photometric information. This allows us to treat more efficiently the spectral degeneracies than the maximum a posteriori method used in the previous data releases, reducing parameter combinations which were found in astrophysically non-justified parts of the ($T_{\text{eff}} - \log g$) space.

Furthermore, this DR4 catalogue takes advantage of a multitude of new calibration data sets that have been collected recently in order to obtain reliable metallicities. The calibration libraries consist of RAVE and RAVE-like spectra for which there are parameter determinations derived from high-resolution spectroscopy, and stars selected from open and globular clusters of well-known metallicities. In addition to the stellar atmospheric parameters published for the newly observed targets, these calibration spectra and the new pipeline have also been applied in order to re-estimate and re-calibrate the parameters from the previous data-releases. Then, given the new effective temperatures, surface gravities and metallicities, individual abundances are also computed for the entire data set, using an updated version of the Boeche et al. (2011) chemical pipeline. Finally, new distances are also inferred, using the methods presented in Zwitter et al. (2010) and Binney et al. (2013).

The paper is structured as follows: First, in Sect. 2 we present the new input catalogue of RAVE, and in Sect. 3, we present the pipeline that is used in order to obtain the atmospheric parameters, by recalling the basic equations and the updates of the MATISSE and DEGAS algorithms that are in the core of this new parameterisation pipeline. Then, in Sect. 4, we show which calibration data sets are used and discuss how the calibration relation is obtained. Section 5 presents the updates on the chemical pipeline that is used in order to measure the individual abundances. Based on the presented pipelines and the calibration relation that is established, we present in Sect. 6 the DR4 atmospheric parameters catalogue, as well as a comparison with the previous DR3 parameters, in particular for the metallicities. Sections 7, 8, 9 and 10 present the DR4 catalogue for the proper motions, the radial velocities and the stellar distances, as well as a description of the *AAVSO Photometric All-Sky Survey* (APASS) photometry which is recommended to be used as it becomes available. Finally, Sect. 11 sums up.

² <http://www.rave-survey.org>

The RAVE wavelength window of 8410–8795Å implies that an *I*-band selection of the targets is the most appropriate. However, when RAVE started observing in April 2003, there was no southern sky *I*-band photometric survey spanning the RAVE magnitude range. Therefore, the original input catalogue was constructed by deriving *I* magnitudes from Tycho-2 photometry and filling in Tycho-2’s incompleteness at the faint end of the RAVE magnitude range with SuperCOSMOS photographic *I* magnitudes (see DR1 paper for more details). The *DEep Near Infrared Survey of the Southern Sky* (DENIS) DR2 was available in May 2005 (DENIS Consortium 2003), which included Gunn-*I* photometry at 0.82 μm , but did not have sufficient coverage (55% of the southern sky) to be used as the basis for a new RAVE input catalogue. RAVE DR1, DR2 and DR3 were solely observed from the original input catalogue. DR3 was the last release to be solely observed from the original input catalogue, thereby concluding the pilot survey.

DENIS DR3 was available in September 2005 (The Denis Consortium 2005) and did have sufficient coverage (80% of the southern sky) to be used as the basis for a new RAVE input catalogue. DENIS entries within the RAVE magnitude range ($9 < I < 12$ mag) were selected, including saturated entries (DENIS saturates at $I < 9.8$ mag – see later discussion). Entries with *I* magnitude error = 1 indicate a non-estimated error so these entries were rejected. Then the remaining entries were cross-matched with 2MASS using a 1 arcsec box search. This search region was chosen because both DENIS and 2MASS were calibrated on the USNO-A2.0 catalogue, which has an astrometric accuracy of 0.5 arcsec. The nearest DENIS DR3 catalogue entry to a 2MASS star provided the *I* magnitude for that star (2MASS does not include *I*-band photometry). DENIS catalogue entries not within a 1 arcsec search box of a 2MASS star were rejected.

At the edges of the DENIS CCD detector, both the astrometry and photometry become less accurate. For each different scan of DENIS strip overlap regions, the catalogue reports every detection of a source. If a star in this region is imaged more than once, each detection is included in the catalogue because, although the multiple detections have almost identical magnitudes and positions, they cannot be associated with the same source. Cross-matching DENIS with 2MASS not only removes these multiple detections from the new input catalogue but also provides more accurate astrometry, leading to fibre placement better matching stellar positions on the sky, which results in higher signal-to-noise spectra. DENIS includes spurious sources due to charge bleeding and diffraction spikes, which do not have matches in 2MASS and so are removed from the new DENIS input catalogue, increasing its efficiency.

Comparison of Figure 1 with Siebert et al. (2011b) Figure 17 shows that, in addition to covering the sky area of the original RAVE input catalogue, the new DENIS input catalogue has the major new feature of extending to lower Galactic latitudes (*b*). The aim of the extension towards the Galactic anti-rotation direction ($225^\circ < l < 315^\circ$, $5^\circ < |b| < 25^\circ$) is to observe the outer Galactic disc. Distances probed at the faint magnitude limit ($I = 12$ mag) are expected to be up to ~ 5 kpc for K-type giants (assuming $M_I = +1$ mag

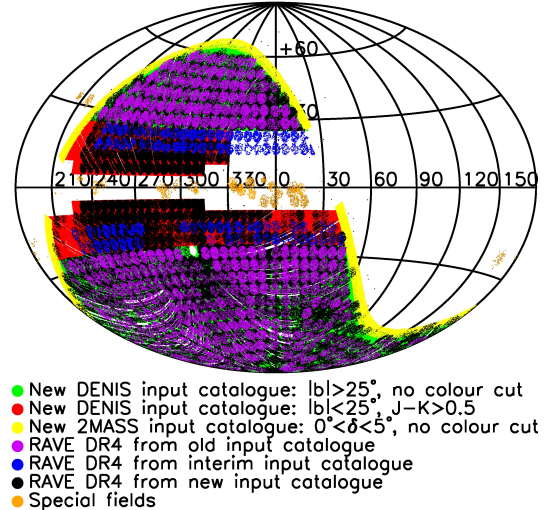


FIG. 1.— Aitoff projection of Galactic co-ordinates of the new input catalogues, colour-coded into no colour cut and colour cut samples. Overlaid are the RAVE DR4 stars, colour-coded according to their source input catalogue. Their pattern is due to the 6dF field of view (5.9°). The original input catalogue was observed with field centre co-ordinates separated by 5.7° . The new input catalogue was observed with field centre co-ordinates separated by 5.0° .

and no extinction). Therefore, at low Galactic latitudes in this direction, giants just reach the nominal ‘edge’ of the stellar disc. Symmetric sampling about the Galactic plane will constrain the disc warp and flare. Distances probed at $I = 12$ mag are only up to ~ 400 pc for G-type dwarfs (assuming $M_I = +4$ mag). Therefore, the most efficient way to observe the outer disc is to apply a colour cut ($J - K > 0.5$ mag) in this region to avoid observing G-type dwarfs and preferentially observe K-type giants. The Besançon Galactic model (Robin et al. 2003) predicts that in the RAVE magnitude range at $J - K > 0.5$ mag 70% of stars are KM-type giants and 30% are KM-type dwarfs. Although DENIS includes *J* and *K* photometry, the colour cut is performed using 2MASS *J* and *K*. This is because of the aforementioned edge affect on the DENIS CCDs and due to higher levels of sky image noise in DENIS than 2MASS. The noise comes from the thermal infra-red background radiation emitted by the instrument itself. 2MASS optics avoid this by including a cold stop, which DENIS optics do not have.

After observing the new DENIS input catalogue from 2006 to 2010, more targets closer to the Galactic plane were required to maintain RAVE’s observing efficiency due to sky regions not always being observable from the UK Schmidt Telescope (UKST) at different times of the year. The aim was still to target red giants by selecting $J - K > 0.5$ mag, thereby rejecting young foreground stars, which have weak Paschen lines that yield less accurate radial velocities. This selection works with reddening of $E(B - V) < 0.35$ mag. Therefore to preserve a homogeneous selection function with this colour cut, the new DENIS input catalogue was extended closer to the Galactic plane in regions where $E(B - V) < 0.35$ mag. The northern Galactic hemisphere of the Galactic bulge

has $E(B - V) > 0.35$ mag and so $b < 25^\circ$ at $l > 330^\circ$ and $l < 30^\circ$ is not included in the new extended DENIS input catalogue. $10^\circ < b < 25^\circ$ at $l < 225^\circ$ and at $315^\circ < l < 330^\circ$ has $E(B - V) < 0.35$ mag and so is included. In the southern hemisphere of the bulge, $-10^\circ < b < -25^\circ$ at $l < 225^\circ$, $l > 315^\circ$ and $l < 30^\circ$ all have $E(B - V) < 0.35$ mag and so are included.

DR4 includes observations of the interim input catalogue, which extended the original input catalogue from $|b| < 25^\circ$ to $|b| < 15^\circ$ at all l . These observations were taken before the new DENIS input catalogue was available, which is why they sample the northern bulge (blue dots in Figure 1) outside of the new extended DENIS input catalogue colour cut footprint (red dots in Figure 1). However, there are many observations of the interim input catalogue (blue dots in Figure 1) within the colour cut footprint. It is important to note that these do not include the colour cut and so include all colours. These fields can be identified using the Galactic co-ordinates in Figure 1 and obsdate ≤ 20060312 . The special fields outside of the colour cut footprint (orange dots in Figure 1) are specific science and calibration fields and do not include the colour cut.

More bright targets north of the celestial equator ($\delta \leq 5^\circ$) were required, again, to maintain RAVE's observing efficiency in bright time. DENIS's sky coverage is $\delta \leq 2^\circ$. Therefore, to extend the input catalogue to $\delta = 5^\circ$ required DENIS I to be constructed from 2MASS J and K using:

$$I_{\text{DENIS}} = J_{2\text{MASS}} + 0.054 + 1.18(J_{2\text{MASS}} - K_{2\text{MASS}}) \quad (1)$$

where $\Delta_{\text{DENIS}} = 0.15$ mag. This was done for 2MASS sources with $0^\circ \leq \delta \leq 5^\circ$ and $0^h < \alpha < 6^h$, $7^h30 < \alpha < 17^h$ and $19^h30 < \alpha < 24^h$ (yellow dots in Figure 1) to avoid the Galactic plane. The 2MASS input catalogue spatially overlaps the DENIS input catalogue by $\Delta\delta = 3^\circ$ because DENIS's sky coverage is not complete. The long white areas within the coloured regions in Fig. 1 are one or more slots (12 arcmin in α by 30° in δ), where the observed DENIS strips filling these slots are missing from DENIS DR3. The small white areas within the coloured regions are one or more missing DENIS images (12 arcmin \times 12 arcmin). The white circular region within the coloured regions is the southern equatorial pole, which is not observed by DENIS. The width of the missing DENIS strips and images is 3.5% of the 6dF field of view and so does not pose a fibre configuration problem. Its effect on RAVE's random selection of targets should be negligible. It is important to note that observations from the 2MASS input catalogue at $|b| > 25^\circ$ do not include the colour cut and so include all colours. Figure 1 shows that there are only three DR4 fields that spatially overlap the DENIS input catalogue colour cut footprint and the 2MASS input catalogue footprint and so have mixed selection functions.

Figure 2 compares the new input catalogues and the number of observed DR4 spectra as a function of I magnitude. It emphasises that the observed DR4 spectra have not exhausted the new DENIS input catalogue overall and so are not complete with respect to DENIS overall, although individual fields may be complete. Indeed, the new DENIS input catalogue is only complete where DENIS has sky coverage. DR4's completeness with re-

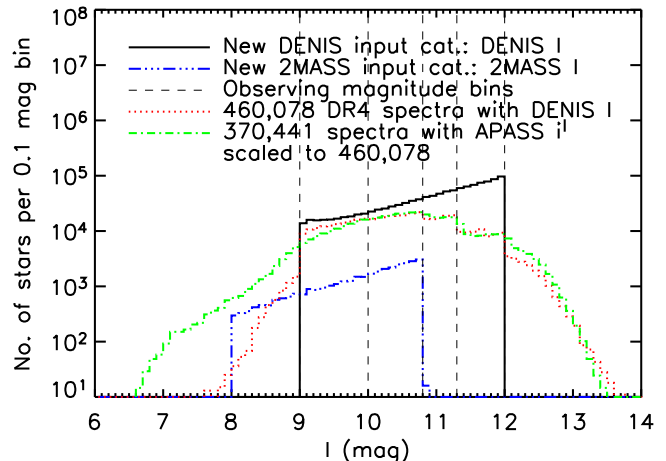


FIG. 2.— Histogram comparing the new input catalogues as a function of I magnitude and the selection functions of all the observed RAVE stars as a function of I magnitude and as a function of APASS i' magnitude, which is similar but not identical to DENIS I .

spect to 2MASS is shown in Figure 3. Figure 2 also shows that the 2MASS input catalogue extends the bright limit of the survey to $I = 8$ mag. Each 6dF field set-up only selects new input catalogue targets from one of the following four magnitude bins: $9.0 < I < 10.0$ ($8.0 < I < 10.0$ for the new 2MASS input catalogue), $10.0 < I < 10.8$, $10.8 < I < 11.3$ and $11.3 < I < 12$ mag, which are visible in Figure 2. This minimises the magnitude range within any one 6dF field set-up to be within a bin, meaning exposure times can be scaled more appropriately for all the targets in the same field. Each field set-up is a random selection of unobserved targets within these bins (apart from designed repeat observations). Any spectrum within a 6dF field set-up can be adjacent to any other in the same set-up on the CCD but the bins limit the magnitude difference, which also minimises fibre cross-talk.

Figure 2 compares the selection functions of the new input catalogues and the observed DR4 stars. The input catalogues have step functions at their bright and faint ends. However, the observed DR4 stars do not have step functions but extend to brighter and fainter than the input catalogues. Because DENIS saturates at $I < 9.8$ mag, the selection function of RAVE's new input catalogue and observations need to be compared to an I -band survey that doesn't saturate in the RAVE magnitude range. The recent advent of the *AAVSO Photometric All-Sky Survey* (APASS - see Sect. 10) means that this can now be explored. Future data releases will be supplemented with APASS photometry. At the time of writing, APASS i' (internal release DR7) was available for 370,441 spectra and is plotted in Figure 2, scaled to the number of DR4 spectra. It shows that the distribution of APASS i' approximately agrees with the distribution of DENIS I at the faint end but extends to much brighter magnitudes at the bright end. This is because DENIS saturates at $I < 9.8$ mag, which means some sources are actually $I < 9$ mag.

The overall selection function of DR4 is more clearly seen in Fig. 4. It has a complex shape due to the observ-

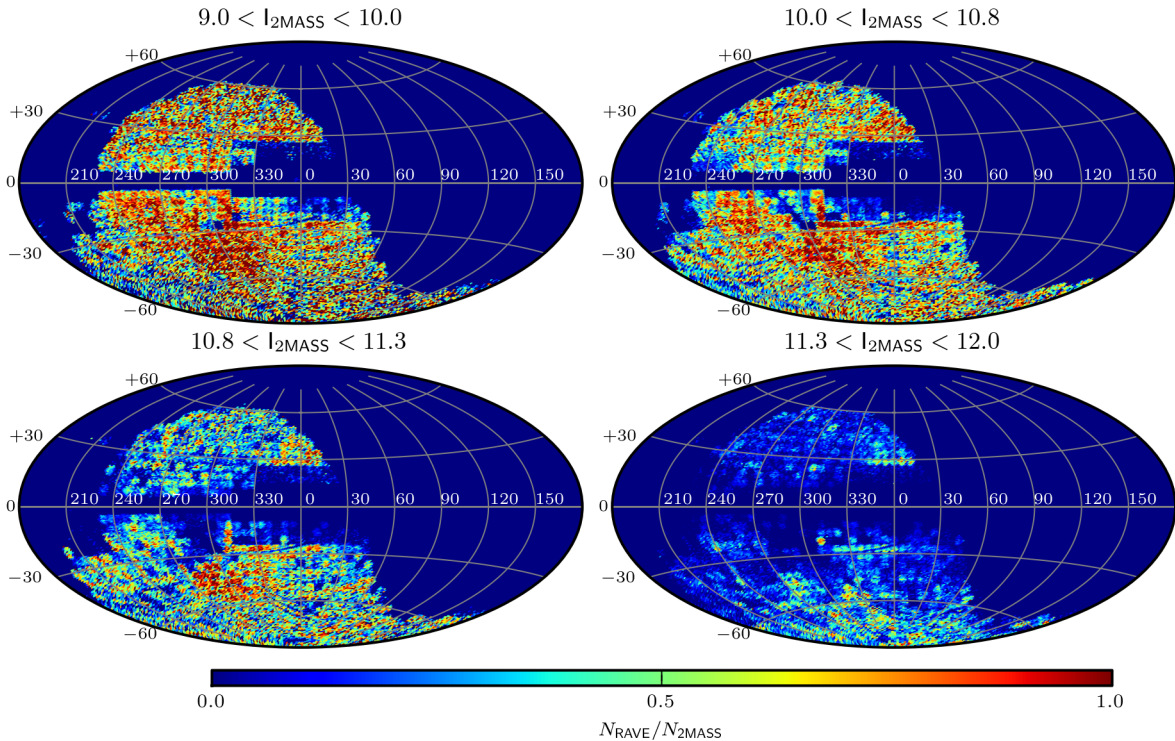


FIG. 3.— Aitoff projection of Galactic co-ordinates of the completeness of the stars in the $I_{2\text{MASS}}$ band for which radial velocity measurements are available. Each panel shows a different magnitude bin. Grey-scale coding represents the ratio of RAVE observations to 2MASS stars. Only stars with errors in radial velocity less than 10 km s^{-1} are shown.

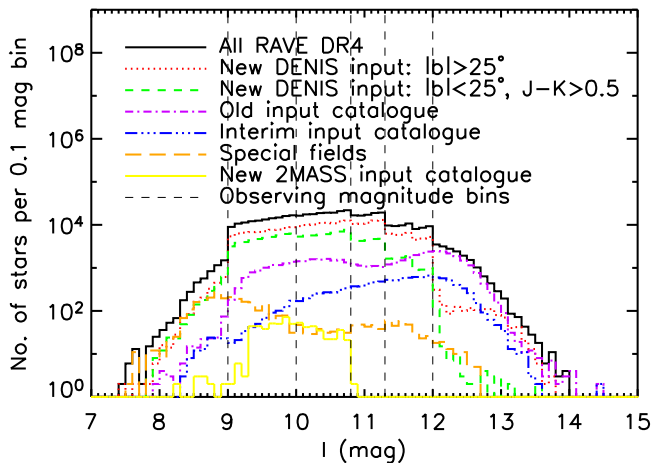


FIG. 4.— Histogram decomposing DR4 into its constituent input catalogues as a function of I magnitude. Note that this is either DENIS I or 2MASS constructed DENIS I and so are not reliable at $I < 9.8 \text{ mag}$ due to DENIS I saturation.

ing strategy and because DR4 includes all RAVE observations up to the end of 2012, which have been selected from four different RAVE input catalogues. Numerically, DR4 is dominated by stars selected from the new DENIS input catalogue ($|b| > 25^\circ$). This means the observing magnitude bins are visible in the DR4 selection function. It also means that overall the new input catalogue observations have filled in the incompleteness of the old input catalogue (mainly due to Tycho-2) thus reducing

the presence of its subtle selection biases in DR4, compared to DR1, DR2 and DR3. Therefore, overall RAVE DR4 is more representative of the underlying Galactic stellar populations than previous DRs, with the exception of $|b| < 25^\circ$ which deliberately targets giants with $J - K > 0.5 \text{ mag}$. Nevertheless, on a field by field basis, Galactic science still requires care to account for the various selection biases introduced by the inhomogeneous photometry used to derive some of the input samples (detailed in the DR1 paper). Care is required if stars are selected from DR4 using their observation date as the selection function changes as a function of time: old and interim input catalogues $\text{obsdate} \leq 20060312$; new DENIS input catalogue $\text{obsdate} > 20060312$; new 2MASS input catalogue $\text{obsdate} > 20120128$. There may also be a stellar position bias because the 6dF fibre positioner software avoids putting targets too close to each other and also avoids crossing of fibres.

Figure 4 shows that the faint tail of the DR4 magnitude distribution is dominated by the old input catalogue. This tail is fainter than the nominal selection of $I < 12 \text{ mag}$ due to SuperCOSMOS photographic I magnitudes being saturated. The twin peaks of the old input catalogue are due to the merging of Tycho-2 and SuperCOSMOS. The interim input catalogue also includes Tycho-2 and SuperCOSMOS but weights their relative numbers to achieve a single peak in its magnitude distribution. The special fields are identified by being away from the main data. However, there are many calibration and science stars within the main footprint of the survey and so are classed as stars observed from the new input catalogue. These dominate the bright tail of the DR4

magnitude distribution in Figure 4 and also contribute to the faint tail. The old and interim input catalogues contribute to the bright tail because their bright magnitudes were constructed from Tycho-2 B_T and V_T .

To summarise, DR4 has no kinematic bias and no overall photometric bias. The notable exception is the colour criterion ($J - K > 0.5$ mag) to deliberately target giants at $|b| < 25^\circ$ (except where $\delta > 0^\circ$). No other colour cuts exist in the data. However, on a field by field basis, subtle selection biases may still be present.

3. THE NEW PIPELINE FOR THE STELLAR PARAMETERS

The wavelength region $\lambda\lambda 8410 - 8795\text{\AA}$ is often used for Galactic archaeology purposes, as for instance with the multi-fibre spectrographs of ESO FLAMES-Giraffe at the LR8 and HR21 setups, and the Gaia-RVS. Indeed, it is a spectral region with relatively few telluric absorptions, that exhibits many iron and α -element lines, in particular the prominent Ca II triplet ($\lambda = 8498.02\text{\AA}$, 8542.09\AA , 8662.14\AA). This feature is still visible at low signal-to-noise-ratio (SNR) and low metallicity, and as a consequence, it allows relatively easily to have radial velocity measurements and metallicity estimations for any type of spectrum.

3.1. Spectral degeneracies in the infrared ionised Calcium triplet wavelength range

The recent work of Kordopatis et al. (2011a, noted K11 hereafter) on spectra with a resolution $R \leq 10\,000$ has shown that the Ca II wavelength range suffers from spectral degeneracies that, if not appreciated, can introduce serious biases in spectroscopic surveys that use automated parameterisation pipelines. These degeneracies are mostly important for cool main-sequence stars, and stars along the giant branch. On the one hand, the spectral signatures that are used to determine the surface gravities for the main-sequence stars are insensitive to small $\log g$ variations, hence reducing the accuracy of the measurement of that parameter. On the other hand, the spectra of stars along the giant branch can be identical for different sets of parameters. In this case, the degeneracy is due to the fact that the spectral signatures sensitive to variations of effective temperature, surface gravity and metallicity are the same. The degeneracy works as follows: the spectrum corresponding to a given T_{eff} , $\log g$ and $[\text{M}/\text{H}]$, is almost identical to a spectrum corresponding to a lower (higher) temperature, lower (higher) surface gravity and lower (higher) metallicity.

Automated parameterisation pipelines try to find the model template that minimises the distance function, defined as the difference between the observation and a set of reference (model) spectra. In the case where not enough information is available in the data, the distance function can become non-convex, and secondary minima can appear, in which the parameterisation algorithms can falsely converge. If these secondary minima are close in the parameter space, the resulting parameter estimation will have a large scatter around the true value, whereas if they are distant in the parameter space, the algorithms might converge randomly to one or the other according to where the noise is placed in the spectrum.

In K11 it has been shown that for low and medium resolution spectra around the IR Ca II, decision-tree methods manage to better find the absolute minimum of the distance function, compared to other algorithms, like the projection methods (e.g.: principal component analysis) or the ones trying to solve an optimisation problem (e.g.: minimum χ^2), in particular when the SNR is low. For that reason, the pipeline presented in K11 iteratively renormalises the spectra and obtains the atmospheric parameters using a combination of a decision-tree algorithm called DEGAS (Bijaoui et al. 2012) and a projection method called MATISSE (Recio-Blanco et al. 2006) which allows to better interpolate between the grid points.

Both DEGAS and MATISSE have a learning phase based on a nominal library of synthetic spectra (*i.e.* the templates), described in Sect. 3.4. Here we describe briefly the pipeline and the two algorithms, but we refer the reader to Recio-Blanco et al. (2006); Bijaoui et al. (2012); Kordopatis et al. (2011a) for further details.

3.2. DEGAS: an oblique k -d decision-tree method for the low SNR spectra, and for re-normalisations

In the limit of the sampling precision of a learning grid (*i.e.* the parameter steps), parameter estimation is a pattern recognition problem. The grid of synthetic spectra can be treated as a known set of patterns among which the observed spectra should be identified. The DEGAS (*DE*cision *tree* *alG*orithm *for* *AS*trophysics) algorithm is an oblique 3-d decision tree (in our case T_{eff} , $\log g$ and $[\text{M}/\text{H}]$), for which the decisions result from the projection of the observations onto N node vectors noted $D_n(\lambda)$ ($n = 1 \dots N$). These node vectors are associated with a subset of spectra of the nominal library, in the sense that the result of the projection of an observed spectrum on that node will select half of the subset which most closely resembles the observation.

The recognition rules of DEGAS, at each node, are established during the learning phase as follows:

1. The mean vector $M(\lambda)$ of the flux values per pixel of all the reference spectra in the subset is computed.
2. For each reference spectrum $S_j(\lambda)$ associated with the node, the scalar product $c_j = \sum_{\lambda} S_j(\lambda) \cdot M(\lambda)$ is calculated. Let \bar{c} be the median value of c_j .
3. The reference spectra are bisected in two new subsets, T_1 and T_2 , according to the following criteria: S_j belongs to the subset T_1 if $c_j \leq \bar{c}$
 S_j belongs to the subset T_2 if $c_j > \bar{c}$.
4. The difference vector $D(\lambda) = M_1(\lambda) - M_2(\lambda)$ is determined, where $M_1(\lambda)$ and $M_2(\lambda)$ are the mean vectors of the flux values of each subset.
5. If the correlation coefficient between $M(\lambda)$ and $D(\lambda)$ is too small (typically, smaller than 0.999), the initial subset of reference spectra is re-separated by the hyperplane defined by $D(\lambda)$, iterating until convergence (going back to step 2, replacing $M(\lambda)$ by $D(\lambda)$).

When the previous procedure has converged for a particular node n , the final adopted projection node vector $D_n(\lambda)$ is determined, that will display the features that allow the separation of the subset of learning spectra at that node. The final median value \tilde{c}_n of $c_j = \sum_{\lambda} S_j(\lambda) \cdot D_n(\lambda)$ that will allow us to make the decisions is also set.

In this way, the recognition tree is built, having $\log_2(N)$ levels, where N is the number of spectra of the learning grid. At the lowest level nodes of the tree, only one training spectrum remains associated with each node. During the application phase, the target data $O_i(\lambda)$ passes through all the levels of the recognition tree, and a template is associated with it.

Of course, noise can induce misclassifications. The exploration of the branches, even if the decision threshold \tilde{c}_n does not allow it, is accomplished thanks to an activation function on the directions of the tree. Let us consider:

$$u_i = \frac{c_i - \tilde{c}_n}{\sigma_{c_i}} \quad (2)$$

where $c_i = \sum_{\lambda} O_i(\lambda) \cdot D_n(\lambda)$, $\sigma_{c_i} = S_f \cdot \sqrt{\sum_{\lambda} D_n(\lambda)^2}$ and S_f is an arbitrary constant chosen in order to explore optimally the branches. If $u_i \leq -k$ we decide that the correct direction is 1. If $u_i \geq k$ the direction 2 is chosen. If $-k < u_i < k$ both directions are considered.

After the scanning of all the nodes, a subset of synthetic templates is selected, and their distances (in terms of the difference with the observed spectrum) are computed. Then, the parameters of the observed spectrum are determined by computing a weighted mean on the selected spectra, taking into account these distances, setting:

$$W_i^n = \left(1 - \left[\sum_{\lambda} O_i(\lambda) - S_n(\lambda) \right]^2 \right)^p \quad (3)$$

The value p of the exponent is rather arbitrary. Following K11, where it was found that $p = 64$ gave the best results, the same value was adopted in what follows.

DEGAS has a key role in the pipeline used for the RAVE DR4 analyses. Because of its pattern recognition approach, it is exploring more efficiently the parameter space than other mathematical methods, and as a consequence, is less affected by secondary minima in the distance function. Hence, given a roughly normalised spectrum at the rest frame, DEGAS is used in order to achieve a good normalisation for the data, using the synthetic spectrum corresponding to the intermediate solution found.

Once DEGAS has converged on a set of parameters, the new parameters are used to re-normalise the spectrum given the intermediate solution template. The re-normalisation process might need several iterations until the shape of the continuum stays unchanged from one normalisation to another. The number of needed iterations may vary from three to ten. In the case where the distance function has many secondary minima (low SNR spectra and/or low metallicity stars) the results of DEGAS at that stage are the most accurate among the other methods. Nevertheless, it has been shown in K11

that MATISSE manages to better interpolate between the grid points when the astrophysical information is sufficient in the spectra. Thus, once the shape of the continuum has converged, the mean SNR per pixel is estimated in the same way as in Zwitter et al. (2008), and in the case of high SNR spectra MATISSE is run to get more precise atmospheric parameters. The SNR threshold at which MATISSE is run has been established in K11 to be $\text{SNR} = 30 \text{ pixel}^{-1}$.

3.3. MATISSE: a projection method for the high SNR regimes

The MATISSE algorithm (*MATRIX Inversion for Spectral Synthesis*) is a local multi-linear regression method. It estimates a $\hat{\theta}_i$ stellar atmospheric parameter ($i \equiv T_{\text{eff}}, \log g, [\text{M}/\text{H}]$) by projecting the observed spectrum $O(\lambda)$ on a particular vector $B_{\theta}(\lambda)$ associated to a theoretical θ_i parameter, as follows:

$$\hat{\theta}_i = \sum_{\lambda} B_{\theta_i}(\lambda) \cdot O(\lambda) \quad (4)$$

These vectors, called $B_{\theta}(\lambda)$ functions hereafter, are computed during a learning phase. They relate, in a quantitative way, the pixel-to-pixel flux variations in a spectrum to a given variation of the θ_i parameter. In the case where the $B_{\theta}(\lambda)$ are orthogonal, the effects due to each parameter affect the spectrum in an independent way, and hence the atmospheric parameters are derived accurately. When this is not the case (as in most applications), possible degeneracies in the parameter space can occur, causing a correlation of the parameter errors.

The $B_{\theta}(\lambda)$ functions are computed within a given range of parameters, from an optimal multi-linear combination of theoretical, synthetic spectra $S(\lambda)$, as follows:

$$B_{\theta_i}(\lambda) = \sum_j \alpha_{ij} \cdot S_j(\lambda) \quad (5)$$

where the α_{ij} factor is the weight associated with each synthetic spectrum $S_j(\lambda)$, in order to retrieve the $\hat{\theta}_i$ parameter. The weights are computed during the learning phase by applying Eq. 4 to a subset of synthetic spectra. Thus, combining Eq. 4 and 5, one obtains:

$$\Theta_i = C \alpha_i \quad (6)$$

where $C = [c_{jj}]$ is the correlation matrix and Θ_i the vector of the parameters θ_i for all the considered spectra. The weights α_{ij} are then obtained by inverting the correlation matrix C . As explained in K11, a direct inversion of C would take into account all the available spectral signatures, including the smallest ones. Nevertheless, in the case of noisy spectra some lines become insignificant and should hence be discarded from the analysis. In order to achieve that, we adopt here the same approach as in K11 which used the Landweber algorithm to iteratively invert C . By stopping the inversion procedure at different convergence values, smaller weights are then applied to the most insignificant lines which allows the solution to be less affected by secondary minima in the distance function. Extensive analysis of the parameter space for spectra of different SNR values allowed adoption of a different set of $B_{\theta}(\lambda)$ functions for different SNR

values, and hence achieved enhanced accuracy in the parameter determination (see K11 for further details).

The convergence of the algorithm works as follows: if the projection of the observed spectrum on a set of $B_\theta(\lambda)$ gives results that are not within the parameter ranges for which these $B_\theta(\lambda)$ have been computed, then a new set of $B_\theta(\lambda)$ is used, centred on the previous solution. This step is repeated until the results stay within the parameter range of applicability of the projection vectors. In the case where the distance function is convex, less than five iterations are usually needed to reach the absolute minimum, but in some cases of degeneracy in the distance function, the algorithm might not converge (these spectra are then flagged and should not be used from the catalogue, see Sect. 6.1).

As noted previously, MATISSE has the advantage of interpolating accurately between the learning grid points, achieving a good parameter estimation at the high SNR regimes. Nevertheless, local projection methods such as MATISSE have, in general, two main disadvantages. The first consists in not exploring entirely the parameter space, and hence being easily trapped in secondary minima of the distance function if there is a lot of noise in the spectrum. The second disadvantage is that it can extrapolate results outside the boundaries of the learning grid. These two undesired effects are attenuated with the parallel use of DEGAS. Indeed, as described in Sect. 3.2, DEGAS is first used to converge towards a sub-region of the parameter space. Then, for the lowest SNR spectra or when the derived MATISSE parameters are outside the grid's limits, the results of DEGAS are adopted, and MATISSE is not implemented³.

3.4. The grid of synthetic spectra for the learning phase of the pipeline

The very high resolution grid computed in K11 has been convolved with a Gaussian kernel, in order to obtain a new synthetic library at $R = 7500$ ⁴, with a constant wavelength step of 0.35\AA and covering the wavelength range of $[8450.80-8746.55]\text{\AA}$. In addition, the cores of the Ca II lines have been removed from the synthetic spectra, corresponding to one pixel for the first Ca II line and 2 pixels for the other two lines. This removal is justified since the cores of the lines are formed in the upper stellar atmospheric layers where some modelling assumptions like the Local Thermodynamical Equilibrium (LTE) or hydrostatic equilibrium might not be valid hypotheses anymore. The flux disagreement with real spectra for these pixels can induce the algorithms to converge to false minima and hence the cores must be discarded (see K11 for further details).

³ the stars for which DEGAS parameters have been adopted after MATISSE has given parameters outside the grid boundaries are flagged as well, and should be used with caution.

⁴ We note that the effective resolution of RAVE can in reality vary from $6500 < R < 8500$, the changes being a function of both time and position on the CCD. Nevertheless, simple tests, degrading the S^4N library (see Sect. 4.5) to $R \sim 6500, 7500$ and 8500 and then analysis as if the spectra were at $R \sim 7500$, show that the effect on the parameter estimation was of the second order. We hence did not take into account these resolution changes for DR4. However, future data releases will implement these second order effects.

We recall that the synthetic library has been computed using the 1D, LTE and hydrostatic equilibrium MARCS model atmospheres (Gustafsson et al. 2008), in combination with the Turbospectrum code (Alvarez & Plez 1998). The atomic line list has been calibrated on high SNR and high resolution spectra of the Sun and Arcturus (Braut & Neckel 1987; Hinkle et al. 2003), assuming the Solar abundances of Grevesse (2008), except for CNO where we used the values of Asplund et al. (2005). The molecular line list includes ZrO, TiO, VO, CN, C₂, CH, SiH, CaH, FeH and MgH lines with their corresponding isotopic variations (kindly provided by B. Plez).

The reference grid spans effective temperatures from 4000 K to 8000 K with a constant step of 250 K and surface gravities from 0.0 dex to 5.0 dex with a constant step of 0.5 dex. In addition, the library spans with a constant step of 200 K effective temperatures from 3000 K to 4000 K, and surface gravities from 0.0 dex to 5.5 dex. As far as the metallicities are concerned, the number of grid models has increased compared to K11. Instead of having a variable metallicity step, ranging from 0.25 dex for the most metal-rich stars, to 1 dex for the stars with $[M/H] < -3$ dex, the new grid has a constant metallicity step of 0.25 dex for all the metallicities ranging from $[-5.0; +1.0]$ dex. These new spectra, whose atmospheric models did not exist in the MARCS database, have been linearly interpolated from the existing synthetic spectra.

One of the noticeable differences between previous data releases and DR4 is that, in this work, only three parameters are independent in the grid: the effective temperature: T_{eff} , the logarithm of the surface gravity: $\log g$, and the overall metallicity: $[M/H]$. This restriction decreases the number of the secondary minima of the distance function, hence increasing the accuracy of the parameter derivation. It should be noted though that the microturbulent velocity (ξ) is not constant within the grid, but is changed in lock-step with the gravity of the stars. Dwarfs ($\log g \geq 3.5$ dex) have a microturbulent velocity of $\xi = 1 \text{ km s}^{-1}$, whereas giants have $\xi = 2 \text{ km s}^{-1}$. Abundances of the α -elements⁵ are also changed systematically with metallicity, being scaled on the iron abundance, $[Fe/H]$, following the standard α -enhancement found for the metal-poor stars of the Milky Way (thick disc and halo):

- $[\alpha/Fe]=0.0$ dex for $[Fe/H] \geq 0.0$ dex
- $[\alpha/Fe]=-0.4 \times [Fe/H]$ dex for $-1 \leq [Fe/H] \leq 0$ dex
- $[\alpha/Fe]=+0.4$ dex for $[Fe/H] \leq -1.0$ dex.

In addition, spectra for which the parameter combinations did not correspond to realistic astrophysical stars have been removed from the learning grid and hence from the solution space as well. To minimise the importance of our astrophysical priors in the derived parameters, we removed only the templates with $\log g = 5$ dex and $T_{\text{eff}} > 6250$ K, those with $T_{\text{eff}} \leq 4250$ K and $4 \leq \log g \leq 3$ dex, as well as all stars with $[M/H] \leq -3$ dex, $T_{\text{eff}} \leq 4000$ K and $\log g \leq 4$ dex.

⁵ The chemical species considered as α -elements are O, Ne, Mg, Si, S, Ar, Ca and Ti.

These criteria correspond to excluding very young stars with extremely metal-poor abundances (age < 0.5 Gyr and $[\text{Fe}/\text{H}] < -2.5$ dex), as well as old stars that are extremely metal-rich (age > 14 Gyr and $[\text{Fe}/\text{H}] > 0.75$ dex). The final grid contains 3580 spectra of 839 pixels each.

Based on this grid, a subset of reference models can be selected, according to the additional information that is available for each data set to be treated. In the case of RAVE, the 2MASS photometric information that is available for the observed targets is used to exclude some parameter combinations from the solution space corresponding to derived temperature ranges which are grossly inconsistent with the photometric colour. In practice, the RAVE spectra have been separated into four different colour ranges. Then, according to their 2MASS ($J - K_s$) colour, a set of solutions has been imposed as soft photometric priors for every analysed spectrum, defining:

- $(J - K_s) > 0.75 \Rightarrow T_{\text{eff}} < 4500$ K
- $0.4 < (J - K_s) < 0.75 \Rightarrow 3750 < T_{\text{eff}} < 6000$ K
- $(J - K_s) < 0.4 \Rightarrow T_{\text{eff}} > 5250$ K.

The few stars for which no 2MASS photometry was available (less than 2%) form a fourth category for which there is no prior on the solution space.

The above mentioned effective temperature ranges have been determined by requesting a colour-magnitude diagram of the Galaxy from the web interface⁶ of the Padova database with the 2MASS photometric system. Then, for the above three colour ranges we inferred the full range of effective temperatures of the simulated stars, and increased these limits by ± 500 K. We note that the effective temperature bins have been made deliberately large, because neither the photometric errors nor the extinction have been taken into account when separating the spectra into colour bins.

3.5. Computation of the internal uncertainties

The total uncertainty of the pipeline for a given star is the quadratic sum of its internal and external errors. The internal uncertainties relate the capacity of an algorithm to treat spectral degeneracies and SNR, whereas external uncertainties concern the difference between the template synthetic spectra and the true stellar spectra (see Sect. 4.6).

Following K11 the internal uncertainties of the algorithm have been estimated by computing a set of spectra of realistic Galactic populations. Based on the Besançon Galactic model, a simulated catalogue of stars towards three different Galactic directions (Galactic centre, north Galactic pole and intermediate Galactic latitudes) has been constructed, from which 10^4 stars have been randomly selected to be our realistic Galactic sample. In addition, in order to explore different metallicity regimes, each star has been replicated in the catalogue, with its partner having reduced (by -0.75 dex) metallicity. The 2×10^4 synthetic spectra corresponding to these parameter combinations have been computed thanks to the interpolation capabilities of MATISSE, and

four different values of white Gaussian noise were added to them (SNR=100, 50, 20, 10 pixel⁻¹). Given these final 8×10^4 spectra, the pipeline was run in order to retrieve the associated errors.

In order to simulate the way the RAVE spectra are analysed, the pipeline was run twice. Once without any photometric prior (see Table 1), and once by imposing soft priors (see Table 2), based on their temperatures. These priors have been selected in order to be similar with the ones that are applied in the analysis of the RAVE spectra (see Sect. 3.4). The error values for different stellar types, presented in Tables 1 and 2, have been computed as the 70th percentile of the error distribution. Indicative atmospheric parameter uncertainties for typical thin disc dwarfs, thick disc dwarfs and halo giants are also given in the last three lines of these tables. A comparison of the uncertainty values with or without photometric priors shows that when the spectral degeneracy is important, the applied soft priors improve significantly the associated uncertainties (see for example the hot, metal-poor dwarfs). In addition, it has been noticed, as expected, that the use of the soft photometric priors improve the 90th percentile of most of the stellar categories considered in these tables.

The way the internal errors are associated with a specific parameter estimation is as follows: once the pipeline has converged towards a set of parameters, the final SNR is computed as in Zwitter et al. (2008), utilising the associated solution template. According to the SNR, the stellar type, the luminosity class, its metallicity, and the use or not of 2MASS photometric prior, the equivalent internal error estimations in one of the Tables 1 or 2 are adopted. We note that this approach does not optimally take into account the properties of the distance function and hence the degeneracies. Nevertheless, we find that in the case of spectral degeneracy, the associated errors are larger, being consistent with what is expected.

3.6. Description of the observed input spectra

The extraction and reduction procedures applied to the observed spectra are as described in Steinmetz et al. (2006); Zwitter et al. (2008). As far as the normalisation and rest-frame corrections are concerned, we have used the results and the raw data coming from DR3, details of which can be found in Siebert et al. (2011b) and for which the general properties are summarised in Sect. 8. In addition, in order to be able to perform a pattern recognition and a pixel-to-pixel comparison with the spectra of the learning grid, the RAVE spectra have been interpolated at the wavelengths of the templates and the cores of the IR Ca II triplet lines have been removed (see Sect. 3.4).

Since the DR4 pipeline re-normalises the observed spectra, initially erroneous or inaccurate continuum shapes do not influence the final parameter accuracy of DR4. One might worry about the accuracy of the radial velocity of the stars, and hence their rest-frame correction. Indeed, the radial velocities have been computed using cross-correlation with the solution template derived in DR3, whereas in the present work, the atmospheric parameters are recomputed, leading to different values. Nevertheless, the pipeline requires a radial velocity precision only better than $\sim 7 - 10$ km s⁻¹ (see

⁶ <http://stev.oapd.inaf.it/cmd>

TABLE 1
INTERNAL ERRORS AFTER RE-NORMALISATIONS **without** PHOTOMETRIC PRIORS

SNR (per pixel)	T_{eff} (K)				$\log g$ (dex)				$[M/H]$ (dex)			
	100	50	20	10	100	50	20	10	100	50	20	10
KII-IV, $[M/H]>-0.5$ dex	72	76	117	201	0.12	0.13	0.20	0.48	0.08	0.08	0.10	0.23
KII-IV, $-1<[M/H]<-0.5$ dex	62	85	133	302	0.14	0.20	0.35	0.72	0.08	0.09	0.16	0.30
KII-IV, $-2<[M/H]<-1$ dex	75	96	178	330	0.20	0.30	0.57	0.97	0.09	0.11	0.19	0.33
KII-IV, $[M/H]<-2$ dex	78	105	184	382	0.31	0.40	0.76	1.26	0.09	0.10	0.20	0.37
GII-IV, $[M/H]>-0.5$ dex	78	111	233	402	0.09	0.20	0.40	0.69	0.07	0.09	0.15	0.35
GII-IV, $-1<[M/H]<-0.5$ dex	81	110	241	426	0.15	0.25	0.54	0.98	0.08	0.10	0.17	0.44
GII-IV, $-2<[M/H]<-1$ dex	98	164	282	472	0.25	0.46	0.74	1.08	0.10	0.13	0.23	0.43
GII-IV, $[M/H]<-2$ dex	187	248	375	553	0.37	0.61	0.99	1.07	0.17	0.26	0.49	0.60
FII-IV all $[M/H]$	79	73	138	140	0.14	0.13	0.14	0.15	0.09	0.09	0.10	0.27
KV, $[M/H]>-0.5$ dex	66	69	92	171	0.11	0.14	0.22	0.34	0.08	0.09	0.09	0.21
KV, $-1<[M/H]<-0.$	75	85	112	225	0.15	0.17	0.24	0.38	0.09	0.10	0.13	0.30
KV, $-2<[M/H]<-1$	83	98	173	328	0.16	0.19	0.25	0.51	0.09	0.11	0.14	0.35
KV, $[M/H]<-2$ dex	93	133	278	518	0.11	0.17	0.47	1.03	0.06	0.06	0.15	0.38
GV, $[M/H]>-0.5$ dex	67	98	209	344	0.10	0.16	0.33	0.51	0.09	0.10	0.14	0.30
GV, $-1<[M/H]<-0.$	87	147	246	426	0.14	0.22	0.36	0.55	0.09	0.12	0.21	0.38
GV, $-2<[M/H]<-1$	119	181	358	669	0.19	0.32	0.44	0.71	0.11	0.14	0.28	0.54
GV, $[M/H]<-2$ dex	279	435	690	843	0.44	0.54	0.72	1.06	0.26	0.38	0.61	0.80
FV, $[M/H]>-0.5$ dex	81	117	307	493	0.13	0.18	0.34	0.52	0.11	0.13	0.27	0.43
FV, $-1<[M/H]<-0.$	96	151	306	575	0.14	0.21	0.33	0.49	0.11	0.14	0.26	0.48
FV, $-2<[M/H]<-1$	155	257	563	999	0.21	0.30	0.40	0.69	0.13	0.19	0.43	0.83
FV, $[M/H]<-2$ dex	447	641	1046	1165	0.43	0.65	0.84	1.22	0.40	0.53	0.95	1.14
Thin Disc dwarfs	66	89	199	344	0.09	0.14	0.32	0.50	0.09	0.10	0.13	0.29
Thick Disc dwarfs	91	146	280	501	0.14	0.22	0.35	0.52	0.09	0.13	0.24	0.43
Halo giants	90	149	244	443	0.23	0.43	0.70	1.05	0.10	0.13	0.24	0.39

^aLuminosity classes I-II assume $\log g \leq 3.5$, luminosity class V assumes $\log g > 3.5$. Spectral types are defined by T_{eff} ranges as follows: $T_{\text{eff}} < 5000$ K K type, $5000 \leq T_{\text{eff}} < 6000$ K G type, and $T_{\text{eff}} \geq 6000$ K F type stars.

TABLE 2
INTERNAL ERRORS AFTER RE-NORMALISATIONS **with** PHOTOMETRIC PRIORS

SNR (per pixel)	T_{eff} (K)				$\log g$ (dex)				$[M/H]$ (dex)			
	100	50	20	10	100	50	20	10	100	50	20	10
KII-IV, $[M/H]>-0.5$ dex	71	76	112	180	0.12	0.14	0.24	0.50	0.08	0.08	0.11	0.21
KII-IV, $-1<[M/H]<-0.5$ dex	61	86	137	285	0.14	0.20	0.40	0.69	0.08	0.10	0.17	0.29
KII-IV, $-2<[M/H]<-1$ dex	75	96	173	312	0.20	0.31	0.59	1.02	0.09	0.11	0.21	0.34
KII-IV, $[M/H]<-2$ dex	75	101	213	399	0.27	0.35	0.79	0.98	0.10	0.10	0.18	0.32
GII-IV, $[M/H]>-0.5$ dex	78	104	237	332	0.09	0.21	0.48	0.49	0.07	0.09	0.18	0.26
GII-IV, $-1<[M/H]<-0.5$ dex	79	103	238	412	0.15	0.23	0.52	0.97	0.08	0.10	0.17	0.37
GII-IV, $-2<[M/H]<-1$ dex	90	158	283	412	0.21	0.45	0.78	1.05	0.11	0.12	0.23	0.33
GII-IV, $[M/H]<-2$ dex	203	265	378	479	0.33	0.61	0.91	1.14	0.15	0.25	0.49	0.54
FII-IV all $[M/H]$	79	83	93	138	0.14	0.13	0.14	0.26	0.09	0.09	0.09	0.31
KV, $[M/H]>-0.5$ dex	66	69	92	168	0.11	0.15	0.22	0.36	0.08	0.09	0.09	0.20
KV, $-1<[M/H]<-0.5$ dex	75	84	110	219	0.15	0.17	0.23	0.38	0.09	0.10	0.12	0.29
KV, $-2<[M/H]<-1$ dex	82	97	172	293	0.16	0.19	0.23	0.52	0.08	0.10	0.14	0.33
KV, $[M/H]<-2$ dex	92	144	240	480	0.11	0.17	0.46	0.54	0.07	0.07	0.17	0.39
GV, $[M/H]>-0.5$ dex	66	95	203	316	0.10	0.15	0.35	0.55	0.09	0.10	0.15	0.30
GV, $-1<[M/H]<-0.5$ dex	85	144	238	360	0.14	0.22	0.38	0.55	0.09	0.12	0.20	0.33
GV, $-2<[M/H]<-1$ dex	101	169	291	441	0.15	0.28	0.43	0.62	0.10	0.13	0.24	0.39
GV, $[M/H]<-2$ dex	220	317	393	480	0.35	0.46	0.53	0.80	0.21	0.30	0.39	0.50
FV, $[M/H]>-0.5$ dex	66	94	257	464	0.13	0.18	0.38	0.56	0.10	0.11	0.25	0.41
FV, $-1<[M/H]<-0.5$ dex	84	127	277	498	0.14	0.21	0.35	0.52	0.09	0.13	0.25	0.43
FV, $-2<[M/H]<-1$ dex	104	182	440	601	0.18	0.25	0.38	0.53	0.11	0.15	0.32	0.51
FV, $[M/H]<-2$ dex	331	503	617	678	0.32	0.51	0.54	0.66	0.33	0.48	0.54	0.69
Thin Disc dwarfs	61	85	183	330	0.09	0.14	0.33	0.53	0.09	0.10	0.12	0.30
Thick Disc dwarfs	84	133	256	406	0.14	0.21	0.38	0.54	0.09	0.12	0.22	0.37
Halo giants	83	143	258	399	0.21	0.41	0.74	1.04	0.10	0.12	0.24	0.38

K11) in order not to be affected by Doppler shifts in the parameter estimation. This threshold is much higher than the accuracy of the radial velocities coming from the DR3, where 95% of the sample has errors of less than $\sim 4 \text{ km s}^{-1}$ and 98% less than 7 km s^{-1} (Siebert et al. 2011b, and Sect. 8). Thus, we can assume that the spectra are indeed at the rest frame for the purpose of our analysis.

4. VALIDATION OF THE PARAMETERISATION WITH EXTERNAL DATA SETS

Up to here in this paper, only the internal performances of the pipeline have been discussed. Nevertheless, any given pipeline based on a grid of synthetic spectra needs to be verified and calibrated on observed spectra with high SNR, and well-determined parameters. The grid of synthetic spectra that has been used for this work has been computed with an atomic line list calibrated on the high-resolution and high-SNR spectra of the Sun and Arcturus of Brault & Neckel (1987); Hinkle et al. (2003). However, these calibrations concern only two particular stars, and further investigation needs to be done in order to correct possible biases in the parameter's estimation. In order to calibrate the T_{eff} , $\log g$ and $[M/H]$, instead of going through the process of calibrating all the lines for many reference stars and improve the quality of the atmosphere modelling, one can also validate the pipeline's parameter results with reference parameter measurements from the literature.

This calibrating data set needs to cover as much as possible the parameter space investigated by the survey. Ideally the calibration of the parameters would be done using only RAVE spectra of suitable standards, but RAVE-like spectra, at the same resolution and (if possible) reduced in the same manner, can be sufficient in the case where not enough calibration spectra are available.

4.1. The calibration data sets of observed spectra

First, the RAVE database has been explored to find spectra of stars which had atmospheric parameter determinations available from high-resolution spectroscopy. For that purpose, we made extensive use of the heterogeneous PASTEL catalogue⁷ to identify such targets, retrieving roughly 400 star candidates. Following Soubiran et al. (2010), we considered only the reference values coming from Fuhrmann (1998a,b, 2004, 2008); Gratton et al. (1996, 2003); Hekker & Meléndez (2007); Luck & Heiter (2006, 2007); McWilliam (1990); Mishenina & Kovtyukh (2001); Mishenina et al. (2004, 2006, 2008); Ramírez et al. (2007); Valenti & Fischer (2005). These studies, when considered by author, all include a large number of stars (at minimum 222 stars), and are all analysed in a homogeneous way. This allows to minimise the discrepancies between the sub-catalogues of PASTEL. When for a given star several measurements were available, the mean was computed and the dispersion of the parameters has been considered as the uncertainty on the reference values. We kept only those stars for which measurements were available for the three parameters from a single study, and for which the dispersions among the literature values were less than 100 K, 0.2 dex and

0.1 dex for T_{eff} , $\log g$ and $[M/H]$, respectively. In total, 169 stars were selected that way, mainly dwarfs of intermediate metallicity.

In order to investigate the pipeline's behaviour in the low metallicity regime for giant stars, we chose to use the parameters of 229 thick disc stars analysed by Ruchti et al. (2011), as well as 163 stars observed by Fulbright et al. (in prep.). The targets of both of these data sets are drawn from RAVE, while the stellar parameters have been obtained from an equivalent-width analysis of high resolution spectra. In addition, the very metal-poor giant star CD-38245 ($[M/H] = -4.2$ dex, Cayrel et al. 2004), which has been observed twice by RAVE, has been included in the list, in order to calibrate the results at the very metal-poor regime.

Metal-rich giant stars have been explored thanks to the CFLIB library (Valdes et al. 2004). The entire spectral library was downloaded from the webpage⁸ of that project, excluding only spectra which did not include the wavelength range around the IR Ca II triplet. The final comparison catalogue is the same as in K11, where once again, we used the updated values that can be found in the PASTEL database, and discarded the stars for which the dispersion in the literature values were greater than 100 K, 0.2 dex and 0.1 dex for T_{eff} , $\log g$ and $[M/H]$, respectively.

Finally, in order to have a more significant statistical sample at the high-metallicity regime, we used the 2.3m telescope at the Siding Spring Observatory (SSO) to obtain spectra of stars belonging to open clusters. Although the data have not been obtained with the same instrument, the same reduction pipeline has been used as for the RAVE spectra. For calibration purposes, we have used 16 RAVE-like SSO spectra of giant stars belonging to the open cluster M67 and 12 RAVE-like SSO spectra of giants belonging to the open cluster IC4651, with a few additional data sets used as testing sets (see Sect. 4.5). These targets were selected given their positions, colours and radial velocities when available, prioritising bright stars in order to have high SNR spectra. For these stars, no individual atmospheric parameters were available, but their metallicity is expected to have a small dispersion around their mean open cluster metallicity value.

In total, 809 stars are used as calibrators, each having $\text{SNR} > 40 \text{ pixel}^{-1}$. The final number of spectra used from each data set is summarised in Table 3 and their reference and retrieved $T_{\text{eff}} - \log g$ diagrams are plotted in Fig. 5.

4.2. Validation of the effective temperatures and surface gravities

Figures 5 and 6 show the comparison between the reference values found in the literature and those found with the present pipeline for all the data sets except those for open cluster members (where no reference values were available). As far as the effective temperature is concerned, good agreement is found, with a mean offset of 15 K and a dispersion of roughly 400 K. On the other hand, the agreement is less good for the surface gravity, with a rather big scatter for the giant stars. This effect is a manifestation of the previously cited spectral degeneracy which is present for the low and intermediate

⁷ <http://pastel.obs.u-bordeaux1.fr/>

⁸ <http://www.noao.edu/cflib/>

TABLE 3
CALIBRATION DATA SETS WITH $\text{SNR} > 40 \text{ PIXEL}^{-1}$

Dataset	Object	N spectra	[Fe/H]	Reference for the stellar parameters
IC 4651	open cluster	6	+0.10	Pasquini et al. (2004)
M67	open cluster	16	+0.05	Pancino et al. (2010)
CFLIB	dwarfs & giants	224	$[-1.0, 0.0]$	PASTEL database
CD-38245	$T_{\text{eff}}=4800 \text{ K}$, $\log g=1.5$	2	-4.2	Cayrel et al. (2004)
Ruchti et al. (2011) ^a	giants & dwarfs	229	$[-2.5; -0.5]$	Ruchti et al. (2011)
Fulbright et al.	giants	163	$[-2.5; 0.0]$	Fulbright et al. (in prep.)
RAVE spectra	giants & dwarfs	169	$[-1.5; 0.0]$	PASTEL database

^aFor the Ruchti et al. (2011) catalogue we selected stars with $[M/H] > -2.5$ dex and $\log g < 3$, and stars with $[M/H] < -0.8$ dex and $\log g > 3$.

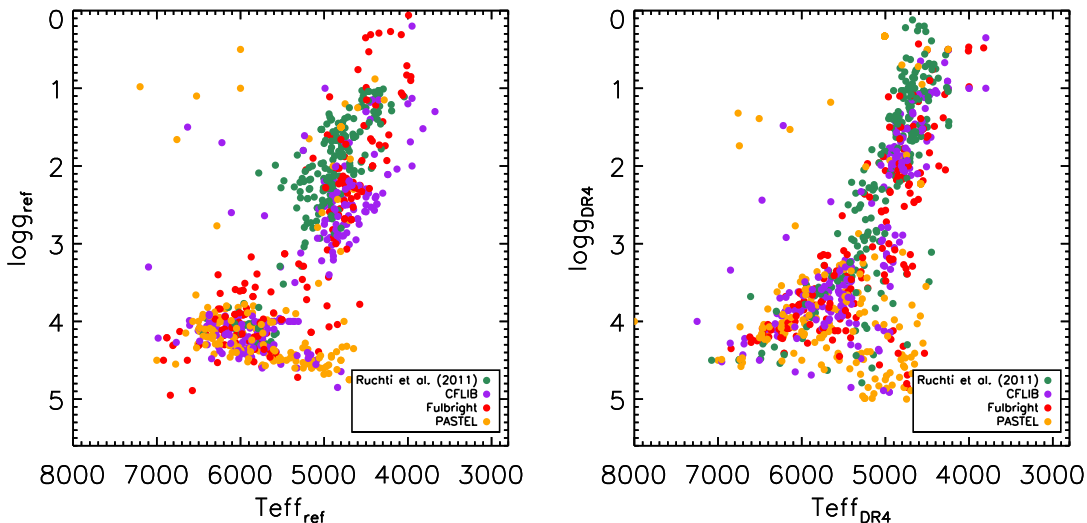


FIG. 5.— Surface gravity ($\log g$) versus effective temperature (T_{eff}) diagram of the calibration data sets for which we have parameter estimations coming from high-resolution spectroscopy. At the left hand side are represented the values found in the literature, whereas on the right hand side are plotted the results obtained from the DR4 pipeline.

resolution spectra around the IR Ca II triplet. According to the stochastic position of the noise on the spectrum, a metal-rich turn-off star can be easily confused with a star on the sub-giant branch of lower metallicity. Unless precise photometric temperatures are known, this degeneracy cannot be lifted using medium resolution spectrum alone and is a true degeneracy. Nevertheless, as noted in the previous sections, the DR4 pipeline takes advantage of the 2MASS photometric information (see Sect. 3.4), hence partly reducing the effect of these degeneracies.

Discussion on the effective temperature scale— In order to verify the determination of the effective temperatures, we compared the DR4 values of RAVE spectra with $\text{SNR} > 20 \text{ pixel}^{-1}$ for 327 stars in common with the photometric effective temperatures from the Casagrande et al. (2010) calibration of the Geneva-Copenhagen Survey (GCS, Nordström et al. 2004a). Figure 7 shows on one hand a small dispersion of the DR4 pipeline’s effective temperatures when comparing with the values published by Casagrande et al. (2011) for the GCS but on the other hand there is a constant underestimation of $\sim 170 \text{ K}$. Nevertheless, since the GCS covers only a limited range of the parameter space (only metal-rich

dwarfs), and because any such offset is not seen with the other calibration data sets, it has been decided not to apply any correction to the RAVE T_{eff} scale. We note though that the user of the DR4 effective temperatures should be aware that in order to be in agreement with the Casagrande et al. (2010) effective temperature scale, for the type of stars analysed by the GCS, an offset correction should be performed.

4.3. Overall metallicity calibration

In order to investigate the calibration needs for the metallicities, we used the iron abundances ($[\text{Fe}/\text{H}]$) from the literature. Indeed, we recall that the iron-peak and the α -element abundances of the synthetic spectra are scaled to the iron abundance. Since the metallicity measurement is dominated by the Ca II lines (which correspond to an α -element), in our case and for standard Galactic α -abundances (*i.e.* following the trend defined in Sect. 3.4) we have: $[\text{M}/\text{H}]_{\text{DR4}} \approx [\text{Fe}/\text{H}]$. Nevertheless, for non-standard stars, the overall metallicity will not be equal to the iron abundance, and hence it has been decided to keep in what follows the notation $[\text{M}/\text{H}]$ instead of $[\text{Fe}/\text{H}]$. In what follows, the nomenclature of the DR3 paper is adopted, denoting the raw metallicity estimation

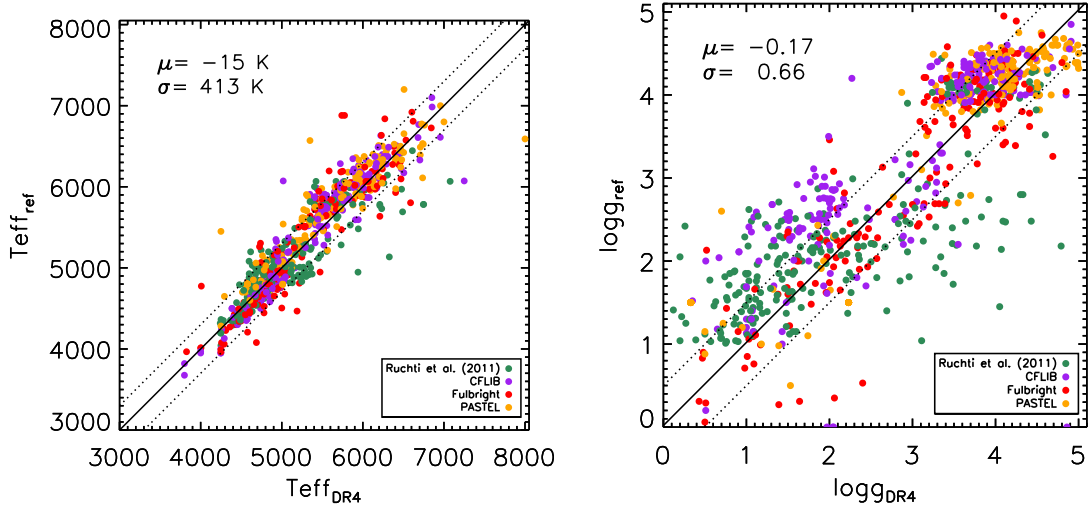


FIG. 6.— Comparison of the reference values found in the literature and the derived effective temperatures (left hand side) and surface gravities (right hand side). Colour coding for each data set is the same as in Fig. 5. Dotted diagonal lines represent offsets from unity of ± 300 K and ± 0.5 dex for T_{eff} and $\log g$, respectively. The mean offsets (μ) and the dispersions (σ) are indicated in the upper left corner of each plot.

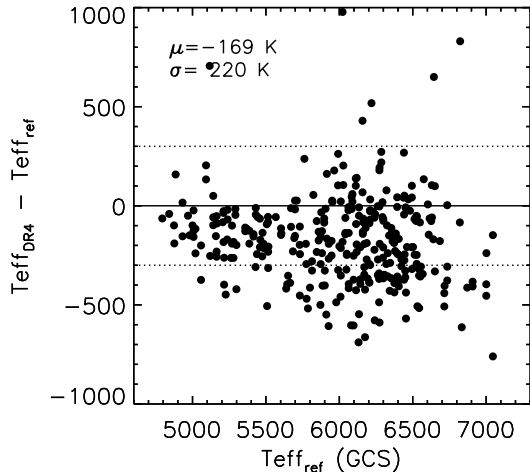


FIG. 7.— Comparison of the effective temperatures found by the DR4 pipeline for RAVE spectra of stars that are part of the Geneva-Copenhagen Survey with the updated values of Casagrande et al. (2011). The constant offset of ~ 170 K shows that DR4 is not on the same effective temperature scale.

of the DR4 pipeline as $[m/H]$, and the calibrated (final) metallicity as $[M/H]$. Comparison of the reference values and those derived by the DR4 pipeline is presented in the left panel of Fig. 8.

The results of Fig. 8 have been obtained with all the data sets of Table 3, assuming the metallicities given in the fourth column of that table. From the left hand side plot of Fig. 8 one can notice that there is an offset between the derived metallicities from the RAVE spectra and the reference iron abundances. This bias is not the same for all metallicities, and it is more important for metal-poor stars than in the metal-rich regime. We investigated the correlations of the errors, and found that the main parameters driving the bias are the surface gravity and the metallicity itself. Figure 9 illustrates the covari-

ance of the residual errors on the metallicity with respect to the surface gravity, for different metallicity ranges. In this figure, each point and error bar represent the median and the dispersion of the metallicity error for the stars inside each gravity bin. This binning approach smooths the errors, minimises the impact of outliers and highlights the general trends of the biases. On one hand, the results of Fig. 9 show for the lowest metallicities a rather constant underestimation of the metallicity by 0.2 dex. On the other hand, there are some clear trends in the more metal-rich regimes, where the giant stars exhibit higher offsets than the dwarfs. These trends are too strong to be explained by a variation of microturbulent velocity along the giant branch, where the expected offsets should be less than 0.1 dex (see for example Kirby et al. 2009).

Using the binned points of Fig. 9, the resulting fit of a quadratic surface for the errors in metallicity, taking into account the dependences on both the surface gravity and the metallicity, is:

$$[m/H] - [M/H]_{\text{ref}} = -0.076 - 0.006 * \log g + 0.003 * \log^2 g - 0.021 * [m/H] * \log g + 0.582 * [m/H] + 0.205 * [m/H]^2. \quad (7)$$

Given this relation, the trend for the typical mean metallicity inside each box of Fig. 9 has been plotted in blue. As expected, the fits are in good agreement with the offsets, hence assimilating the metallicity calibration relation to Eq. 7. The right panel of Fig. 8 shows the improvement that has been made on the metallicity determination thanks to the correction of Eq. 7. We note, however, that due to the lack of reference stars with super-solar metallicities, our calibration is not optimal for $[M/H] > +0.1$ dex. This limitation will be addressed in a future study.

A more detailed investigation of the residuals for different gravity regimes and with respect to the calibrated metallicity is shown in Fig. 10, for the Ruchti, Fulbright,

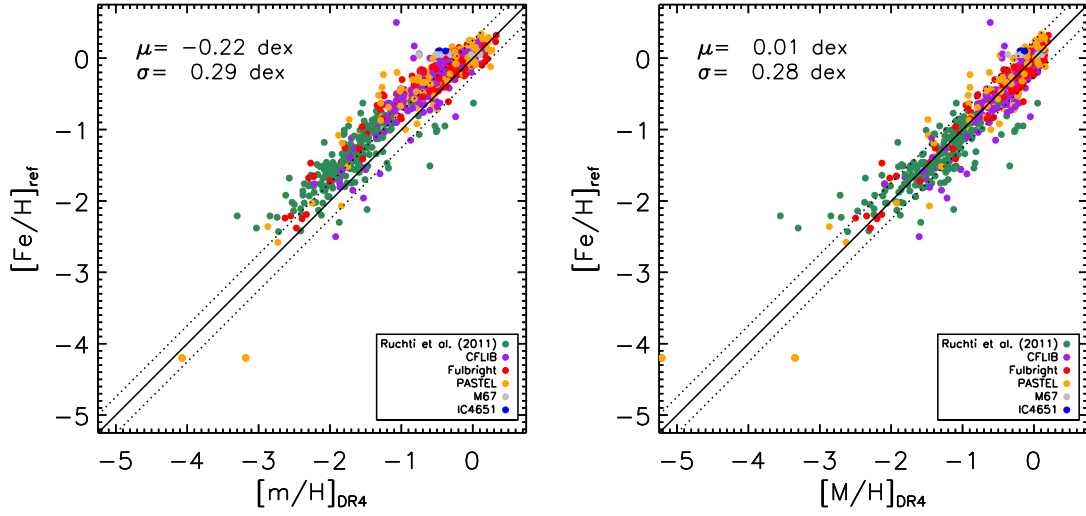


FIG. 8.— Comparison between the reference iron abundances found in the literature ($[\text{Fe}/\text{H}]_{\text{ref}}$) and the derived overall metallicities ($[\text{m}/\text{H}]_{\text{DR4}}$, left hand side) and the calibrated overall metallicities ($[\text{M}/\text{H}]_{\text{DR4}}$, right hand side), according to Eq. 7. Colour coding for each data set is the same as in Fig. 5. Dotted diagonal lines represent offsets from unity of ± 0.25 dex.

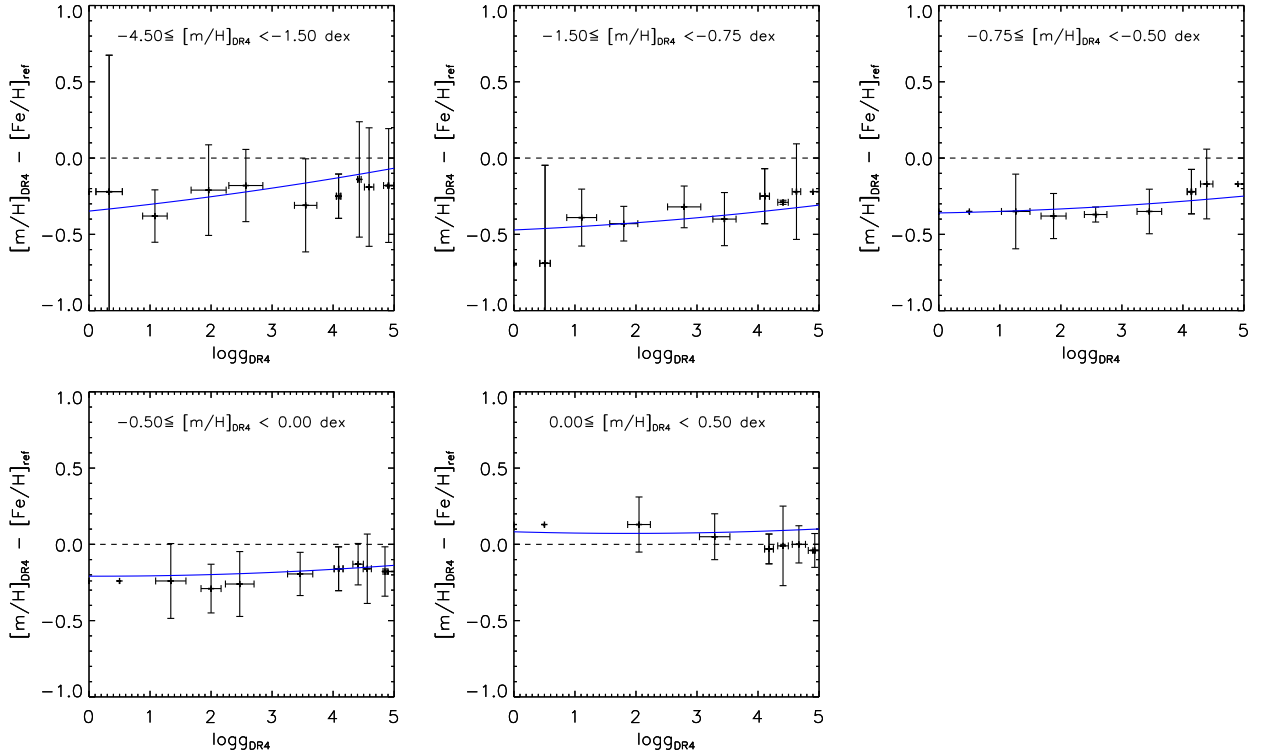


FIG. 9.— Trends in the metallicity determination for different gravity bins, at different metallicity ranges. The error bars correspond to the dispersion of $\log g$ and the error in metallicity inside each bin. The blue lines represent the polynomial that has been adopted in order to best describe the metallicity offsets. It corresponds to the polynomial of Eq. 7, and has been computed for the mean metallicity of each subsample.

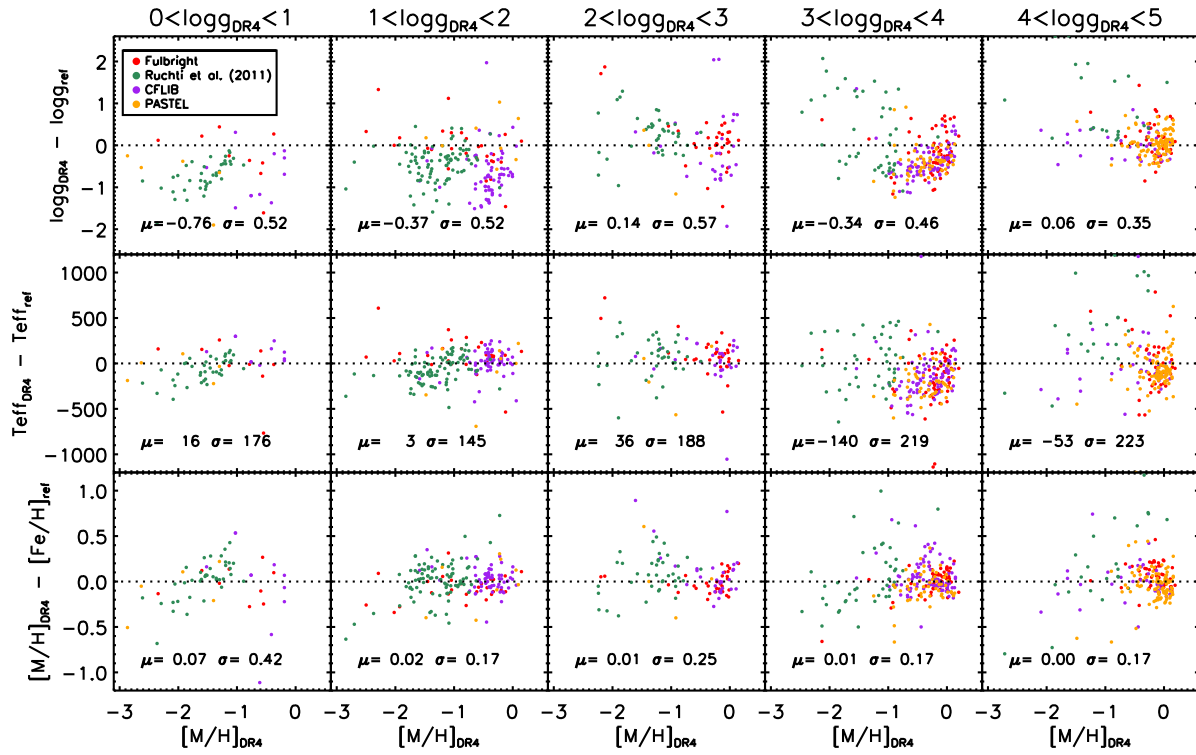


FIG. 10.— DR4 residual plots for RAVE (RAVE-PASTEL in yellow, Ruchti in green and Fulbright in red) and RAVE-like spectra (CFLIB, in purple). The trends in the stellar parameter systematics are shown with respect to the calibrated metallicity, divided into different (DR4) $\log g$ bins of 1 dex. In each panel, the median offset and the dispersion is indicated.

PASTEL and CFLIB libraries. As expected, there is no bias for the calibrated metallicity (lower plots), nor for the other parameters, except for the surface gravity of the lowest gravity giant stars (see also Sect. 6.1). The self-consistency of the calibration is hence validated.

4.4. *A comment on RAVE DR1, DR2, & DR3 parameters*

Previous RAVE data releases used the Munari et al. (2005) grid of synthetic spectra and a penalised χ^2 algorithm in order to determine the effective temperatures, surface gravities, overall metallicities and α -abundances. The stellar rotational velocities (V_{rot}) and the microturbulent velocities (ξ) were also left as free parameters, although without attributing any constraint on these values in the end⁹. Furthermore, the 2MASS photometric information was not used to help reduce spectral degeneracies and the calibration data sets were not fully available.

The present DR4 pipeline reduces the parameter space to only the three free atmospheric parameters we are trying to measure. In addition to imposing a photometric effective temperature range, the new pipeline explores more efficiently the parameter space, thanks to the decision-tree algorithm. This makes the new results more robust and less susceptible to biases caused by spectral degeneracies.

Efficient exploration of the low dimension parameter space is crucial for the accurate determination of the atmospheric parameters, and calibration of the results. Indeed, tests done on the above mentioned calibration data sets, using the DR3 pipeline output, showed that the metallicity biases could not be calibrated adequately, especially for the turn-off stars, where the degeneracy of the distance function is the most important (see Fig. 11). As it will be shown in Sect. 6.3, this lead to biases and interdependences between the DR3 parameters, and motivated the effort to develop the approach implemented here in DR4.

4.5. *Sanity check of the metallicity calibration on a set of observed spectra*

Our proposed metallicity calibration relation (see Eq. 7) has been further verified on spectra that are not part of the calibration process. For that purpose, we used the 327 RAVE spectra of the GCS stars described previously, 105 non-RAVE spectra from the S^4N library degraded to RAVE resolution (Allende Prieto et al. 2004) and 65 RAVE-like spectra of open and globular cluster stars obtained by the 2.3m telescope at the SSO, listed in Table 4. We note though that the reference metallicity values that have been adopted for these test spectra are not as reliable as the calibration data sets. Indeed, except for the S^4N library, all the other data sets do not have individual spectroscopically measured metallicities. In addition, non-member stars might be included in the cluster data sets. Finally, the mean metallicity value has been considered for the stars belonging to the globular clusters, whereas dispersions up to few tenths of a dex (Gratton et al. 2004) can be expected in some cases.

⁹ for DR3 the microturbulent parameter was fixed at $\xi = 2 \text{ km s}^{-1}$.

The three plots of Fig. 12 show the recovered $T_{\text{eff}} - \log g$ diagram of the total considered sample (left), the $\log g$ versus residuals in $[m/H]$ (middle) and versus residuals in calibrated $[M/H]$ (right). Despite the relatively large dispersion due to the heterogeneous quality of the data sets, one can see that the bias is greatly reduced in all the samples, and for all gravities, providing a sanity validation check of the calibration relation established previously.

4.6. *Computation of the total uncertainties of the pipeline*

The errors described in Sect. 3.5 concern only the internal accuracies of the method. To estimate the total uncertainties of the pipeline one needs also to estimate the external errors.

We used all the spectra with $\text{SNR} \geq 50 \text{ pixel}^{-1}$ of the previously described calibration data set to estimate the external uncertainties for different ranges of stellar parameters. Given the total number of spectra in the data set, we divided the sample into cool ($T_{\text{eff}} \leq 6000 \text{ K}$) and hot ($T_{\text{eff}} > 6000 \text{ K}$) dwarfs ($\log g \geq 3.5 \text{ dex}$) and giants ($\log g < 3.5 \text{ dex}$). Furthermore, we also divided into metal-rich ($[M/H] \geq -0.5 \text{ dex}$) and metal-poor ($[M/H] < -0.5 \text{ dex}$) regimes, except for the hot giants for which not enough stars were available in the sample. The dispersion of the residual differences is presented in Table 5, together with the number of stars that have been considered in order to compute these uncertainties.

Using the values presented in Table 5, the total uncertainties of the pipeline parameter determinations are then estimated by adding in quadrature the external errors with the internal errors given in Tables 1 and 2.

5. COMPUTATION OF THE CHEMICAL ABUNDANCES

The atmospheric parameters inferred in the previous sections are used as an input in order to determine abundances of individual elements. For that purpose, we use an improved version of the RAVE chemical pipeline described in detail in Boeche et al. (2011, afterwards B11). Below, we recall the general features of that pipeline, and present the current improvements.

The chemical pipeline relies on an equivalent widths (EWs) library which contains the expected EWs of the lines visible in the RAVE wavelength range (604 atomic and molecule lines). These EWs are computed for a grid of stellar parameters values covering the range $[4000, 7000] \text{ K}$ in T_{eff} , $[0.0, 5.0] \text{ dex}$ in $\log g$ and $[-2.5, +0.5] \text{ dex}$ in $[M/H]$ and five levels of abundances in the range $[-0.4, +0.4] \text{ dex}$ relative to the metallicity, in steps of 0.2 dex (adopting the Solar abundances of Grevesse & Sauval 1998). The chemical pipeline constructs on-the-fly spectrum models by adopting the effective temperatures and surface gravities obtained by the DR4 pipeline (see Sect. 3). It then searches for the best fitting model by minimising the χ^2 between the models and the observations.

For a given normalised, RV corrected and wavelength calibrated spectrum, the chemical pipeline determines the elemental abundances, following the steps described below:

- i) Upload the EWs for the lines at the estimated DR4

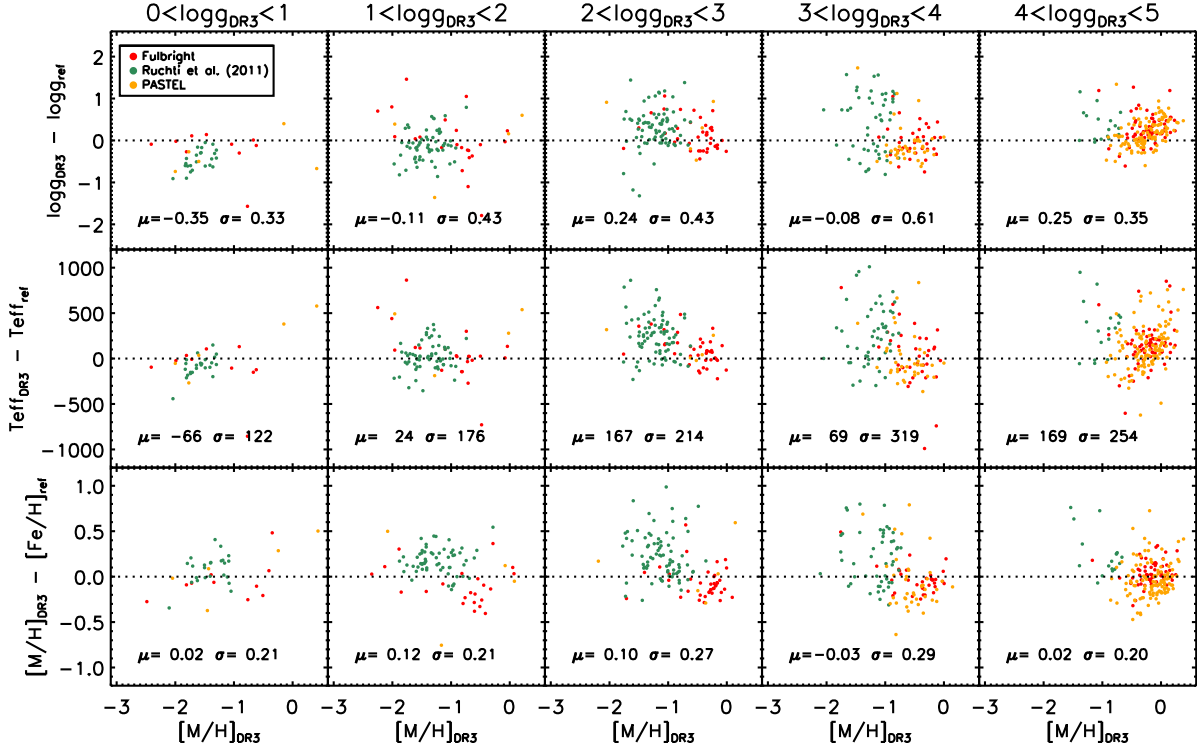


FIG. 11.— Same as Fig. 10 but for the RAVE DR3 pipeline and without the CFLIB analysis. The calibrated metallicities correspond to those obtained using Eq. 2 of Siebert et al. (2011b) with parameters $c_0 = 0.578$, $c_1 = 1.095$, $c_3 = 1.246$, $c_4 = -0.520$. The metallicity trends found for the turn-off stars are representative of the uncalibratable biases present in RAVE DR3.

TABLE 4
POST-CALIBRATION VERIFICATION DATA SETS

Dataset	Type	N stars	$\langle [\text{Fe}/\text{H}] \rangle$	$\sigma([\text{Fe}/\text{H}])$	Reference
M5	globular cluster	8	-1.28	0.11	Ramírez & Cohen (2003)
NGC 3680	open cluster	7	-0.04	0.03	Pace et al. (2008)
IC4651	open cluster	5	+0.10	0.05	Pasquini et al. (2004)
M67	open cluster	10	+0.05	0.04	Pancino et al. (2010)
NGC 6752	globular cluster	12	-1.42	0.10	Gratton et al. (2001)
NGC 2808	globular cluster	10	-1.14	0.06	Carretta et al. (2004)
NGC 6397	globular cluster	11	-2.10	0.05	Koch & McWilliam (2011)
Praesepe	open cluster	35	+0.14	0.04	mean literature value
GCS	MW dwarf stars	327	solar	–	Casagrande et al. (2011)
S^4N	MW dwarf stars	105	solar	–	Allende Prieto et al. (2004)

T_{eff} , $\log g$, $[\text{M}/\text{H}]$ and for the five different abundance levels.

- ii)* Keep only the lines which, at the given stellar parameters, have large enough EWs to be visible above the noise. Mathematically, the condition to satisfy is the following:

$$\text{EW}(\text{m}\text{\AA}) > \frac{\sqrt{2\pi}\sigma_{res}}{SNR} \cdot 1000$$

where $\sigma_{res} = 0.56\text{\AA}$ is the standard deviation of the RAVE Gaussian line profile. In practice, any absorption line whose intensity is larger than 1σ of the noise fulfills this condition.

- iii)* Fit the strong Ca II and H I lines and correct the continuum (see Sect. 5.3).

- iv)* Construct the Curve of Growth (COG) of the lines by fitting a polynomial function through the five EW-abundance points.

- v)* Create the model by assuming a Voigt profile for each line and summing these profiles together (see Sect. 5.2).

- vi)* Vary the chemical elemental abundances to obtain different models by changing the EWs of the lines according to their COG.

- vii)* Finally, minimise the χ^2 between the models and

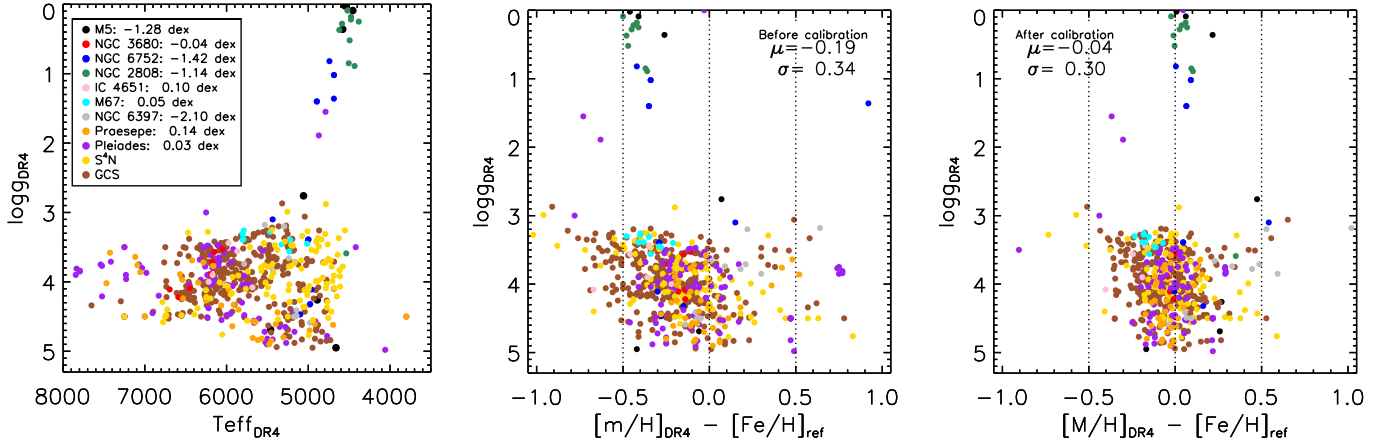


FIG. 12.— Post-calibration verification data sets of open and globular cluster stars, the Geneva-Copenhagen Survey, and the S^4N library. The plot on the right shows that the offsets are greatly improved once the $\log g$ -dependent corrections in metallicity have been applied. The mean offsets (μ) and dispersions (σ) of the residuals are noted in the upper corner of each plot.

TABLE 5
ESTIMATION OF THE EXTERNAL UNCERTAINTIES

Dwarfs				
Parameter range	N	$\sigma(T_{\text{eff}})$	$\sigma(\log g)$	$\sigma([M/H])$
$T_{\text{eff}} > 6000$, $[M/H] < -0.5$	28	314	0.466	0.269
$T_{\text{eff}} > 6000$, $[M/H] \geq -0.5$	104	173	0.276	0.119
$T_{\text{eff}} \leq 6000$, $[M/H] < -0.5$	97	253	0.470	0.197
$T_{\text{eff}} \leq 6000$, $[M/H] \geq -0.5$	138	145	0.384	0.111
Giants				
Parameter range	N	$\sigma(T_{\text{eff}})$	$\sigma(\log g)$	$\sigma([M/H])$
$T_{\text{eff}} > 6000$	8	263	0.423	0.300
$T_{\text{eff}} \leq 6000$, $[M/H] < -0.5$	273	191	0.725	0.217
$T_{\text{eff}} \leq 6000$, $[M/H] \geq -0.5$	136	89	0.605	0.144

the observed spectrum to find the best-matching model.

Further details on the line list and the way the EW library has been constructed can be found in B11. In the following subsections we describe the changes that have been brought to B11. These concern a better consideration of the opacity of neighbouring lines, an implementation of a pseudo-Voigt profile to model the lines and an improved continuum re-normalisation.

5.1. Equivalent-width corrections for the opacity of the neighbouring lines

The EW library is built using the driver *ewfind* of the spectrum synthesis code MOOG (Snedden 1973) which computes the EW of every line as if they were isolated. Nevertheless, line blends when not carefully taken into account can lead to abundance over-estimations. In the case of lines instrumentally (but not physically) blended, the observed blend has a total EW that is the sum of the EWs of the two isolated lines, and thus no problem arises. However, when two lines are physically blended (*i.e.* not instrumentally), the quantity of radiation absorbed by one line is affected by the opacity of the neighbouring line, and the total EW of the blend is smaller than the

sum of the two isolated EWs. In this case the blend in the constructed model is too strong, leading to abundance overestimations. In order to avoid such overestimation, we corrected the EWs of the blended lines in the EW library with the following procedure:

1. Consider the line l_0 having EW_0 , blended with some lines l_i with EW_i . Compute the ratio $EW_r = EW_0 / \sum EW_i$ with EW_0 and EW_i computed as if they were isolated
2. Synthesise the blend composed by l_0 and all l_i , and measure the overall EW_{tot}
3. Compute the corrected EW of the line l_0 as $EW_0^{corr} = EW_r \cdot EW_{tot}$.

Two lines are considered blended if they are closer than 0.2 Å. In addition, we applied this correction to lines which are blended with one or more lines having $EW > 10\text{mÅ}$. Lines with EWs smaller than 10mÅ would affect the EW of the neighbouring lines by less than 0.7%, which can be considered negligible. Although EW_0^{corr} is only an approximation, the constructed blends with such corrected EWs match the synthesised blend better than 1% of the normalised flux. This correction replaces the previous one adopted in the B11 chemical pipeline.

5.2. Improved line profile

Most of the absorption lines in the RAVE wavelength range and resolution have an intrinsic width smaller than the RAVE instrumental profile. Therefore, their line profile is dominated by the instrumental one which is Gaussian. Nevertheless, this is not the case for the strongest lines, where the broad wings extend beyond the instrumental profile. In that case, the line is better approximated by a Voigt profile.

Compared to B11, the new chemical pipeline drops the simplistic Gaussian assumption and now uses an improved line profile. Because of the difficulties of implementing a real Voigt profile we use the approximation implemented by Bruce et al. (2000):

$$V(x) = EW \cdot [rL(x) + (1-r)G(x)] \quad (8)$$

where L and G are the Lorentzian and Gaussian functions, respectively, and EW is expressed in Å. The r parameter rules the linear combination between L and G , so that when $r = 0$, $V(x)$ is a pure Gaussian and when $r = 1$, $V(x)$ is a pure Lorentzian. The Full Width Half Maximum (FWHM) of L and G is forced to be identical, and varies as a function of the EW with the following relation:

$$FWHM = FWHM_{best} + EW/4 \quad (9)$$

where $FWHM_{best}$ is the best matching FWHM found by the minimisation routine during the best matching model searching. Unlike Bruce et al. (2000), we make the parameter r dependent from the EW:

$$r = 0.5 \cdot \exp\left(\frac{-1}{(3EW)^2 + 0.001}\right) \quad (10)$$

so that, for small EW the line profile is Gaussian, and for large EW the line profile approximates a Voigt profile.

Kielkopf (1973) showed that the difference between the real and the pseudo-Voigt profile described by Eq. 8 is always smaller than 1.2% for $EW = 0.5\text{Å}$, which corresponds to an error smaller than 0.72% in EW (Bruce et al. 2000).

5.3. Improved continuum re-normalisation

In order to remove some fringing effects that sometimes affect the initial input RAVE spectra (the same ones as used by the DR4 pipeline, see Sect. 3.6), the chemical pipeline has its own internal re-normalisation algorithm. It can be summarised as follows (a more detailed discussion can be found in Sec. 2.5 and Fig. 3 of B11):

- i)* A preliminary metallicity estimation is performed and the modelled metallic lines are subtracted from the observed spectrum.
- ii)* The strong lines belonging to the Ca II and H I are fitted with a Lorentzian profile and subtracted from the observation.
- iii)* The continuum profile is then defined by a box-car smoothing of the residuals obtained after the previous two steps.
- iv)* The strong Ca II and H I lines are added to the continuum profile to obtain the new "continuum". The chemical pipeline does not measure the broad lines of the Ca II and H I, and their profiles are considered part of the continuum level. Therefore, by adding them to the classical continuum, they are excluded from the chemical analysis. It is by comparison with this level of "continuum" that the metallic lines are measured.

This re-normalisation permits better continuum placement around the absorption lines for a better elemental abundance estimation. In particular, the new adopted Voigt profile (see Sect. 5.2) contributes to improve the continuum placement thanks to the superior fit of the line's wings, which can now be properly subtracted during the re-normalisation procedure.

The present chemical pipeline applies the continuum placement like the chemical pipeline outlined in B11 (see

their Sect. 2.5), with the difference that it is applied twice for spectra with $SNR \geq 40 \text{ pixel}^{-1}$ and only once for $SNR < 40 \text{ pixel}^{-1}$. Indeed, thanks to the pseudo-Voigt profile, the continuum placement process becomes more stable at $SNR \geq 40 \text{ pixel}^{-1}$, and when applied iteratively the continuum estimation converges after 2 iterations. On the other hand, for $SNR < 40 \text{ pixel}^{-1}$ the continuum estimation cannot converge to the right level. The noise spikes (mistaken as metallic lines by the code) lead to a too high continuum placement and, consequently, to a too high metallicity estimation. Thus, the re-normalisation is applied only once for low SNR spectra.

5.4. Precision and accuracy of the RAVE chemical elemental abundances

In order to evaluate the precision and accuracy of the new chemical pipeline, we ran tests on synthetic and real spectra with known chemical abundances and compared the results with the expected abundances. The samples of synthetic and real spectra used are the same as those employed in B11. This allows us to have a clear view of the achieved improvement between the two pipelines.

Unlike the work presented in B11, we present here the tests and results for only 6 elements (aluminium, magnesium, silicon, titanium, nickel and iron). We rejected the calcium abundance as not being reliable (see Sect. 6.3.1).

5.4.1. Internal errors: tests on synthetic spectra

The tests have been performed on a sample of 1353 synthetic spectra. The values for the effective temperature and the surface gravity for these spectra have been taken from a mock sample of RAVE observations created using the Besançon model, whereas the adopted chemical abundances have been taken from the Soubiran & Girard (2005) catalogue whose star metallicities span from -1.5 dex to $+0.4$ dex (for further details on how the sample has been constructed, see B11). This ensures plausible stellar parameters and chemical abundance distributions of the synthetic spectra.

We evaluated the precision and accuracy of the results at $SNR=100, 40, 20 \text{ pixel}^{-1}$. In Fig. 13 and 14 we report the detailed results.

Results at $SNR=100 \text{ pixel}^{-1}$ — While the B11 chemical pipeline gave slightly underestimated abundances, the present one reduces or removes such underestimation for most of the elements at $SNR=100 \text{ pixel}^{-1}$. $[\text{Ni}/\text{H}]$ is under-estimated by ~ 0.1 dex whereas the $[\text{Ti}/\text{H}]$ estimate is good for giants but should be rejected for dwarfs (for which Ti lines are too weak for a good estimation).

Results at $SNR=40 \text{ pixel}^{-1}$ — All the elements have reliable abundances, except for $[\text{Si}/\text{H}]$ and $[\text{Ti}/\text{H}]$, which look overestimated by $\sim +0.1$, and $\sim +0.2$ dex, respectively.

Results at $SNR=20 \text{ pixel}^{-1}$ — $[\text{Fe}/\text{H}]$, $[\text{Si}/\text{H}]$ and $[\text{Al}/\text{H}]$ are reliable, with uncertainties of $\sim 0.15 - 0.20$ dex. $[\text{Mg}/\text{H}]$ and $[\text{Ti}/\text{H}]$ show significant systematics, and $[\text{Ni}/\text{H}]$ cannot be measured because its lines are too weak.

For Ni and Ti the selection effect due to the SNR is particularly evident. Moving to lower SNR the number

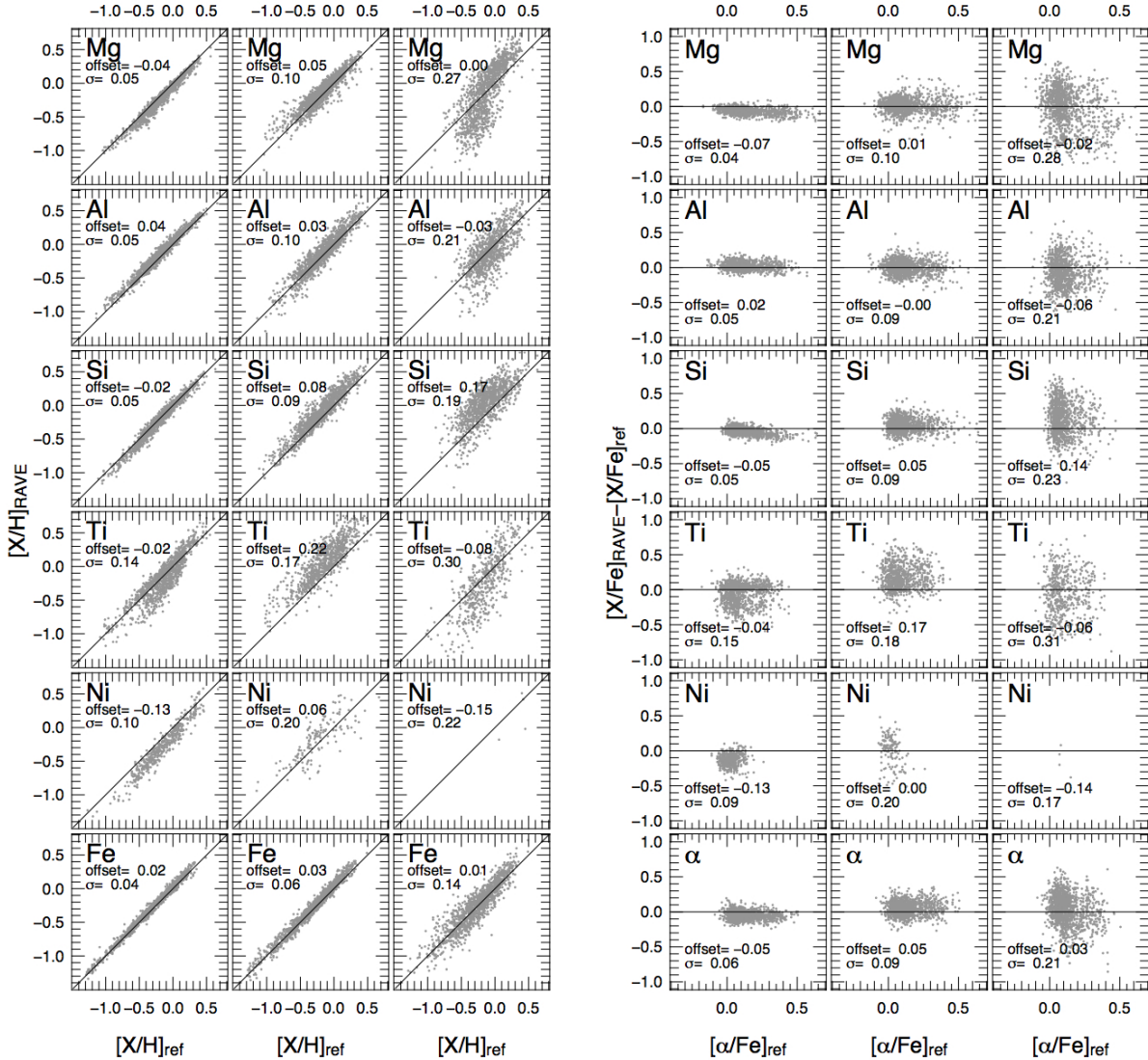


FIG. 13.— **Left:** expected elemental abundances $[X/H]$ (x-axis) versus measured elemental abundances (y-axis) for the sample of synthetic spectra at $\text{SNR}=100, 40, 20 \text{ pixel}^{-1}$ (for the left, middle and right column, respectively) and assuming no errors in stellar parameters. **Right:** as in left panels but for the expected enhancement $[X/Fe]$ (x-axis) and the residuals measured-minus-expected (y-axis). Offsets and standard deviations are reported in the panels. α -abundances are computed as in B11, *i.e.* the mean of Mg and Si abundances.

of spectra with Ti and Ni estimations decreases, because the lines of Ti (in dwarf stars) and Ni are weak in the RAVE wavelength range and they do not overcome the noise at low SNR. This selection bias is further discussed in Sec. 6.3.1.

In general, the new chemical pipeline suffers smaller systematics with respect to the old one. Underestimations are reduced and abundances of important elements (Fe, Si, Al and Mg) do not correlate with the effective temperature (see Fig. 15) as they did with the previous pipeline. $[\text{Ti}/\text{H}]$ appears reliable only for cool giants.

We further tested the robustness of our results by repeating the abundance measurements after adjusting randomly the initial T_{eff} , $\log g$ and $[\text{M}/\text{H}]$ by values normally distributed around their true values with $\sigma_{T_{\text{eff}}} = 250 \text{ K}$, $\sigma_{\log g} = 0.5 \text{ dex}$ and $\sigma_{[\text{M}/\text{H}]} = 0.2 \text{ dex}$, re-

spectively. The results are shown in Fig. 14. The shifts in stellar parameters (representing the input errors) simply inflate the errors in abundances seen in the test without stellar parameters errors, without introducing any new systematics.

5.4.2. External errors: tests on real spectra

The overall uncertainties have been estimated by computing the elemental abundances of 98 RAVE spectra of dwarf stars from Soubiran & Girard (2005, hereafter SG05) and 233 RAVE spectra of 203 giant stars from Ruchti et al. (2011, hereafter R11). Most of the SG05 stars have RAVE spectra with $\text{SNR} > 100 \text{ pixel}^{-1}$ whereas the R11 stars have RAVE spectra with SNR ranging between 30 pixel^{-1} and 90 pixel^{-1} . Hence the results are representative of the medium-high SNR regime. Figure 16 and Fig. 17 show the results obtained for the

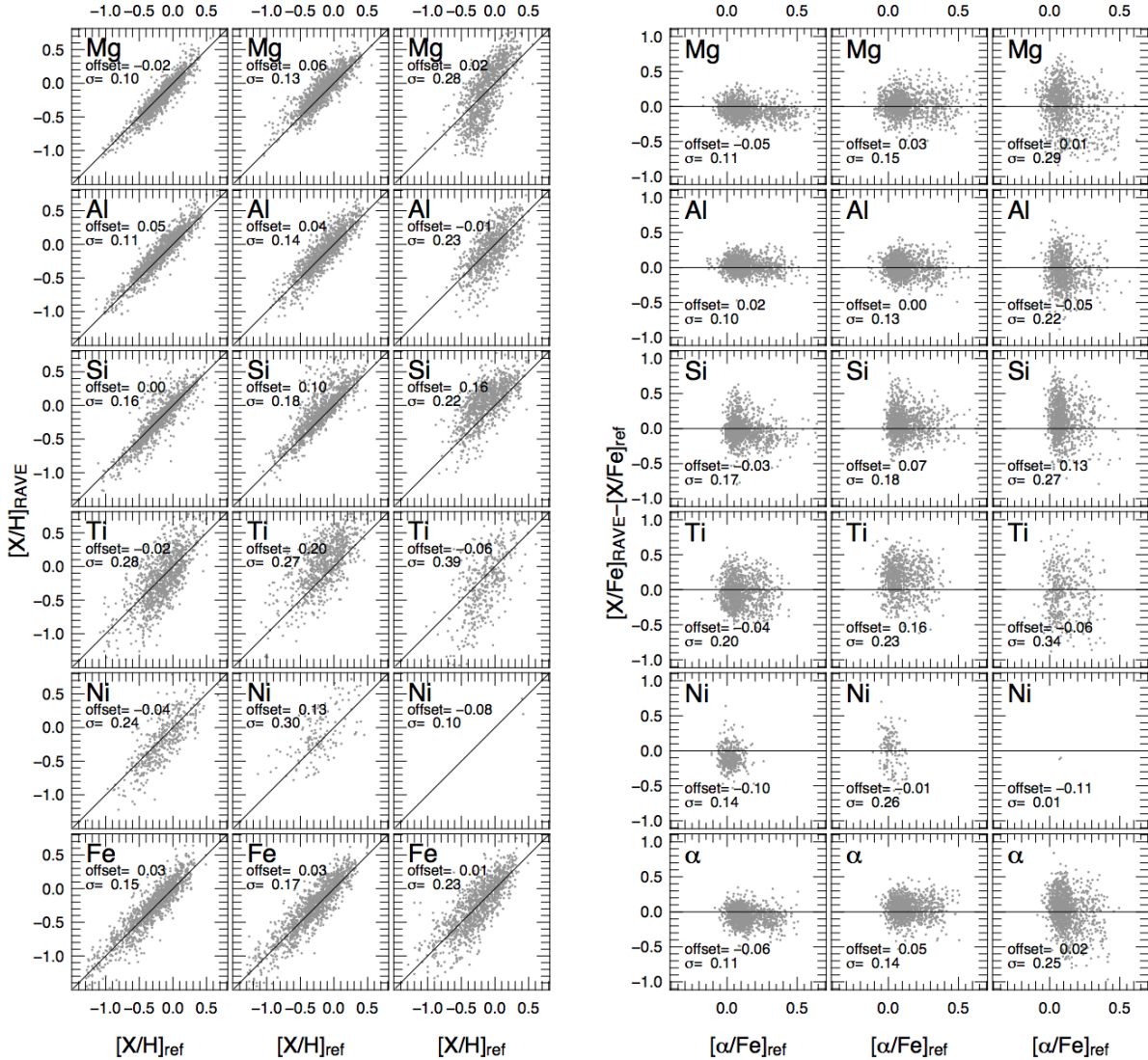


FIG. 14.— As in Fig. 13 but with noisy stellar parameters to simulate the errors appropriate for the RAVE pipeline.

six elements in common with SG05 and the four in common with R11.

Adopting the RAVE DR4 stellar parameters, the RAVE chemical pipeline delivers slightly underestimated abundances for Mg, Al and Ti (~ -0.1 dex). There is a general improvement in precision for most of the elements with respect to the B11 pipeline (dispersions smaller than ~ 0.05 - 0.07 dex for Mg, Ti, Fe) with no visible systematic offsets. The estimated errors in abundance depend on the element and range from 0.17 dex for Mg, Al and Ti to 0.3 dex for Ti and Ni. The error for Fe is estimated as 0.23 dex. We note that the errors reported here are conservative estimations of the RAVE abundance errors, because we are comparing our results with other more precise, but still uncertain measurements, and we have not corrected the variance for the second contribution. For illustration, assuming an uncertainty in the reference abundances of 0.1dex, our estimated RAVE errors decrease by 0.03-0.05 dex.

6. FOURTH PUBLIC DATA RELEASE: CATALOGUE PRESENTATION

The fourth public data release of the RAVE data (RAVE DR4) includes the observations obtained from the 3rd of April 2004 to the 20th of December 2012. In total, 425 561 stars have been observed, collecting 482 430 spectra. The catalogue is accessible online, and it contains also radial velocities, proper motions, photometric information, stellar morphological flags (coming from Matijević et al. 2012), line-of-sight distances, ages and interstellar extinction for each star. In addition, the parameters obtained with the previous DR3 pipeline are also published, to assist readers of papers published based on those parameters, though we strongly recommend the use of the parameters obtained with the latest DR4 pipeline in all future analyses. The DR4 catalogue can be queried or retrieved from the VizieR database at the *Centre de Données Astronomiques de Strasbourg* (CDS), as well as from the RAVE collaboration Web site

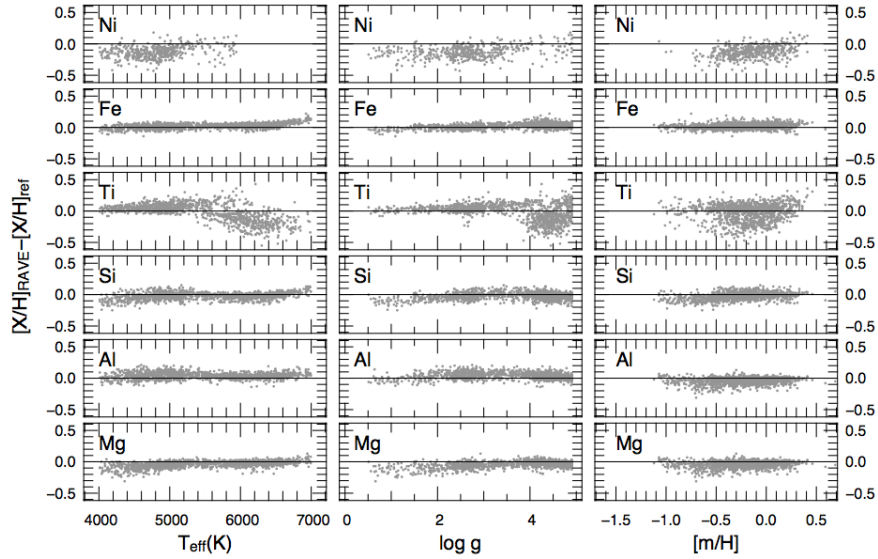


FIG. 15.— Correlation between the elemental abundance residuals and the stellar parameters at $\text{SNR}=100 \text{ pixel}^{-1}$.

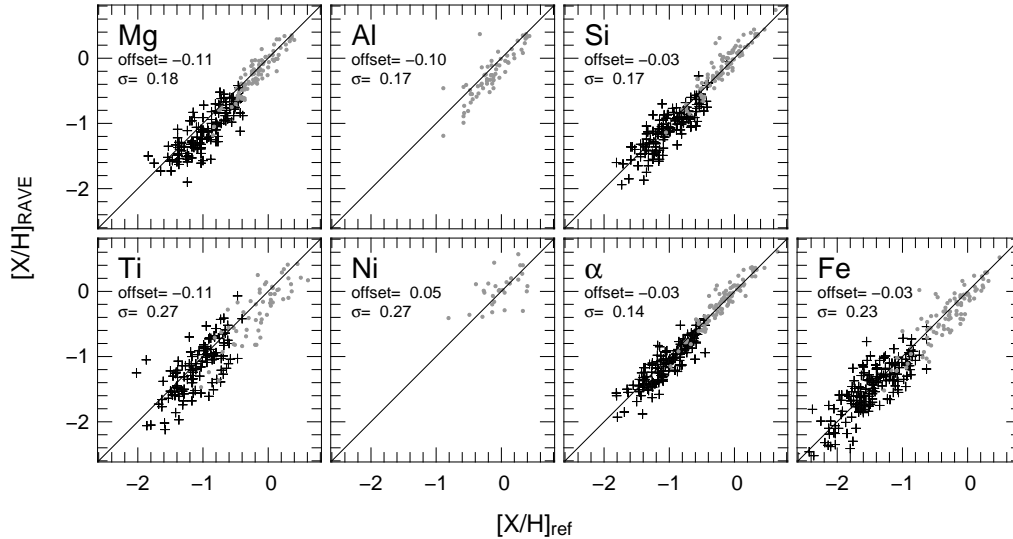


FIG. 16.— Comparison between the reference high-resolution elemental abundances (x -axis) and RAVE elemental abundances (y -axis) for the SG05 (98 dwarf stars, gray dots) and the R11 samples (233 spectra of 203 giant stars, black “+”) measured by adopting the stellar parameters provided by the RAVE pipeline.

(www.rave-survey.org).

The completeness of the published catalogue for the radial velocities, atmospheric parameters, distances and chemical abundances, with respect to the $I_{2\text{MASS}}$ catalogue can be seen in Fig. 18. In addition, Aitoff maps for the completeness of the catalogue at four different magnitude bins as a function of the stellar positions on the sky are shown in Fig. 3.

Below we discuss which criteria to apply in order to obtain a high quality and reliable sample of stars from the catalogue of the atmospheric parameters and the elemental abundances. Brief discussions about proper motions, radial velocities, distances as well as the new

APASS photometry are also included in what follows, but we refer the reader to Siebert et al. (2011b), Zwitter et al. (2010), Binney et al. (2013) and Munari et al. (2013a,b) for full details.

6.1. Criteria for reliable sub-sample selection considering the atmospheric parameters

The following criteria need to be understood as the confidence limits for selection based on observational (signal-to-noise ratio) and pipeline limitations (mainly the boundaries of the grid).

We selected all the stars which had a $\text{SNR} > 20 \text{ pixel}^{-1}$,

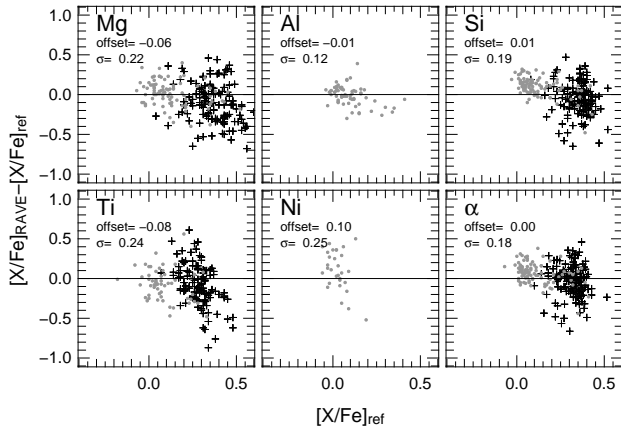


FIG. 17.— Comparison between expected relative elemental abundance (x -axis) and residual abundances RAVE-minus-reference (y -axis). Stellar parameters adopted and symbols are as in Fig. 16.

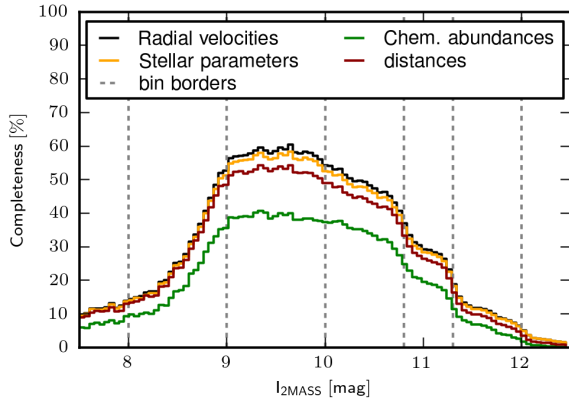


FIG. 18.— Fractional completeness of the RAVE DR4 sample with respect to the I_{2MASS} stars for the published radial velocities, stellar atmospheric parameters, chemical abundances and line-of-sight distances.

had errors in the radial velocity estimation of less than 8 km s^{-1} (measured by RAVE DR3, see Sect. 8), had derived $\log g > 0.5$ dex, determined $T_{\text{eff}} > 3800 \text{ K}$ and calibrated metallicity $[M/H] > -5$ dex (measured by the DR4 pipeline), and for which the DR4 algorithm had converged towards a stable solution¹⁰. In total, roughly 19% ($\sim 8.7 \times 10^4$) of the spectra have been rejected after these quality criteria. We are working towards the next DR5 RAVE data release, with work which we hope will improve the parameters for at least some of these currently non-reliable stars.

The cut on the error on the radial velocity ($\Delta V_{\text{HRV}} < 8 \text{ km s}^{-1}$, 12 974 spectra) has been defined based on the results of Kordopatis et al. (2011a), where it has been shown that for Doppler shifts larger than approximately half a pixel, the results of the pipeline were seriously

¹⁰ MATISSE iterates up to 10 times until the result of the projection of the spectrum on the projection functions $B_{\theta}(\lambda)$ is within the parameter range defined by the $B_{\theta}(\lambda)$ (see Recio-Blanco et al. 2006; Kordopatis et al. 2011a, and Sect. 3.3)

degraded. Nevertheless, a criterion based on the Tonry-Davis correlation coefficient (R) might be preferred in some cases, since some stars can have large errors but good R (due, for example, to strong hydrogen lines), and vice-versa (small errors but $R < 5$).

The removal of the stars with gravities lower or equal to 0.5 dex (25 882 spectra), T_{eff} lower than 3800 K (20 143 spectra) and/or calibrated $[M/H]$ lower than -5 dex (1 282 spectra) has been decided because the results are considered both unrealistic (the synthetic spectra computed with the MARCS atmospheric models at such $\log g$ have not been carefully compared to real spectra) and less reliable (e.g.: missing models in the reference grid). Finally, the cut on the convergence of the DR4 algorithm (14 454 spectra) is made in order to minimise cases badly affected by the spectral degeneracies. Indeed, these degeneracies can cause, in some cases, an impossibility for the algorithm to converge due to a negative gradient in the distance function between the spectrum and the templates. MATISSE can in some cases oscillate between two solutions ($\sim 11\%$ of the published sample). We decided to keep these solutions because, in general, they are close in the parameter space. Nevertheless, in case the user decides not to use them, we have flagged these stars in the *algo_conv* parameter which is also published with this data release (see the appendix).

An additional cut, based on the velocity width parameter of the spectral lines, V_{rot} , has been applied, since our algorithm cannot treat fast rotators. We discarded empirically stars at the high velocity tail of the distribution ($V_{\text{rot}} > 100 \text{ km s}^{-1}$, 11 735 in total). We recall that the estimation of the V_{rot} is made through the DR3 pipeline, as a free parameter, at the same moment as the first estimation of T_{eff} , $\log g$ and $[M/H]$ is made. Nevertheless, the rather low resolving power of RAVE spectra ($\sim 1.2 \text{ \AA}$ or 30 km s^{-1}) does not allow the determination of rotational velocities for slow rotators which represent the vast majority of RAVE stars. Hence this parameter is not published, but true fast rotators will be discussed in a separate paper.

Finally, we note that targets at low Galactic latitudes should also be treated with caution, since the possibly high interstellar extinctions in these directions are not taken into account in the photometric constraints imposed by the DR4 pipeline.

6.2. Criteria for reliable sub-sample selection considering the chemical abundances

From the whole RAVE internal data set, we measured chemical abundances only for spectra with the following features:

- Effective temperature $4000 \leq T_{\text{eff}}(\text{K}) \leq 7000 \text{ K}$
- Signal-to-noise $\text{SNR} > 20 \text{ pixel}^{-1}$
- Rotational velocity $V_{\text{rot}} < 50 \text{ km s}^{-1}$.

Such limitations are due to the following facts. First, the EW library (and the B11 line list on which it is based) is reliable only in this effective temperature range. In addition, the line measurement and stellar parameters are reliable only for signal-to-noise larger than 20 pixel^{-1} . Finally, the absorption lines can be reliably measured

only if their FWHM does not significantly exceed the RAVE instrumental FWHM ($\sim 1.2\text{\AA}$) which corresponds to a rotational velocity of 30 km s^{-1} . Such criteria leave 313,874 spectra selected from the RAVE database.

Besides the chemical abundances of this selected sample, we provide some extra statistical quantities and flags to be employed for further quality selection:

1. χ^2 *between best matching model and observed spectrum*: the lower the values the better the expected abundance precision. We suggest a user reject spectra with $\chi^2 > 2000$.
2. *the value frac* which represents the fraction of the observed spectrum which satisfactorily matches the model. We suggest a user reject spectra with $frac < 0.7$ (see B11 for further details).
3. *classification flags by Matijević et al. (2012)*: we suggest a user selects spectra classified as “normal” by Matijević et al. in order to avoid peculiar objects on which the chemical pipeline fails.
4. *Algo_Conv value*: this value indicates if the DR4 pipeline has converged or if the stellar parameters were either outside the grid boundaries or MATISSE was oscillating between two values. The higher quality data have *Algo_Conv* = 0.

The application of these quality flags is left to the user. The number of spectra which meet all such quality flags is 187,305. In Fig. 19 we show the distribution of the chemical abundances, given the above mentioned criteria, for $\text{SNR} > 20\text{ pixel}^{-1}$ and $\text{SNR} > 40\text{ pixel}^{-1}$.

6.3. Results and comparisons with DR3

A description of Galactic properties based on the published parameters of this catalogue are beyond the scope of this paper. Nevertheless, as a sanity check, we explore in this section the general properties of the catalogue, by analysing the correlation of the parameters and the change of the metallicity properties according to the SNR, the effective temperature or the surface gravity. By comparing the behaviours of the DR3 and the DR4 pipelines, we show that although the differences between the atmospheric parameters of the two methods are relatively subtle, DR4 better reproduces the expected behaviour for different subpopulations of stars and thus is the method of choice for most Galaxy evolution studies.

Figure 20 compares the resulting $T_{\text{eff}}-\log g$ diagrams of the DR4 and the DR3 pipelines as selected according to the criteria of Sect. 6.1. One can notice that besides the well understood and described discretisation due to the DEGAS algorithm, there are some additional subtle differences in the parameters of the two pipelines. In particular, hot dwarfs, as well as turn-off stars have now smaller surface gravities and the main-sequence is better defined. Finally, giants have slightly higher effective temperatures.

The DR4 and DR3¹¹ calibrated metallicity trends, as a function of the surface gravity and the effective temperatures can be seen in Fig. 21. As far as the T_{eff} de-

pendencies are concerned, one can notice that the metallicity distribution functions (MDFs) of the DR4 pipeline get broader when the effective temperature lowers. In particular, the DR4 pipeline finds that the hottest stars have a narrow metallicity distribution with a mean value at slightly super-solar values, as expected for the young stars in the solar neighbourhood. This is not the case for the results of the DR3 pipeline, where metallicities as low as $[M/H] \sim -0.5$ dex are obtained. Furthermore, from the iso-contours of the $\log g$ vs $[M/H]$, we can see that despite the mild pixelisation of the values, there are no trends of the metallicities as a function of the surface gravity for the dwarfs, as derived by the DR4 pipeline. This is not the case for the DR3 pipeline results, where a shift is noticed.

In order to investigate whether this shift is real and justified given our classical view of the Milky Way, we explored the stellar heliocentric radial velocities and the evolution of the MDFs for different surface gravity bins. Figure 22 shows the resulting histograms for the calibrated metallicities of the DR4 (in black solid lines) and the DR3 pipelines (red dashed lines). The radial velocity dispersions of the selected stars have also been reported inside each box. For the lower panels, corresponding to the dwarf stars ($3.5 < \log g < 5$ dex), the radial velocity dispersion stays constant. Considering that each Galactic population (thin disc, thick disc and halo) is characterised by a different velocity dispersion, the constant $\sigma_{V_{\text{HRV}}}$ that is found indicates that the same proportions of Galactic populations are probed for these gravity bins. As a result, the MDFs should not vary inside these bins. This is the case only for the DR4 MDFs, the DR3 ones shifting by 0.2 dex in this range of $\log g$. As far as the sub-giant and giant stars are concerned, a good agreement is found between the DR3 and DR4 MDFs, with a shift towards lower metallicities with decreasing $\log g$ and at the same time an increase in the radial velocity dispersion. This is in agreement with a change in the mixture of the probed Galactic populations as a function of the probed volume, passing from an old thin disc dominated population to the presence of more halo stars for the larger volume probed by the more luminous giant stars.

To show the correlations between the parameters, we select among the DR4 catalogue those stars that are observed multiple times, and for which several independent spectra and derived parameter sets are available. In the panels we plot the differences between the several determinations of the measured T_{eff} , $\log g$ and calibrated metallicities. Figure 23 shows the results for the stars with $\text{SNR} > 20\text{ pixel}^{-1}$, for both DR4 and DR3 pipelines. From that figure one can see that the new DR4 pipeline is more robust than the DR3 one, since the bulk of the stellar parameters show a very small discrepancy between the repeated observations, as well as a negligible parameter correlation. This validates once more the robustness of our calibration relation of Eq. 7. However, we note that correlations between the parameter estimations still exist for some stars. This is expected, due to the intrinsic spectral degeneracy: an underestimation of the T_{eff} leads to a similar underestimation of the $\log g$ and the $[M/H]$.

The robustness of the DR4 pipeline in terms of better treatment of the spectral degeneracies can also be seen on Fig. 24. The evolution of the mean metallicity as a

¹¹ Calibrated according to Eq. 2 of Siebert et al. (2011b), with $c_0 = 0.578, c_1 = 1.095, c_3 = 1.246, c_4 = -0.520$.

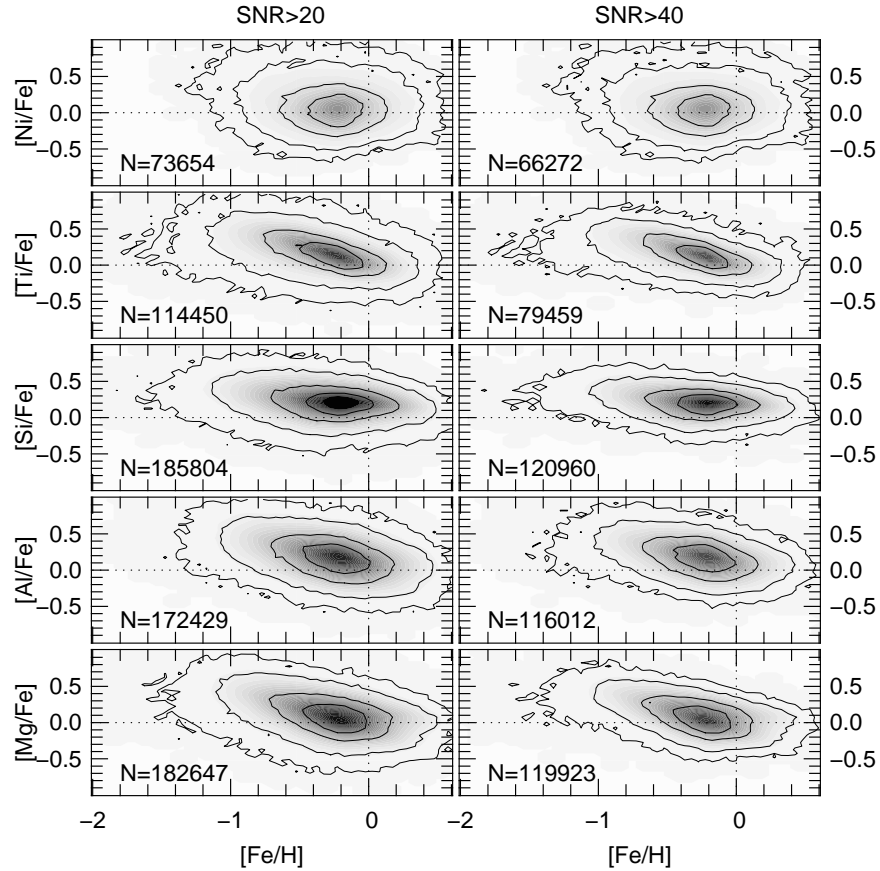


FIG. 19.— Distribution on the chemical plane of spectra after the application of the quality indicators reported in Sec. 6.2. The isocontours hold 34.0%, 68.0%, 95.0% and 99.5% of the sample.

function of the SNR (yellow points on Fig. 24) shows no trends down to $\text{SNR} > 15 \text{ pixel}^{-1}$. Nevertheless, the cost for this better treatment is the pixelation of the results for the most metal-poor stars or the ones having low SNR. In particular, the pixelisation effect can be clearly seen in Fig. 24 below the threshold of $\text{SNR} = 30 \text{ pixel}^{-1}$. Indeed, we recall that for all the observed spectra DE-GAS is first used to find the nominal template spectrum of the learning grid in order to re-normalise the observed one. Then, on one hand, for the high SNR regime, the MATISSE algorithm is used on these optimally re-normalised spectra in order to obtain the final parameters. On the other hand, for the low SNR data ($< 30 \text{ pixel}^{-1}$) and at the boundaries of the learning grid, tests on synthetic spectra have shown that the projection method was giving less accurate results than the decision-tree. Given these facts, Kordopatis et al. (2011a) showed that DE-GAS is preferred over the projection approach of MATISSE for $\text{SNR} < 30 \text{ pixel}^{-1}$, even if a pixelisation of the parameters is introduced.

6.3.1. Chemical abundance reliability: element by element

Besides the quality indicators described in Sect. 6.2, the number of measured absorption lines for an element can be a good indicator of the reliability and precision of the abundance estimation (as illustrated in Fig. 25). We outline here a summary of the expected precision of

the abundance element by element.

Magnesium yields reliable results on synthetic and real spectra with no significant correlation with stellar parameters. We expect errors $\sigma_{\text{Mg}} \leq 0.15 \text{ dex}$ for $\text{SNR} > 40 \text{ pixel}^{-1}$ and $\sigma_{\text{Mg}} \sim 0.25 \text{ dex}$ for $20 < \text{SNR} < 40 \text{ pixel}^{-1}$. Tests on synthetic spectra show that Magnesium suffers of a systematic error when measured at low SNR. Such an error has not been confirmed with real spectra.

Aluminium gives a reliable abundance although obtained with only two isolated lines. Abundance errors expected are $\sigma_{\text{Al}} \leq 0.15 \text{ dex}$ for $\text{SNR} > 40 \text{ pixel}^{-1}$ and $\sigma_{\text{Al}} \sim 0.25 \text{ dex}$ for $20 < \text{SNR} < 40 \text{ pixel}^{-1}$.

Silicon is among the most reliably determined elements. Abundance errors expected are $\sigma_{\text{Si}} \leq 0.15 \text{ dex}$ for $\text{SNR} > 40 \text{ pixel}^{-1}$ and $\sigma_{\text{Si}} \sim 0.25 \text{ dex}$ for $20 < \text{SNR} < 40 \text{ pixel}^{-1}$ with a small overestimation of $\sim 0.1 \text{ dex}$.

Titanium gives reliable estimates at high SNR for cool giants ($T_{\text{eff}} < 5500 \text{ K}$ and $\log g < 3$). We suggest rejecting Ti abundances for dwarf stars. Tests on synthetic and real spectra suggest an expected error of

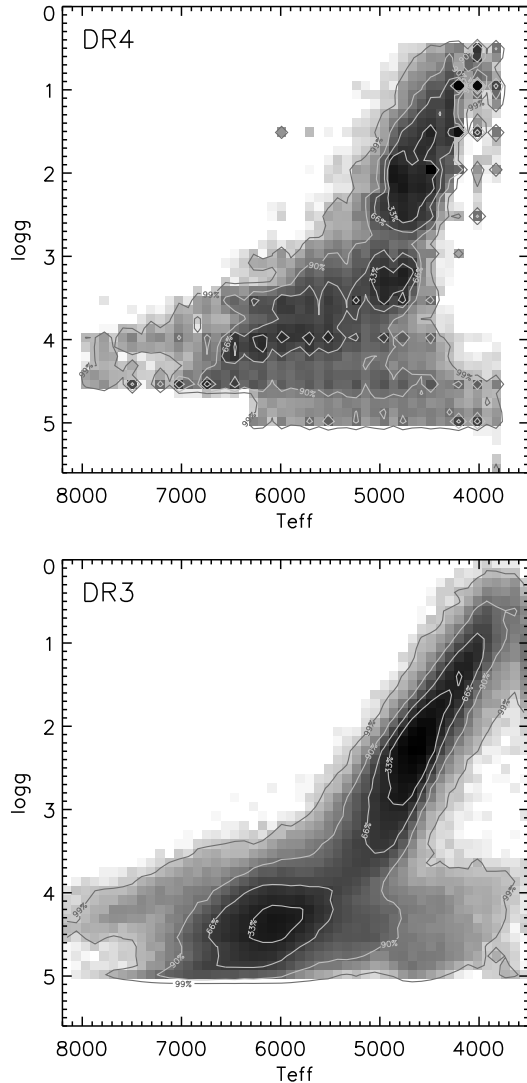


FIG. 20.— $T_{\text{eff}}\text{-log } g$ diagram for the selected RAVE stars (top: DR4 pipeline, bottom: DR3 pipeline), meeting our criteria defined in Sect. 6.1. In total the parameters of $\sim 4 \times 10^5$ spectra are represented in these diagrams. The contour lines contain 33%, 66%, 90% and 99% of the total considered sample.

$\sigma_{\text{Ti}} \leq 0.2$ dex for $\text{SNR} > 40 \text{ pixel}^{-1}$ and $\sigma_{\text{Ti}} \sim 0.3$ dex for $20 < \text{SNR} < 40 \text{ pixel}^{-1}$.

Iron gives robust and precise abundances thanks to its large number of measurable lines at all stellar parameter values. Expected errors are $\sigma_{\text{Fe}} \leq 0.1$ dex for $\text{SNR} > 40 \text{ pixel}^{-1}$ and $\sigma_{\text{Fe}} \sim 0.2$ dex for $20 < \text{SNR} < 40 \text{ pixel}^{-1}$.

Nickel abundances have to be used with care because of the few lines that are measurable. From synthetic spectra we infer that Ni should be used for cool stars only ($T_{\text{eff}} < 5000\text{K}$) and high SNR. In this regime, the abundances are reliable (despite being underestimated by ~ 0.1 dex) with an expected error of $\sigma_{\text{Ni}} \sim 0.25$ dex. The mean abundance correlates with the number of measured lines (*i.e.* with SNR) as highlighted in Fig. 25.

α -enhancement is the average of $[\text{Mg}/\text{Fe}]$ and $[\text{Si}/\text{Fe}]$ and it proved to be a robust estimation, particularly useful at low SNR, where the measurements are more uncertain. The expected error is ~ 0.15 dex for $\text{SNR} > 40 \text{ pixel}^{-1}$ and ~ 0.2 dex for $20 < \text{SNR} < 40 \text{ pixel}^{-1}$.

Thanks to the improved line profile and the correction of the EW library for the opacity of the neighbouring lines, the continuum re-normalisation has improved. The new abundances are now less affected by systematic errors than the previous ones and their correlations with T_{eff} are now negligible. On the other hand, the new continuum re-normalisation reveals the scarcity of information for elements with weak and few visible lines like $[\text{Ca}/\text{H}]$ (which has been dropped in this data release) and $[\text{Ti}/\text{H}]$ on dwarf stars, which turns out to be not reliable. A slight correlation between abundances and SNR is present, as shown in Fig 26. Such correlation is negligible for giant stars whereas for dwarfs stars $[\text{m}/\text{H}]_{\text{chem}}$ (computed with the formula given by Salaris et al. 1993, see Sect. 3.4 of B11) increases by ~ 0.1 dex from $\text{SNR} = 80 \text{ pixel}^{-1}$ to $\text{SNR} = 40 \text{ pixel}^{-1}$. The different re-normalisation procedure for the two SNR regimes generates the step in average metallicity seen at $\text{SNR} = 40 \text{ pixel}^{-1}$.

The accuracy of the RAVE abundances depends on many variables, often inter-dependent in a non-linear way, which makes difficult the accuracy estimation of the individual abundances. Indeed, on one hand the abundance accuracy depends on the number of measured absorption lines. On the other hand, the number of measurable lines (*i.e.* strong enough to be identified in the noise) depends on SNR and on the stellar parameters. In Fig. 25 the dispersion of the residuals between measured and expected abundances (for the sample of synthetic spectra) decreases as the number of measured lines increases. This number is a useful index of goodness of the abundance accuracy, although it must be considered together with SNR. In Fig. 27 we illustrate the fraction of spectra having an abundance estimation (*i.e.* at least one absorption line measured) for different elements, and how this fraction decreases when SNR and/or metallicity decrease. This is a selection effect due to the measurement process and it must be taken in account during data analysis and interpretation.

6.3.2. Comparison between $[\text{M}/\text{H}]$ and $[\text{m}/\text{H}]_{\text{chem}}$

In order to measure the chemical abundances, the RAVE chemical pipeline uses on one hand the estimation of T_{eff} and $\log g$ of the RAVE pipeline, and on the other hand $[\text{M}/\text{H}]$ is employed only as a first guess. This means that the metallicity $[\text{m}/\text{H}]_{\text{chem}}$ (computed as explained in Sec 3.4 of B11) and any elemental abundance provided by the chemical pipeline are independent of $[\text{M}/\text{H}]$. It is, therefore, interesting to compare $[\text{M}/\text{H}]$ with $[\text{m}/\text{H}]_{\text{chem}}$ as much as with $[\text{Fe}/\text{H}]$, because the latter is the element of reference used to calibrate $[\text{M}/\text{H}]$. In Fig. 28 the residuals between $[\text{M}/\text{H}]$, $[\text{m}/\text{H}]_{\text{chem}}$ and $[\text{Fe}/\text{H}]$ are shown as a function of T_{eff} , $\log g$ and $[\text{M}/\text{H}]$ for spectra with $\text{SNR} > 40 \text{ pixel}^{-1}$. In general, $[\text{M}/\text{H}]$ appears to lie between $[\text{Fe}/\text{H}]$ and $[\text{m}/\text{H}]_{\text{chem}}$, in the order $[\text{Fe}/\text{H}] \leq [\text{M}/\text{H}] \leq [\text{m}/\text{H}]_{\text{chem}}$. More specifically, there

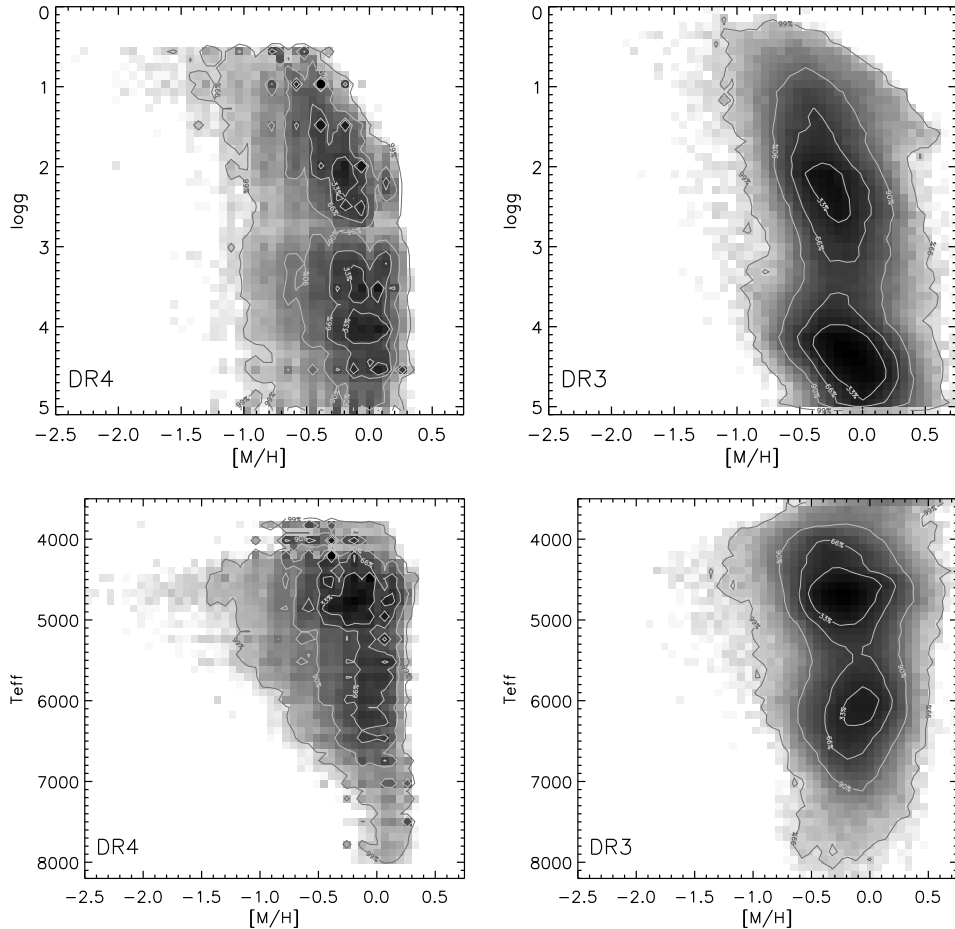


FIG. 21.— Surface gravity ($\log g$, upper plots) and effective temperature (T_{eff} , lower plots) versus metallicity for all the selected RAVE stars, defined in Sect. 6.1. The contour lines contain 33%, 66%, 90% and 99% of the total considered sample. The results for the DR4 pipeline are on the left hand side, whereas the results from the DR3 pipeline are on the right hand side. For both pipelines the mean metallicity slightly decreases for the lowest gravities, which is a signature of a different mixture in the probed Galactic populations. In addition, one can notice the $\log g$ and the T_{eff} trends which are present for the dwarfs analysed with the DR3 pipeline.

are some differences: for dwarf stars this difference is slightly larger (~ 0.1 dex) than for giants (≤ 0.05 dex). This can be due to the higher number of strong and narrow absorption lines available in giants with respect to hot dwarfs, which allows better measurements over the whole SNR range. In addition, the $[\text{Fe}/\text{H}]$ deviation can be due to the α -enhanced stars which do not follow the enhancement relation of the learning grid (see Sec. 3.4) and for which $[\text{Fe}/\text{H}] \neq [\text{M}/\text{H}]$. Indeed, roughly 25% of the stars with $\text{SNR} > 40 \text{ pixel}^{-1}$ deviate more than 1σ (0.15 dex) from the enhancements of the learning grid of Sec. 3.4.

7. PROPER MOTIONS

In DR3, the proper motions were sourced from the PPMX (Röser et al. 2008), Tycho-2 (Høg et al. 2000), SSS (Hambly et al. 2001), and UCAC2 (Zacharias et al. 2004) catalogs. As already described in DR2, the most precise available proper motion was chosen for each object. In DR4, we no longer follow this procedure but publish a set of available proper motions for each object and leave the selection to the user. The reason is the following: the proper motion error bars published are

of different origin, they may be calculated either from the scatter or from the weights of the individual positions. Hence, the proper motion with the smallest formal error is not necessarily the most accurate. So, the DR4 catalogue lists proper motions from the following sources: Tycho-2, UCAC2, UCAC3, UCAC4 (Zacharias et al. 2010, 2013), PPMX, PPMXL (Roeser et al. 2010) and SPM4 (Girard et al. 2011).

8. RADIAL VELOCITIES

The radial velocities for this fourth data release are based on the RAVE pipeline described in Siebert et al. (2011b), therefore only a brief reminder of the general features is given here.

The radial velocities are obtained using a standard cross-correlation algorithm in Fourier space on the continuum subtracted spectra. First, an estimate of the radial velocity is obtained using a subset of 10 template spectra. This first estimate, with an accuracy better than 5 km s^{-1} is used to put the spectrum in the zero velocity frame. A new template is constructed using the full template database using a penalised chi-square technique described in Zwitter et al. (2008). The new template is

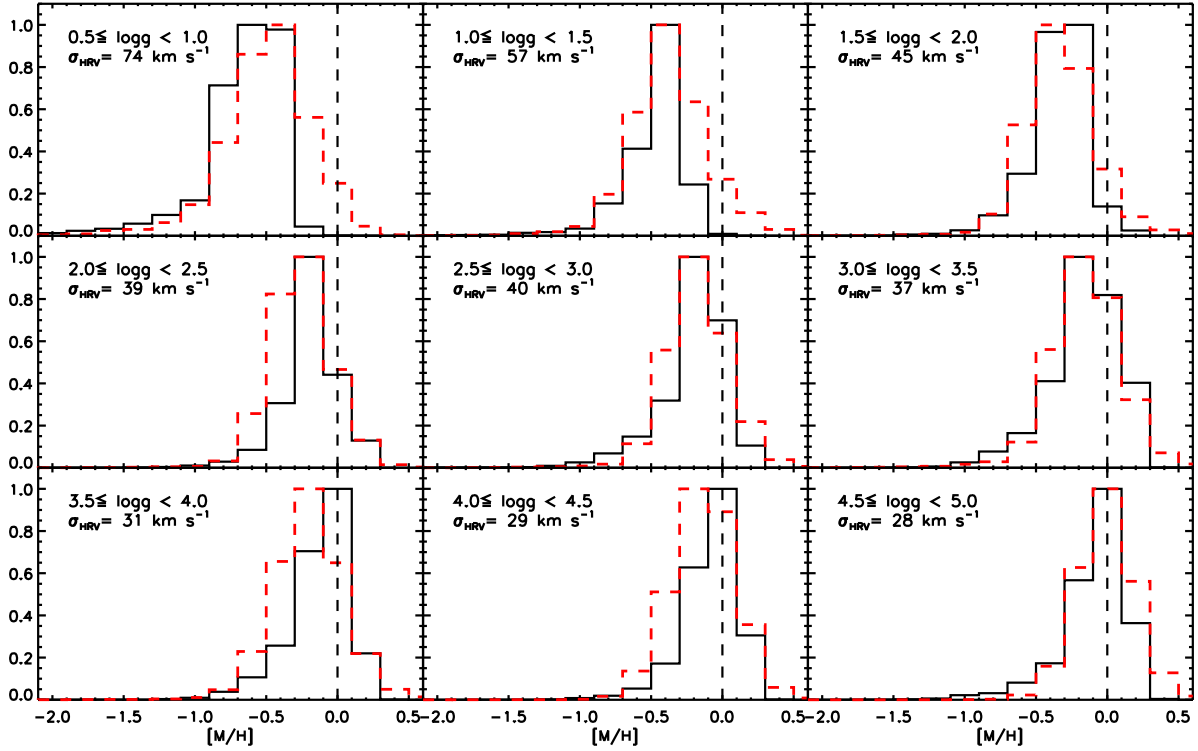


FIG. 22.— Calibrated metallicity distribution functions for different surface gravity ($\log g$) bins. The peak of the histograms have been normalised to unity. The mean radial velocity dispersion for the selected stars per surface gravity bin (σ_{HRV}) are noted in the upper part of each box. RAVE DR4 results are plotted in black solid lines, RAVE DR3 ones in red dotted lines.

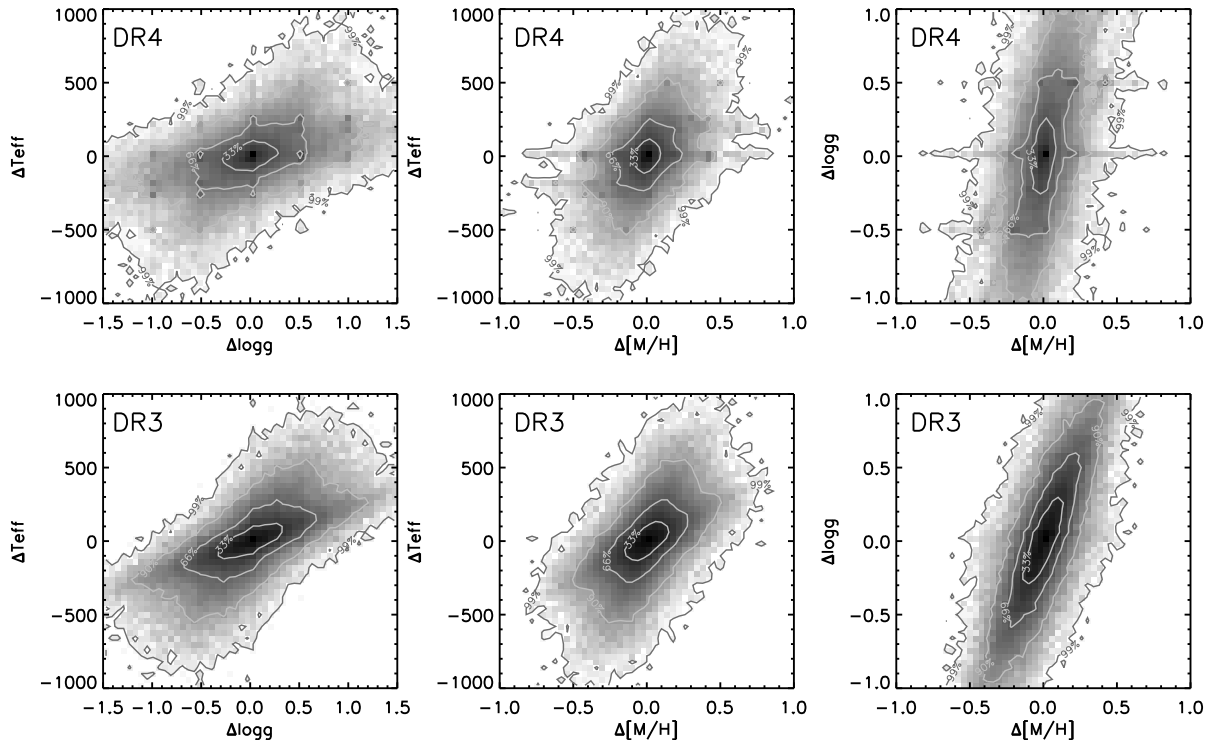


FIG. 23.— Correlations between the derived atmospheric parameters (top: DR4 pipeline, bottom: DR3 pipeline) for the stars that have been observed several times by RAVE. The iso-contour levels contain 33%, 66%, 90% and 99% of the total considered sample. See the text for an explanation.

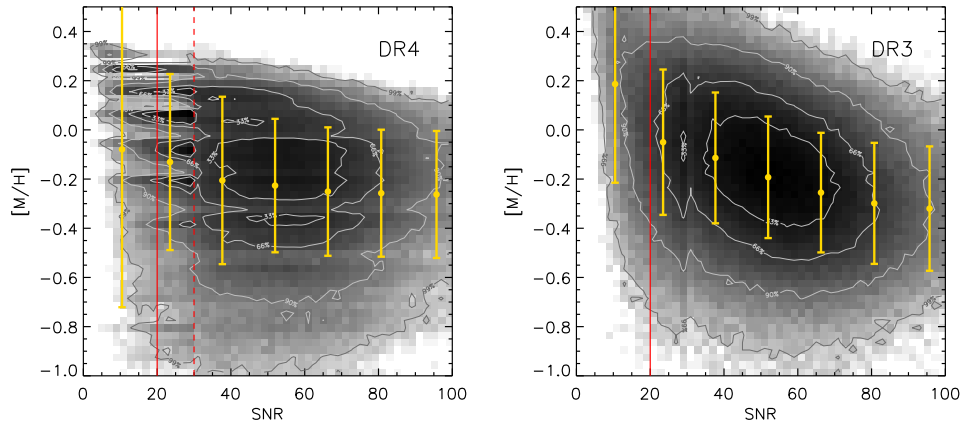


FIG. 24.— Calibrated $[M/H]$ versus SNR for the selected RAVE stars with the DR4 pipeline (left hand side) and the DR3 one (right hand side). One can notice the pixelisation at low SNR ($\text{SNR} < 30 \text{ pixel}^{-1}$, red dashed line), due to the DEGAS algorithm. The yellow points are calculated as the mean measured metallicity in different SNR bins, and the error bars represent the metallicity dispersion inside each bin. One can notice that the DR4 results (left hand side plot) are more stable to SNR changes, compared to the results of the DR3 (right hand side plot). A red solid line is plotted at the $\text{SNR} = 20 \text{ pixel}^{-1}$ value, below which the parameters are not considered reliable.

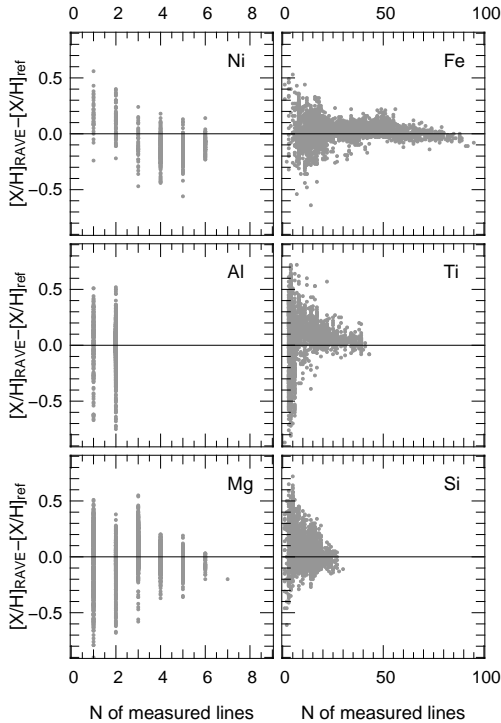


FIG. 25.— Residuals between measured and expected abundances (y-axis) as function of the number of measured lines (x-axis) for each element in the test with synthetic spectra at SNR=100, 40, 20 pixel⁻¹.

then used to derive the final, more precise, radial velocity. The internal error is obtained as the error on the determination of the maximum of the correlation function. This part is performed using the IRAF `xcsao` task.

The histogram distribution of the internal radial velocity error is presented in Fig. 29 top panel. The different histograms contain data new to each data release as indicated in the top right corner. The bottom panel of Fig. 29 is the associated cumulative distribution of internal radial velocity error. The figure shows a clear improvement of the quality of the radial velocity from DR1 towards DR4, with a jump in quality for data new to DR4. From DR2 to DR4¹², while the mode of the distribution remains constant at ~ 1 km s⁻¹, the tail at larger velocity errors is consistently reduced with a leap between DR3 and DR4. Indeed, while for DR3 68% of the data had internal errors better than 2 km s⁻¹, for DR4 the 68% limit goes down to 1.4 km s⁻¹. The source of this improvement is two-fold. First the DR4 data are based upon a new input catalog which uses DENIS *I*-band magnitude instead of a pseudo-*I* magnitude constructed from Tycho-2 B_T and V_T photometry for the bright part of the catalog and photographic *I*-band from the SuperCosmos Sky Survey for the faint part. This more accurate photometry allows a better splitting of the bright and faint sub-samples which have different exposure times. Second, at the telescope the signal-to-noise ratio is now “monitored”, and fields with insuffi-

¹² DR1 data suffer from second order contamination, which was corrected for DR2 data, hence the radial velocity measurement is not as precise as for subsequent releases.

cient SNR benefit from longer exposure times to ensure a minimal quality of the data. The combination of these two points allows us to considerably reduce the tail of the radial velocity error distribution.

8.1. Repeat observations

To verify the quality of the RAVE data, a fraction of the survey time is devoted to multiple observations of RAVE targets with time intervals between observations ranging from a few hours to 4 years. 23,288 stars in the present release belong to this programme for a total of 61,457 measurements, some stars having been observed up to 13 times. The distribution of the number of observations per star is presented in the left panel of Fig. 30. The distribution of the time interval Δt between re-observations is presented in Fig. 30, right panel, where the Δt are binned using intervals of one day. As seen from this figure, the distribution is not random. A quasi-logarithmic spacing is used to sample optimally the possible orbital state of the spectroscopic binaries with an enhancement of the observations at specific intervals of one day, 2 weeks, 1, 2 and 3 months, 6 months and 1, 2, 3 and 4 years.

The comparison between the radial velocity measurements for the different observations is given in Fig. 31. In the top panel, the colour coding follows the density per bin of 2 km s⁻¹. For each star, the velocity of the observation with the highest SNR is used as the reference velocity along the x-axis (HRV_1) while subsequent observations are along the y-axis (HRV_2). The measurements are convolved with a Gaussian function along each direction. The dispersion of the Gaussian is the internal error associated with the measurement along each axis. The general trend follows closely the one-to-one relation, showing no sign of any systematic effects.

Another way to look quantitatively at the radial velocity difference is presented in the bottom panel of Fig. 31, which shows the histogram of the radial velocity difference normalised to the errors $\Delta_{HRV} = (HRV_1 - HRV_2) / (\sqrt{\sigma_1^2 + \sigma_2^2})$. If our measurements were perfect, this distribution should follow a Gaussian function of zero mean and unit dispersion. Binaries and problematic measurements contribute to the tail and can be assumed to follow a Gaussian function with a larger dispersion. In the case of our RAVE data, a sum of two Gaussians is used to fit the histogram, setting the dispersion of the first Gaussian function to one. Also, we remove the central bin from the fit. This central bin is mostly populated by repeat observations without delay in time. The best fit is shown as a continuous black line, the contribution of each Gaussian function being represented by a dashed line. Apart from the central bin, the fit provides an adequate representation of the observed histogram. The respective contributions of the two Gaussian functions is 77% for the standard population and 23% for the spectroscopic binaries/problematic observations. This fraction is in agreement with our finding for DR3 data (26%).

8.2. Zero point offset

As for the DR3 and previous releases, the radial velocity solutions are corrected for potential zero-point offsets due to change in temperature in the spectrograph room. The procedure uses the available sky lines in

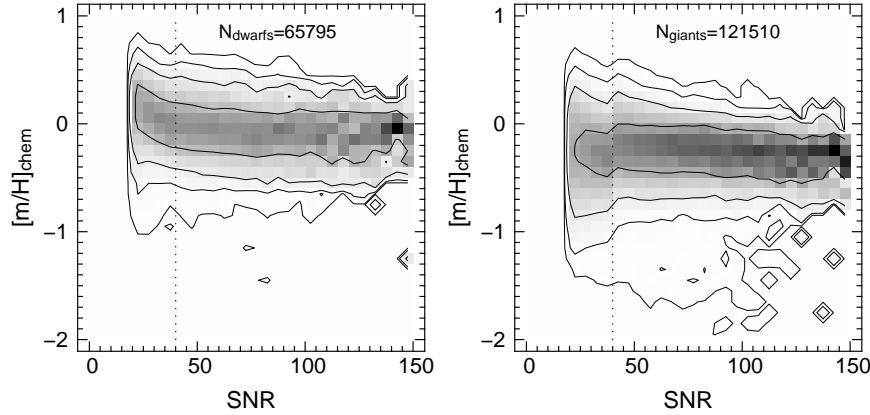


FIG. 26.— $[m/H]_{\text{chem}}$ distribution for dwarfs (left panel) and giants (right panel) as a function of signal-to-noise SNR. In order to highlight the shape of the distribution at any SNR, the $[m/H]_{\text{chem}}$ distribution has been normalised for every SNR bin.

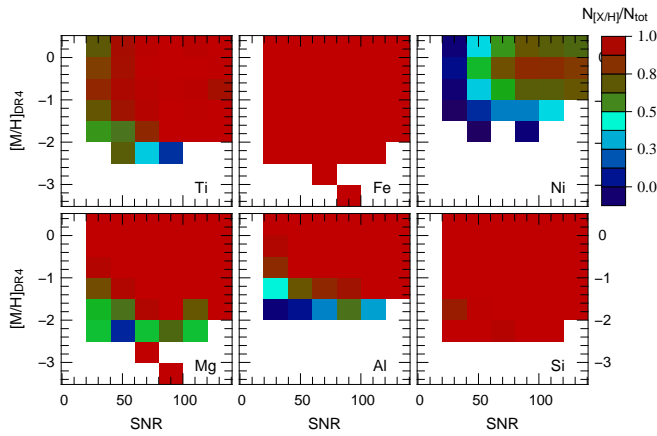


FIG. 27.— The colours of the bins represent the number of spectra having abundance estimation (N_X/N_{tot}) as a fraction of the total number of spectra as a function of metallicity and SNR. Each panel shows the distribution for the identified element.

the RAVE spectra to construct a smooth solution of the zero point offset across the field plate. This procedure is fully described in (Siebert et al. 2011b) and the relevant measurements for each fibre are given in the catalogue. To verify the validity of our velocity zero point solution, comparison to independent measurements is made. Our comparison sample comprises data from seven different sources: the Geneva-Copenhagen Survey (GCS, Nordström et al. 2004b), Chubak et al. (2012) data and high-resolution echelle follow-up observations of RAVE targets at the ANU 2.3m telescope, Asiago observatory, Apache Point Observatory from Ruchti et al. (2011) and Observatoire de Haute Provence using the Elodie and Sophie instruments. In total, the sample of RAVE stars with external radial velocity measurements contains 1265 stars. Their distributions in DENIS I magnitude and 2MASS $J - H$ vs $H - K$ color-color diagram are presented in Fig. 32. Stars with $I < 9$ are mostly custom RAVE observations of bright GCS stars. At fainter magnitudes the sample consists primarily of high resolution re-observations of RAVE targets. In the 2MASS

TABLE 6
SUMMARY OF THE RADIAL VELOCITY COMPARISON TO EXTERNAL SAMPLES.

Sample	N_{stars}	N_{obs}	$\langle \Delta RV \rangle$	$\sigma_{\Delta RV} (\sigma_{\text{clip}}, n_{\text{rej}})$
GCS	733	1024	0.28	1.72 (3,120)
Chubak	77	97	-0.07	1.28 (3,2)
Ruchti	314	445	0.78	1.78 (3,34)
Asiago	25	47	-0.22	2.95 (3,0)
ANU 2.3m	73	203	-0.60	2.87 (3,18)
OHP Elodie	9	13	0.29	0.40 (2.5,3)
OHP Sophie	34	43	0.83	1.56 (3,4)
Full sample	1265	1872	0.20	1.52 (3,266)

^aThe mean difference in the radial velocities, ΔRV , has been computed as following: $\Delta RV = RV_{\text{DR4}} - RV_{\text{ext}}$

colour-colour diagram, we observe that this sample covers the two main peaks (representing dwarf and giant stars) present in the RAVE catalog. However, dwarfs are over-represented compared to the RAVE distribution due to the large number of GCS stars observed in this sample which are Hipparcos dwarfs.

The summary of the comparison to the control samples is given in Table 6. This table reports the number of objects in each sample, the total number of observations, the mean $\Delta RV = RV_{\text{DR4}} - RV_{\text{ext}}$ and the standard deviation. ΔRV is computed using an iterative σ -clipping technique to remove the contamination by spectroscopic binaries or problematic measurements. No other quality cut was applied on the samples. The clipping parameter and the number of stars rejected for each sample is given in the last column of the table.

We note that the agreement between RAVE and the external sources is better than 1 km s^{-1} in all the cases. Fig. 33 top panel presents the direct comparison of the DR4 radial velocities to the external source measurements. The blue circles are the known spectroscopic binaries and show a broader distribution than the remainder of the sample. Figure 33 bottom panel shows the histogram of the radial velocity difference. This distribution can be adequately reproduced by the sum of two Gaussian functions, the peak representing the single stars being of zero mean with a dispersion of 1.5 km s^{-1} , consistent with our expectation for RAVE data.

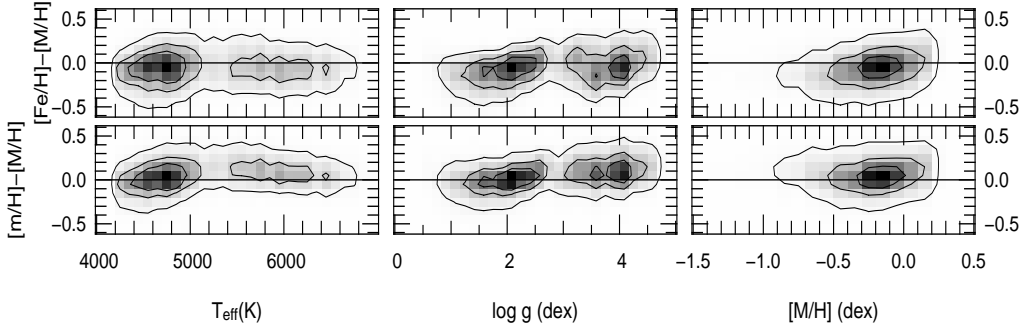


FIG. 28.— Residuals between the DR4 metallicity ($[M/H]$), the chemical pipeline metallicity ($[m/H]$) and the measured iron abundance ($[Fe/H]$) as a function of the effective temperature, surface gravity and metallicity. The contour levels hold 34%, 68% and 95% of the points, respectively.

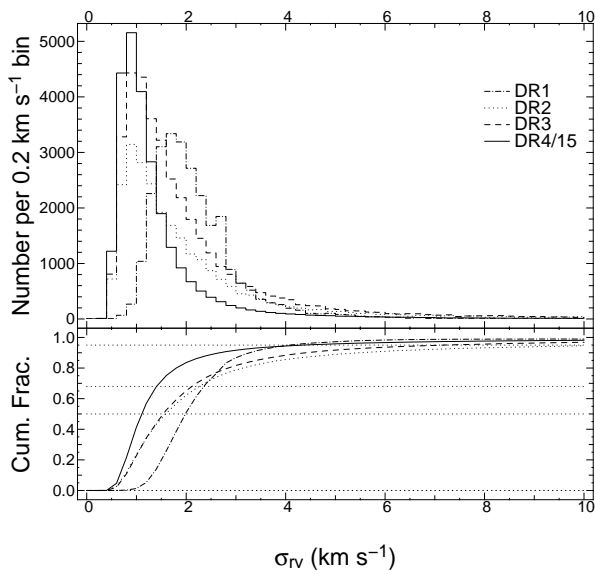


FIG. 29.— **Top:** histograms of the internal radial velocity error for data new to each data release. The bin size is 0.2 km s^{-1} . For DR4, the number of stars per bin is divided by 15 to compensate for the increase in sample size. **Bottom:** cumulative distributions. The dotted lines mark 50, 68 and 95% of the samples.

As a final test, we check the dependence of the radial velocity difference as a function of the Tonry-Davis correlation coefficient (R) and signal-to-noise of the RAVE data (Fig. 34). Although an increase in the dispersion is observed for $\text{SNR} < 30 \text{ pixel}^{-1}$, or R of 40, the absence of an apparent bias indicates that our radial velocity measurements are reliable.

9. STELLAR DISTANCES, AGES AND EXTINCTIONS

In the absence of parallaxes for the stars, the best way to obtain individual stellar distances is to project the atmospheric parameters on a set of theoretical isochrones and obtain the most likely value of the absolute magnitude of the stars. Up to now, the RAVE consortium has published a variety of studies using the distances inferred by red clump giants (e.g.: Siebert et al. 2008; Veltz et al. 2008; Williams et al. 2013), and developed three different methods in order to obtain the individual stel-

lar line-of-sight distances (Breddels et al. 2010; Zwitter et al. 2010; Burnett & Binney 2010). Previous RAVE catalogues published the derived distances for the first two of these methods.

Figure 35 presents for different regions of the $T_{\text{eff}} - \log g$ diagram, the ratio between the distances obtained using the Zwitter et al. (2010) method with the DR3 parameters (Z10-DR3 hereafter) and with the DR4 ones (Z10-DR4 hereafter). It should be noted that Z10-DR3 distances have been obtained using only internal errors for the atmospheric parameters, whereas Z10-DR4 consider the quadratic sum of the external uncertainties (Table 5) and the internal ones (Table 1 or Table 2). One can see that the largest deviations in distances occur in parts of the H-R diagram which are (and should be) scarcely populated. As an overall mean, the Z10-DR3 distances are 6% larger than the Z10-DR4 ones, with the 1σ dispersion being at roughly 30%.

For the present DR4 catalogue, we publish two sets of distances: one using the Z10 method with the DR4 parameters, as well as another set obtained using a more robust algorithm, based on the Bayesian distance-finding method of Burnett & Binney (2010). The improved algorithm is presented in Binney et al. (2013, B13 hereafter), and now takes into account the interstellar extinction, as well as kinematic correction factors obtained by the method of Schönrich, Binney, & Asplund (2012). The pipeline determines the probability distribution function of each star in the space of initial mass, age, metallicity, distance, extinction, etc., and from this distribution an age, a distance and an extinction are inferred from appropriate expectation values. The most reliable distance indicator turns out to be not the expectation value of the distance but the inverse of the expectation value of the parallax. Here we discuss briefly the results for only the distances, but we refer the reader to B13 for a full explanation of the method as well as a detailed analysis of the reliability of the parameters.

The B13-DR4 spectrophotometric parallaxes have been computed for the stars which had spectra with $\text{SNR} > 10 \text{ pixel}^{-1}$. For the targets that were observed several times, only the spectrum with the highest SNR

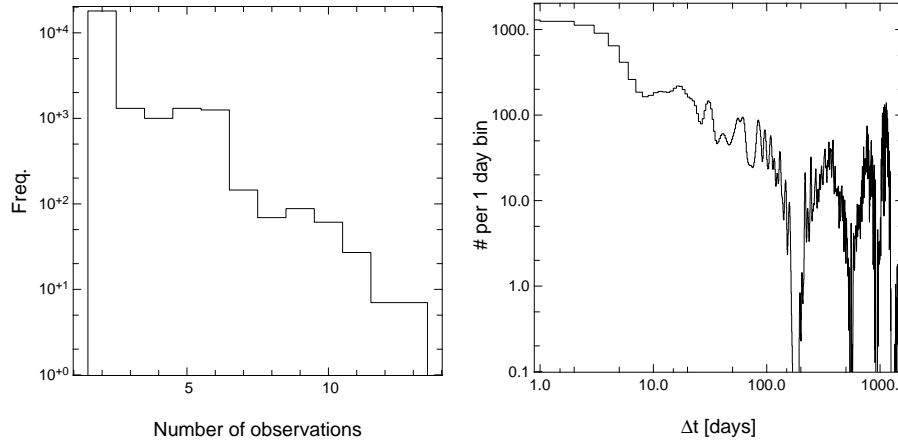


FIG. 30.— Left: histogram of the number of observations for stars observed more than once. Right: distribution of the time intervals between the first observation of a star and its re-observation.

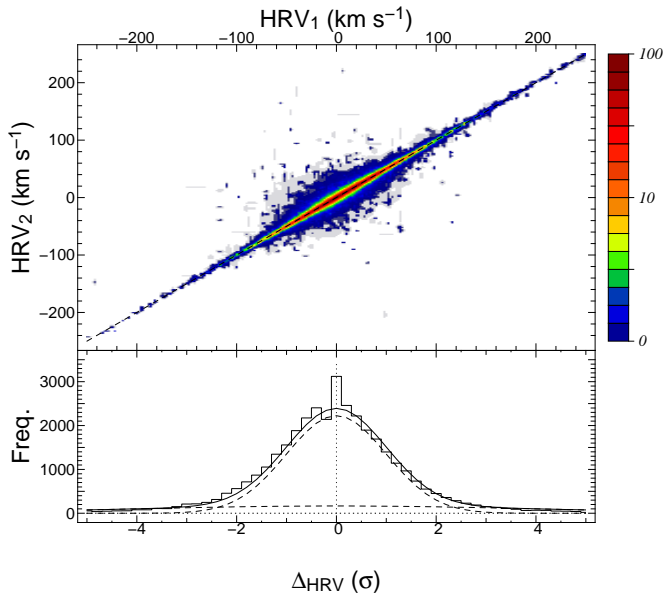


FIG. 31.— Top: comparison of the radial velocities measured for re-observed RAVE targets. For each star in this sample, the measurement with highest SNR is used as the reference point on the x-axis (HRV_1) while other measurements are along the y-axis (HRV_2). Along each axis the distribution is obtained by convolving the measurement with a Gaussian function whose dispersion is the associated internal error. The colour-coding follows the resulting density on a logarithmic scale. The one-to-one relation is indicated by the dashed line. Bottom: histogram of the radial velocity differences normalised to the error. The plain black line is a fit to the histogram assuming that it is composed of two Gaussian populations (see text). From this fit, the contribution to the histogram of spectroscopic binaries and problematic spectra is 23%.

has been used every time. The results have shown that the spectrophotometric parallaxes of Hipparcos stars are very satisfactory and are definitely improved by taking extinction into account. Nevertheless, an over-estimation of less than 10% for the dwarfs and less than 20% for the giants is evident. The method has also been tested on the open cluster spectra presented in Table 4, deriving very satisfactory distances, provided a cluster-specific age prior is used. Indeed, our data barely constrain the ages of stars, so a star’s adopted age is heavily influenced

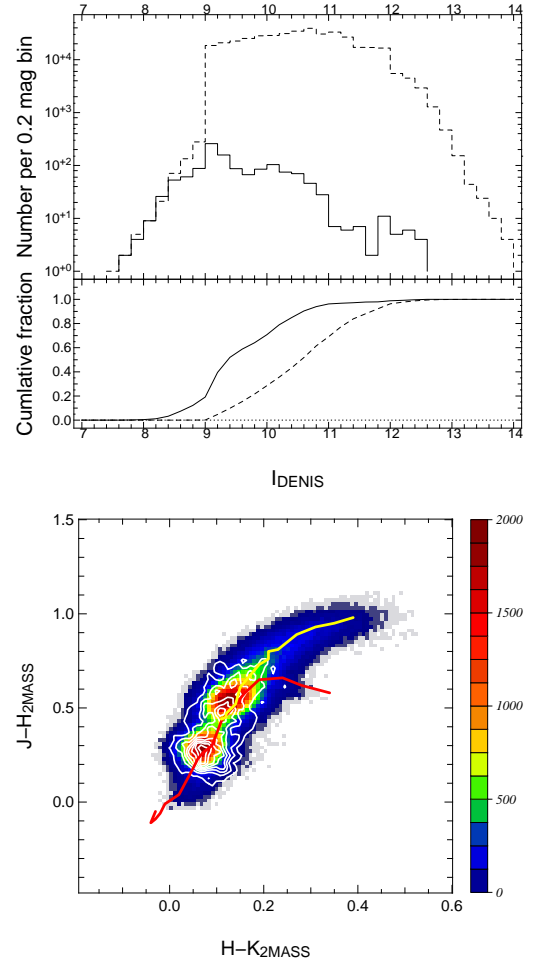


FIG. 32.— Top: DENIS I magnitude histogram of the sub-sample of RAVE stars with external radial velocity measurements (plain line) compared to the distribution of DENIS I magnitude for the full RAVE catalog (dashed line). Bottom: 2MASS $J-H$ vs $H-K$ two dimensional histogram of the RAVE DR4 catalog with a bin size of 0.02 magnitude on each axis. The contours show the location of the sub-sample with external HRV measurements. The thick yellow and red lines are fiducial colours from Table 2 of Wainscoat et al. (1992) for giant and dwarf stars respectively.

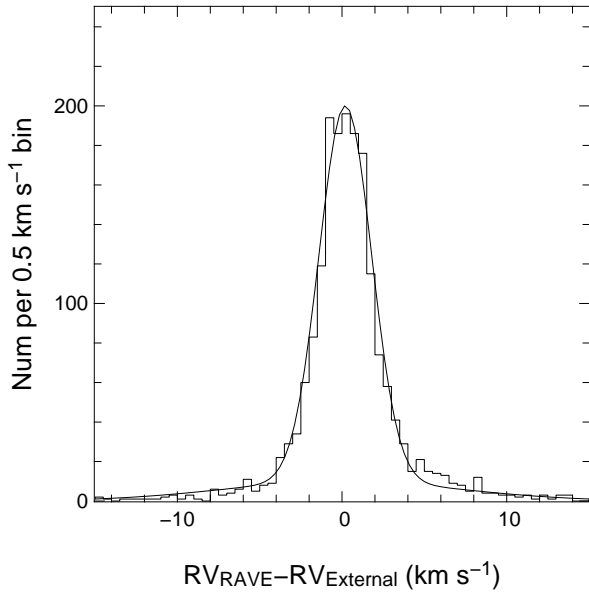
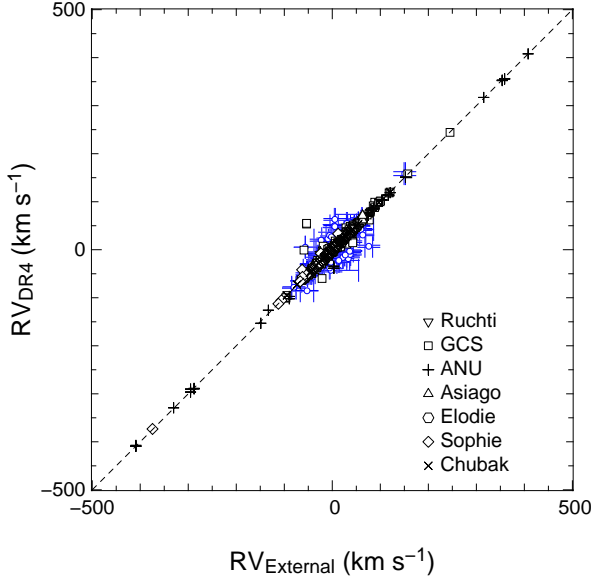


FIG. 33.— Top: Comparison of RAVE radial velocities to external measurements. The blue circles are spectroscopic binaries detected in the high-resolution spectra. The dashed line marks the one to one relation. Bottom: Histogram of the radial velocity difference. The histogram can be modelled using two Gaussian functions to account for normal stars and binaries/problematic spectra (black curve). The Gaussian function recovering the peak is at zero mean with a standard deviation of 1.5 km s^{-1} . The problematic spectra/binaries contribution to this sample is 5%.

by the age prior used, and the prior that is appropriate for field stars leads to excessive ages being assigned to most cluster stars, which tend to be young.

Figure 36 compares the distance estimations obtained using the Padova isochrones and the Z10-DR4 or the B13-DR4 methods. From this figure one can see that for the bulk of the targets, the distances obtained with the two methods are quite similar. We find that the median of the distribution defined by Z10/B13 is equal to 1.02. However, for the most distant stars ($D \gtrsim 2 \text{ kpc}$) Z10-DR4 predicts larger distances than B13-DR4. Finally,

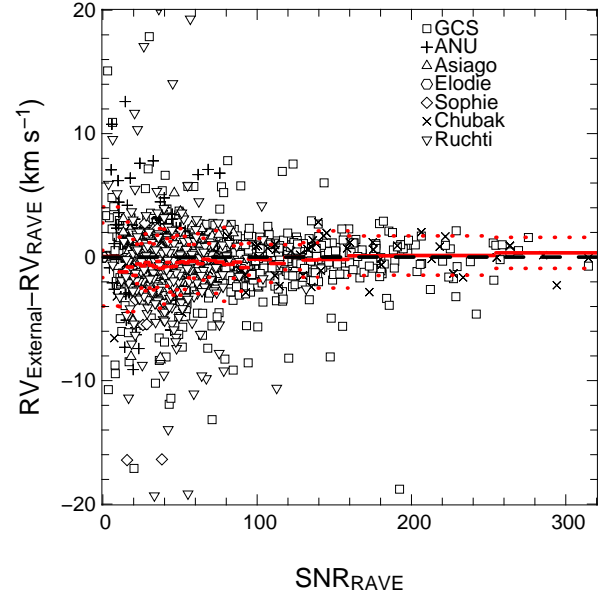
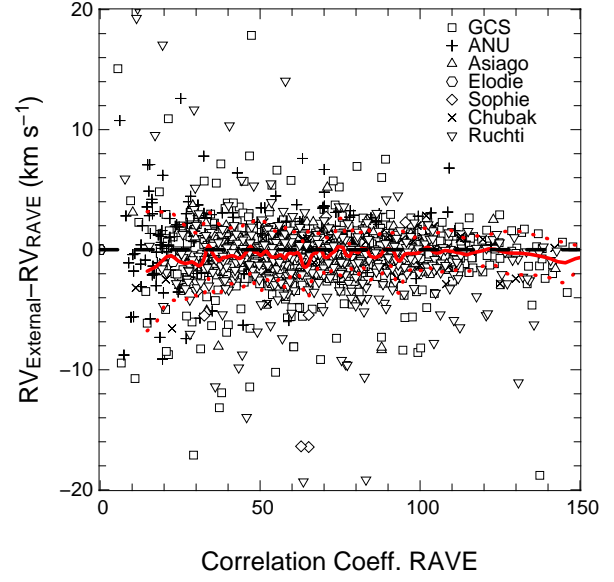


FIG. 34.— Radial velocity difference as a function of Tonry-Davis correlation coefficient (upper plot) and signal to noise (lower plot). The thick red line marks the mean relation, the red dotted line the dispersion. The symbols indicate the source of the external measurements.

the targets for which B13-DR4 predicts $D \sim 0.5 \text{ kpc}$ and Z10-DR4 derives $D > 1.5 \text{ kpc}$ correspond to the most metal-poor giant stars of the sample, for which the atmospheric parameters have also the largest errors. This disagreement is mainly due to the fact that Z10 projects the atmospheric parameters on the isochrones, without having any *a priori* constraint on their expected output parameters, based on their position in the Galaxy, their radial velocity or proper motion. Hence, input atmospheric parameter values with large uncertainties, especially for metal-poor giant stars, naturally lead to erroneous distances and to the discrepancy shown in Fig. 36.

We conclude that the B13-DR4 distances are more robust and hence should give better results if the priors are satisfied.

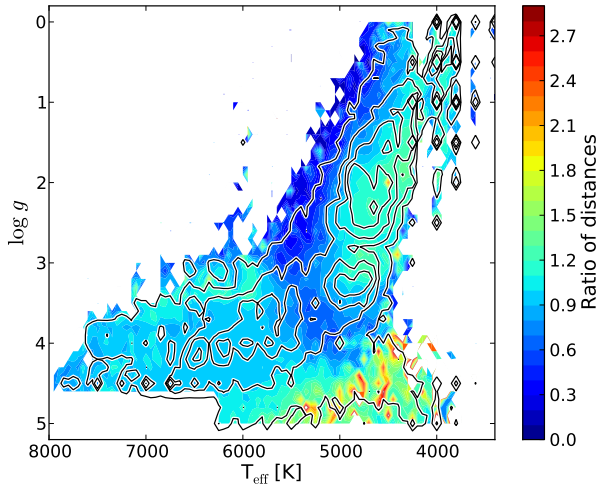


FIG. 35.— Comparison of the average ratio of distances in the $T_{\text{eff}}-\log g$ plot for the stellar spectra with $\text{SNR} > 20 \text{ pixel}^{-1}$. The ratio is the Zwitter et al. (2010) distance based on DR3 parameters divided by the Zwitter et al. (2010) distance based on DR4 parameters. The ratio is in filled contours, bin size is 50 K in temperature and 0.1 dex in gravity. Empty contours show occurrence of T_{eff} and $\log g$ (expectation values) as calculated by DR4.

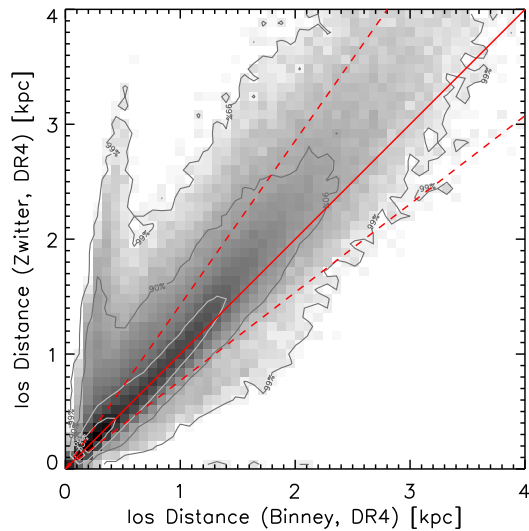


FIG. 36.— Comparison of the line-of-sight distance estimations obtained using the Binney et al. (2013) method (x -axis) and the ones obtained using the Zwitter et al. (2010) method combined with the Padova isochrones (y -axis). Red line is the 1:1 relation and dashed lines show deviations of 30% from unity. Contour lines hold 33%, 66%, 90% and 99% of the sample.

10. PHOTOMETRY FROM APASS

$BVg'r'i'$ photometric data of RAVE stars have been obtained as part of the ongoing APASS survey (Henden et al. 2013, Munari et al. 2013a,b). The APASS photometric survey covers the whole sky, from Pole to Pole, with ongoing observations from CTIO (Chile), for the southern hemisphere, and New Mexico for the northern counterpart. At both sites, a pair of twin remotely controlled, small telescopes obtain simultaneous CCD observations during dark- and grey-Moon time over five optical

bands: B, V (tied to the equatorial standards of Landolt 2009) and g', r', i' bands (tied to the 158 primary standards given by Smith et al. 2002, that define the Sloan photometric system). The telescopes are 20cm f/3.6 astrographs feeding Apogee U16m cameras (4096×4096 array, $9 \mu\text{m}$ pixels), that cover a field 2.9 deg wide with a 2.6 arcsec/pix plate factor. The photometric filters are of the dielectric multi-layer type and are produced by Astrodon. Transmission curves and photometric performances of Astrodon filters used in the APASS survey are discussed and compared to more conventional types of photometric filters in Munari et al. (2012) and Munari & Moretti (2012). On average 80 fields are observed per night at each APASS location, 20 of them being standard fields (Landolt, Sloan).

The APASS observations are obtained with fixed exposure times (different and optimised for each photometric band), set to detect $V=17$ stars at $\text{SNR}=5$ on a single exposure. Stars brighter than $V=10$ mag may saturate under optimal seeing conditions. At the time of writing, 90% of the whole sky has been covered, with 42 million stars measured on at least two distinct epochs. Differential photometry within a given field is accurate to better than 0.01 mag, absolute photometry over the whole sky is currently accurate to better than 0.025 mag (closely similar to 2MASS accuracy). APASS astrometric positions are also highly accurate. Comparison with the positions given in the Carlsberg Meridian Catalog for the 118 940 RAVE stars in common shows a distribution peaked at a separation of 0.105 arcsec, with the median value at 0.177 arcsec. Although APASS DR7 is publicly available, its values are not published in RAVE DR4, because future APASS DR will provide better accuracy and coverage of RAVE DR4. Clearly APASS photometry will significantly enhance analysis of RAVE data. We recommend users to adopt APASS photometry as it becomes available.

11. CONCLUSIONS

The fourth public data release of the RAVE survey includes the stellar atmospheric parameters of 482 430 spectra obtained from April 2004 to December 2012. Compared to the previous catalogue of DR3, a new input catalogue, based on DENIS DR3 and 2MASS, is used to select the observed targets. The new input catalogue has the major new feature of extending to lower Galactic latitudes and providing more accurate astrometry, leading to fibre placement better matching stellar positions on the sky, which results in higher signal-to-noise spectra. In addition, the parameters have been revisited, thanks to a new pipeline, presented in Kordopatis et al. (2011a), and 809 reference spectra that allowed us to validate the effective temperatures and surface gravities, and calibrate the metallicities. The RAVE stellar atmospheric parameters that are obtained with the new pipeline are free of any obvious systematics (no correlations between the derived parameters or as function of signal-to-noise), in particular for the overall metallicities of the stars. The spectra with the lowest signal-to-noise ratio have a distribution function of atmospheric parameter values which shows a well-understood pattern of discretisation effects, but it has been shown that this discretisation does not alter the accuracy of the derived parameters. We show that the metallicity distribution func-

tions of the observed stars shift towards lower metallicity values for the lower surface gravity bins, at the same time as the radial velocity dispersion increases. This is in agreement with a change in the mixture of the probed Galactic populations as a function of the probed volume, passing from an old thin disc dominated population to the presence of more halo stars for the larger volume probed by the more luminous giant stars in low surface gravity bins. That is, at face value the distribution functions for derived stellar parameters are consistent with plausible astrophysical expectations.

In addition to the atmospheric parameters obtained with the new pipeline, those obtained with the DR3 pipeline are also published since they have been used in published analyses. However, they are of lower reliability than our DR4 dataset, so situations demanding their

re-analysis should be rather rare.

The abundances of six individual elements, namely aluminium, silicon, titanium, iron, magnesium and nickel are published, using an improved version of the Boeche et al. (2011) chemical pipeline. The reliability of these elemental abundances varies according to the effective temperature, surface gravity and metallicity of the star, the signal-to-noise ratio of the spectrum, and of course the element itself.

The catalogue also includes the line-of-sight distances computed using the methods presented in Binney et al. (2013) and Zwitter et al. (2010) as well as the ages and the interstellar extinctions which are a sub-product of the Binney et al. (2013) pipeline. Radial velocities, photometric information, proper motions, and stellar binarity flags complete the DR4 catalogue entries.

APPENDIX

APPENDIX MATERIAL

Table 7 describes the contents of individual columns of the Fourth Data Release catalog. The catalog is accessible online at <http://www.rave-survey.org> and via the CDS VizieR service.

REFERENCES

- Abadi, M. G., Navarro, J. F., Steinmetz, M., & Eke, V. R. 2003, *ApJ*, 591, 499
- Allende Prieto, C., Barklem, P. S., Lambert, D. L., & Cunha, K. 2004, *A&A*, 420, 183
- Alvarez, R., & Plez, B. 1998, *A&A*, 330, 1109
- Antoja, T., Helmi, A., Bienaymé, O., et al. 2012, *MNRAS*, 426, L1
- Asplund, M., Grevesse, N., & Sauval, A. J. 2005, in *Astronomical Society of the Pacific Conference Series*, Vol. 336, *Cosmic Abundances as Records of Stellar Evolution and Nucleosynthesis*, ed. T. G. Barnes, III & F. N. Bash, 25
- Bijaoui, A., Recio-Blanco, A., de Laverny, P., & Ordenovic, C. 2012, *Statistical methodology*, 9, 55
- Binney, J., Burnett, B., Kordopatis, G., & RAVE collaboration. 2013, submitted
- Boeche, C., Siebert, A., Williams, M., et al. 2011, *AJ*, 142, 193
- Brault, J., & Neckel, H. 1987, *Spectral Atlas of Solar Absolute Disk-Averaged and Disk-Center Intensity from 3290 to 12510 Å*, available from <ftp.hs.uni-hamburg.de/pub/outgoing/FTS-Atlas/>
- Breddels, M. A., Smith, M. C., Helmi, A., et al. 2010, *A&A*, 511, A90
- Bruce, S. F., Higinbotham, J., Marshall, I., & Beswick, P. H. 2000, *J. Magn. Reson.*, 142, 57
- Burnett, B., & Binney, J. 2010, *MNRAS*, 407, 339
- Burnett, B., Binney, J., Sharma, S., et al. 2011, *A&A*, 532, A113
- Carretta, E., Bragaglia, A., & Cacciari, C. 2004, *ApJ*, 610, L25
- Casagrande, L., Ramírez, I., Meléndez, J., Bessell, M., & Asplund, M. 2010, *A&A*, 512, A54
- Casagrande, L., Schönrich, R., Asplund, M., et al. 2011, *A&A*, 530, A138
- Cayrel, R., Depagne, E., Spite, M., et al. 2004, *A&A*, 416, 1117
- Chubak, C., Marcy, G., Fischer, D. A., et al. 2012, *ArXiv e-prints DENIS Consortium. 2003, VizieR Online Data Catalog*, 1, 2002
- Freeman, K., & Bland-Hawthorn, J. 2002, *ARA&A*, 40, 487
- Fuhrmann, K. 1998a, *A&A*, 338, 161
- . 1998b, *A&A*, 330, 626
- . 2004, *Astronomische Nachrichten*, 325, 3
- . 2008, *MNRAS*, 384, 173
- Fulbright, J. P., Wyse, R. F. G., Ruchti, G. R., et al. 2010, *ApJ*, 724, L104
- Girard, T. M., van Altena, W. F., Zacharias, N., et al. 2011, *AJ*, 142, 15
- Gratton, R., Sneden, C., & Carretta, E. 2004, *ARA&A*, 42, 385
- Gratton, R. G., Carretta, E., & Castelli, F. 1996, *A&A*, 314, 191
- Gratton, R. G., Carretta, E., Claudi, R., Lucatello, S., & Barbieri, M. 2003, *A&A*, 404, 187
- Gratton, R. G., Bonifacio, P., Bragaglia, A., et al. 2001, *A&A*, 369, 87
- Grevesse, N. 2008, *Communications in Asteroseismology*, 157, 156
- Grevesse, N., & Sauval, A. J. 1998, *Space Sci. Rev.*, 85, 161
- Gustafsson, B., Edvardsson, B., Eriksson, K., et al. 2008, *A&A*, 486, 951
- Hambly, N. C., MacGillivray, H. T., Read, M. A., et al. 2001, *MNRAS*, 326, 1279
- Hekker, S., & Meléndez, J. 2007, *A&A*, 475, 1003
- Helmi, A., White, S. D. M., de Zeeuw, P. T., & Zhao, H. 1999, *Nature*, 402, 53
- Hinkle, K., Wallace, L., Livingston, W., et al. 2003, in *The Future of Cool-Star Astrophysics: 12th Cambridge Workshop on Cool Stars, Stellar Systems, and the Sun (2001 July 30 - August 3)*, eds. A. Brown, G.M. Harper, and T.R. Ayres, (University of Colorado), 2003, p. 851-856., ed. A. Brown, G. M. Harper, & T. R. Ayres, Vol. 12, 851-856
- Høg, E., Fabricius, C., Makarov, V. V., et al. 2000, *A&A*, 355, L27
- Kielkopf, J. F. 1973, *Journal of the Optical Society of America (1917-1983)*, 63, 987
- Kirby, E. N., Guhathakurta, P., Bolte, M., Sneden, C., & Geha, M. C. 2009, *ApJ*, 705, 328
- Koch, A., & McWilliam, A. 2011, *AJ*, 142, 63
- Kordopatis, G., Recio-Blanco, A., de Laverny, P., et al. 2011a, *A&A*, 535, A106
- . 2011b, *A&A*, 535, A107
- Landolt, A. U. 2009, *AJ*, 137, 4186
- Luck, R. E., & Heiter, U. 2006, *AJ*, 131, 3069
- . 2007, *AJ*, 133, 2464
- Matijević, G., Zwitter, T., Munari, U., et al. 2010, *AJ*, 140, 184
- Matijević, G., Zwitter, T., Bienaymé, O., et al. 2011, *AJ*, 141, 200
- . 2012, *ApJS*, 200, 14
- McWilliam, A. 1990, *ApJS*, 74, 1075
- Mishenina, T. V., Bienaymé, O., Gorbaneva, T. I., et al. 2006, *A&A*, 456, 1109
- Mishenina, T. V., & Kovtyukh, V. V. 2001, *A&A*, 370, 951
- Mishenina, T. V., Soubiran, C., Bienaymé, O., et al. 2008, *A&A*, 489, 923
- Mishenina, T. V., Soubiran, C., Kovtyukh, V. V., & Korotin, S. A. 2004, *A&A*, 418, 551
- Munari, U., & Moretti, S. 2012, *Baltic Astronomy*, 21, 22
- Munari, U., Sordo, R., Castelli, F., & Zwitter, T. 2005, *A&A*, 442, 1127
- Munari, U., Bacci, S., Baldinelli, L., et al. 2012, *Baltic Astronomy*, 21, 13
- Nordström, B., Mayor, M., Andersen, J., et al. 2004a, *A&A*, 418, 989
- . 2004b, *A&A*, 418, 989
- Pace, G., Pasquini, L., & François, P. 2008, *A&A*, 489, 403
- Pancino, E., Carrera, R., Rossetti, E., & Gallart, C. 2010, *A&A*, 511, A56
- Pasetto, S., Grebel, E. K., Zwitter, T., et al. 2012a, *A&A*, 547, A70
- . 2012b, *A&A*, 547, A71
- Pasquini, L., Randich, S., Zoccali, M., et al. 2004, *A&A*, 424, 951
- Ramírez, I., Allende Prieto, C., & Lambert, D. L. 2007, *A&A*, 465, 271
- Ramírez, S. V., & Cohen, J. G. 2003, *AJ*, 125, 224
- Recio-Blanco, A., Bijaoui, A., & de Laverny, P. 2006, *MNRAS*, 370, 141

TABLE 7
CATALOGUE DESCRIPTION

Col	Format	Units	NULL	Label	Explanations
1	char(32)	-	N	RAVE_OBS.ID	Target designation
2	char(18)	-	N	RAVEID	RAVE target designation
3	double	deg	N	RAdeg	Right ascension
4	double	deg	N	DEdeg	Declination
5	double	deg	N	Glon	Galactic longitude
6	double	deg	N	Glat	Galactic latitude
7	float	km/s	N	HRV	Heliocentric radial velocity
8	float	km/s	N	eHRV	HRV error
9	float	(R+)	N	CorrelationCoeff	Tonry & Davis R correlation coefficient
10	float	-	N	PeakHeight	Height of correlation peak
11	float	-	N	PeakWidth	Width of correlation peak
12	float	km/s	Y	SkyRV	Measured HRV of Sky
13	float	km/s	Y	eSkyRV	Error Measured HRV of Sky
14	float	(R+)	Y	SkyCorrelationCoeff	Tonry & Davis R Sky correlation coefficient
15	float	km/s	Y	CorrectionRV	Zero point correction applied Radial Velocity
16	char(5)	-	Y	ZeroPointFLAG	Quality flag for Zero point correction (Note 3)
17	char(16)	-	Y	ID_TYCHO2	TYCHO2 Target designation
18	float	arcsec	Y	Dist_TYCHO2	Center distance to target catalog
19	char(2)	-	Y	XidQualityFLAG_TYCHO2	Crossmatch quality flag (Note 4)
20	float	mas/yr	Y	pmRA_TYCHO2	Proper motion RA from TYCHO2
21	float	mas/yr	Y	epmRA_TYCHO2	error Proper motion RA from TYCHO2
22	float	mas/yr	Y	pmDE_TYCHO2	Proper motion DE from TYCHO2
23	float	mas/yr	Y	epmDE_TYCHO2	error Proper motion DE from TYCHO2
24	char(16)	-	Y	ID_UCAC2	UCAC2 Target designation
25	float	arcsec	Y	Dist_UCAC2	Center distance to target catalog
26	char(2)	-	Y	XidQualityFLAG_UCAC2	Crossmatch quality flag (Note 4)
27	float	mas/yr	Y	pmRA_UCAC2	Proper motion RA from UCAC2
28	float	mas/yr	Y	epmRA_UCAC2	error Proper motion RA from UCAC2
29	float	mas/yr	Y	pmDE_UCAC2	Proper motion DE from UCAC2
30	float	mas/yr	Y	epmDE_UCAC2	error Proper motion DE from UCAC2
31	char(16)	-	Y	ID_UCAC3	UCAC3 Target designation
32	float	arcsec	Y	Dist_UCAC3	Center distance to target catalog
33	char(2)	-	Y	XidQualityFLAG_UCAC3	Crossmatch quality flag (Note 4)
34	float	mas/yr	Y	pmRA_UCAC3	Proper motion RA from UCAC3
35	float	mas/yr	Y	epmRA_UCAC3	error Proper motion RA from UCAC3
36	float	mas/yr	Y	pmDE_UCAC3	Proper motion DE from UCAC3
37	float	mas/yr	Y	epmDE_UCAC3	error Proper motion DE from UCAC3
38	char(16)	-	Y	ID_UCAC4	UCAC4 Target designation
39	float	arcsec	Y	Dist_UCAC4	Center distance to target catalog
40	char(2)	-	Y	XidQualityFLAG_UCAC4	Crossmatch quality flag (Note 4)
41	float	mas/yr	Y	pmRA_UCAC4	Proper motion RA from UCAC4
42	float	mas/yr	Y	epmRA_UCAC4	error Proper motion RA from UCAC4
43	float	mas/yr	Y	pmDE_UCAC4	Proper motion DE from UCAC4
44	float	mas/yr	Y	epmDE_UCAC4	error Proper motion DE from UCAC4
45	char(16)	-	Y	ID_PPMXL	PPMXL Target designation
46	float	arcsec	Y	Dist_PPMXL	Center distance to target catalog
47	char(2)	-	Y	XidQualityFLAG_PPMXL	Crossmatch quality flag (Note 4)
48	float	mas/yr	Y	pmRA_PPMXL	Proper motion RA from PPMXL
49	float	mas/yr	Y	epmRA_PPMXL	error Proper motion RA from PPMXL
50	float	mas/yr	Y	pmDE_PPMXL	Proper motion DE from PPMXL
51	float	mas/yr	Y	epmDE_PPMXL	error Proper motion DE from PPMXL
52	char(10)	-	N	Obsdate	Observation date yyyyymmdd
53	char(14)	-	N	FieldName	Name of RAVE field (RA/DE)
54	int	-	N	PlateNumber	Number of field plate [1..3]
55	int	-	N	FiberNumber	Number of optical fiber [1,150]
56	float	K	Y	Teff_K	Effective temperature (Note 1)
57	float	K	Y	eTeff_K	Error Effective temperature (Note 1)
58	float	dex	Y	logg_K	Log gravity (Note 1)
59	float	dex	Y	elogg_K	Error Log gravity (Note 1)
60	float	dex	Y	Met_K	Metallicity [m/H](Note 1)
61	float	dex	Y	Met_N_K	Metallicity [m/H](Note 1)
62	float	dex	Y	eMet_K	ErrorMetallicity [m/H] (Note 1)
63	float	-	Y	SNR_K	Signal to Noise value (Note 1)
64	float	-	Y	Algo_Conv_K	Quality Flag for Stellar Parameter pipeline [0..4] (Note 1, Note 5)
65	float	dex	Y	Al	Abundance of Al [Al/H]
66	int	-	Y	Al_N	Number of used spectral lines for calculation of abundance
67	float	dex	Y	Si	Abundance of Si [Si/H]
68	int	-	Y	Si_N	Number of used spectral lines for calculation of abundance

TABLE 7
CATALOGUE DESCRIPTION (CONTINUED)

Col	Format	Units	NULL	Label	Explanations
69	float	dex	Y	Fe	Abundance of Fe [Fe/H]
70	int	-	Y	Fe_N	Number of used spectral lines for calculation of abundance
71	float	dex	Y	Ti	Abundance of Ti [Ti/H]
72	int	-	Y	Ti_N	Number of used spectral lines for calculation of abundance
73	float	dex	Y	Ni	Abundance of Ni [Ni/H]
74	int	-	Y	Ni_N	Number of used spectral lines for calculation of abundance
75	float	dex	Y	Mg	Abundance of Mg [Mg/H]
76	int	-	Y	Mg_N	Number of used spectral lines for calculation of abundance
77	float	-	Y	CHISQ_c	?2 of the Chemical Pipeline (Note 1)
78	float	K	Y	Teff_SPARV	Effective temperature (Note 1)
79	float	dex	Y	logg_SPARV	Log gravity (Note 1)
80	float	dex	Y	alpha_SPARV	Metallicity (Note 1)
81	char(16)	-	Y	ID_2MASS	2MASS Target designation
82	float	arcsec	Y	Dist_2MASS	Center distance to target catalog
83	char(2)	-	Y	XidQualityFLAG_2MASS	Crossmatch quality flag (Note 4)
84	double	mag	Y	Jmag_2MASS	J magnitude
85	double	mag	Y	eJmag_2MASS	Error J magnitude
86	double	mag	Y	Hmag_2MASS	H magnitude
87	double	mag	Y	eHmag_2MASS	Error H magnitude
88	double	mag	Y	Kmag_2MASS	K magnitude
89	double	mag	Y	eKmag_2MASS	Error K magnitude
90	char(16)	-	Y	ID_DENIS	DENIS Target designation
91	double	arcsec	Y	Dist_DENIS	Centre distance to target catalog
92	char(2)	-	Y	XidQualityFLAG_DENIS	Crossmatch quality flag (Note 4)
93	double	mag	Y	Imag_DENIS	I magnitude
94	double	mag	Y	eImag_DENIS	Error I magnitude
95	double	mag	Y	Jmag_DENIS	J magnitude
96	double	mag	Y	eJmag_DENIS	Error J magnitude
97	double	mag	Y	Kmag_DENIS	K magnitude
98	double	mag	Y	eKmag_DENIS	Error K magnitude
99	char(16)	-	Y	ID_USNOB1	USNOB1 Target designation
100	double	arcsec	Y	Dist_USNOB1	Centre distance to target catalog
101	char(2)	-	Y	XidQualityFLAG_USNOB1	Crossmatch quality flag (Note 4)
102	double	mag	Y	B1mag_USNOB1	B1 magnitude
103	double	mag	Y	R1mag_USNOB1	R1 magnitude
104	double	mag	Y	B2mag_USNOB1	B2 magnitude
105	double	mag	Y	R2mag_USNOB1	R2 magnitude
106	double	mag	Y	Imag_USNOB1	I magnitude
107	float	mas	Y	parallax	Parallax (Note 4)
108	float	mas	Y	e_parallax	Error Parallax (Note 4)
109	float	kpc	Y	dist	Distance (Note 4)
110	float	kpc	Y	e_dist	Error Distance (Note 4)
111	float	-	Y	DistanceModulus_Binney	Distance modulus (Note 4)
112	float	-	Y	eDistanceModulus_Binney	Distance modulus (Note 4)
113	float	-	Y	Av	Extinction (Note 4)
114	float	-	Y	e_Av	Error Extinction (Note 4)
115	float	-	Y	age	Age (Note 4)
116	float	-	Y	e_age	Error Age (Note 4)
117	float	MSun	Y	mass	Mass (Note 4)
118	float	MSun	Y	e_mass	Error Mass (Note 4)

TABLE 7
CATALOGUE DESCRIPTION (CONTINUED)

Col	Format	Units	NULL	Label	Explanations
119	char(2)	-	Y	c1	n.th minimum distance (Note 6)
120	char(2)	-	Y	c2	n.th minimum distance (Note 6)
121	char(2)	-	Y	c3	n.th minimum distance (Note 6)
122	char(2)	-	Y	c4	n.th minimum distance (Note 6)
123	char(2)	-	Y	c5	n.th minimum distance (Note 6)
124	char(2)	-	Y	c6	n.th minimum distance (Note 6)
125	char(2)	-	Y	c7	n.th minimum distance (Note 6)
126	char(2)	-	Y	c8	n.th minimum distance (Note 6)
127	char(2)	-	Y	c9	n.th minimum distance (Note 6)
128	char(2)	-	Y	c10	n.th minimum distance (Note 6)
129	char(2)	-	Y	c11	n.th minimum distance (Note 6)
130	char(2)	-	Y	c12	n.th minimum distance (Note 6)
131	char(2)	-	Y	c13	n.th minimum distance (Note 6)
132	char(2)	-	Y	c14	n.th minimum distance (Note 6)
133	char(2)	-	Y	c15	n.th minimum distance (Note 6)
134	char(2)	-	Y	c16	n.th minimum distance (Note 6)
135	char(2)	-	Y	c17	n.th minimum distance (Note 6)
136	char(2)	-	Y	c18	n.th minimum distance (Note 6)
137	char(2)	-	Y	c19	n.th minimum distance (Note 6)
138	char(2)	-	Y	c20	n.th minimum distance (Note 6)

^a**Notes.** (1): Originating from: `_K` indicates values from Stellar Parameter Pipeline, `_NK` indicates a calibrated value, `_c` indicates values from Chemical Pipeline, `_SPARV` indicates values of Radial Velocity Pipeline (used in DR3 also). (2): Cross-identification flag as follows: `A = 1` association within 2 arcsec. `B = 2` associations within 2 arcsec. `C = More than 2` associations within 2 arcsec. `D = Nearest` neighbour more than 2 arcsec. away. `X = No` association found (within 10 arcsec limit). (3): Flag value of the form FGSH, F being for the entire plate, G for the 50 fibres group to which the fibre belongs. S flags the zero-point correction used: C for cubic and S for a constant shift. If H is set to * the fibre is close to a 15 fibre gap. For F and G the values can be A, B, C, D, or E `A = dispersion` around correction lower than 1km/s `B = dispersion` between 1 and 2km/s `C = dispersion` between 2 and 3km/s `D = dispersion` larger than 3km/s `E = less` than 15 fibres available for the fit. (4): See Binney et al. (2013). (5): Flag of Stellar Parameter Pipeline 0 = Pipeline converged. 1 = no convergence. 2 = MATISSE oscillates between two values and the mean has been performed. 3 = results of MATISSE at the boundaries or outside the grid and the DEGAS value has been adopted 4 = the metal-poor giants with SNR<20 have been re-run by degas with a scale factor (ie, internal parameter of DEGAS) of 0.40 (6): Morphological Flag n.th minimum distance to base spectrum given by one of the types *a,b,c,d,e,g,h,n,o,p,t,u,w* (see Matijević et al. 2012).

Robin, A. C., Reylyé, C., Derrière, S., & Picaud, S. 2003, *A&A*, 409, 523
Roeser, S., Demleitner, M., & Schilbach, E. 2010, *AJ*, 139, 2440
Röser, S., Schilbach, E., Schwan, H., et al. 2008, *A&A*, 488, 401
Ruchti, G. R., Fulbright, J. P., Wyse, R. F. G., et al. 2011, *ApJ*, 737, 9
Salaris, M., Chieffi, A., & Straniero, O. 1993, *ApJ*, 414, 580
Sales, L. V., Helmi, A., Abadi, M. G., et al. 2009, *MNRAS*, 400, L61
Schönrich, R., Binney, J., & Asplund, M. 2012, *MNRAS*, 420, 1281
Seabroke, G. M., Gilmore, G., Siebert, A., et al. 2008, *MNRAS*, 384, 11
Sellwood, J. A., & Binney, J. J. 2002, *MNRAS*, 336, 785
Siebert, A., Bienaymé, O., Binney, J., et al. 2008, *MNRAS*, 391, 793
Siebert, A., Famaey, B., Minchev, I., et al. 2011a, *MNRAS*, 412, 2026
Siebert, A., Williams, M. E. K., Siviero, A., et al. 2011b, *AJ*, 141, 187
Siebert, A., Famaey, B., Binney, J., et al. 2012, *MNRAS*, 425, 2335
Smith, J. A., Tucker, D. L., Kent, S., et al. 2002, *AJ*, 123, 2121
Snedden, C. A. 1973, PhD thesis, THE UNIVERSITY OF TEXAS AT AUSTIN.
Soubiran, C., & Girard, P. 2005, *A&A*, 438, 139

Soubiran, C., Le Campion, J.-F., Cayrel de Strobel, G., & Caillo, A. 2010, *A&A*, 515, A111
Steinmetz, M., Zwitter, T., Siebert, A., et al. 2006, *AJ*, 132, 1645
The Denis Consortium. 2005, *VizieR Online Data Catalog*, 1, 2002
Valdes, F., Gupta, R., Rose, J. A., Singh, H. P., & Bell, D. J. 2004, *ApJS*, 152, 251
Valenti, J. A., & Fischer, D. A. 2005, *ApJS*, 159, 141
van der Kruit, P. C., & Freeman, K. C. 2011, *ARA&A*, 49, 301
Veltz, L., Bienaymé, O., Freeman, K. C., et al. 2008, *A&A*, 480, 753
Wainscoat, R. J., Cohen, M., Volk, K., Walker, H. J., & Schwartz, D. E. 1992, *ApJS*, 83, 111
Williams, M. E. K., Steinmetz, M., Sharma, S., et al. 2011, *ApJ*, 728, 102
Williams, M. E. K., Steinmetz, M., Binney, J., et al. 2013, *ArXiv e-prints*, 1302.2468
Wilson, M. L., Helmi, A., Morrison, H. L., et al. 2011, *MNRAS*, 413, 2235
Zacharias, N., Finch, C. T., Girard, T. M., et al. 2013, *AJ*, 145, 44
Zacharias, N., Urban, S. E., Zacharias, M. I., et al. 2004, *AJ*, 127, 3043
Zacharias, N., Finch, C., Girard, T., et al. 2010, *AJ*, 139, 2184
Zwitter, T., Siebert, A., Munari, U., et al. 2008, *AJ*, 136, 421
Zwitter, T., Matijević, G., Breddels, M. A., et al. 2010, *A&A*, 522, A54

We are most grateful to our referee, for his detailed and very relevant comments which improved the quality of the presentation of the paper. Funding for RAVE has been provided by: the Australian Astronomical Observatory; the Leibniz-Institut für Astrophysik Potsdam (AIP); the Australian National University; the Australian Research Council; the French National Research Agency; the German Research Foundation (SPP 1177 and SFB 881); the European Research Council (ERC-StG 240271 Galactica); the Instituto Nazionale di Astrofisica at Padova; The Johns Hopkins University; the National Science Foundation of the USA (AST-0908326); the W. M. Keck foundation; the Macquarie

University; the Netherlands Research School for Astronomy; the Natural Sciences and Engineering Research Council of Canada; the Slovenian Research Agency; the Swiss National Science Foundation; the Science & Technology Facilities Council of the UK; Opticon; Strasbourg Observatory; and the Universities of Groningen, Heidelberg and Sydney. This work was partly supported by the European Union FP7 programme through ERC grant number 320360. The RAVE web site is at <http://www.rave-survey.org>.